



LAWRENCE  
LIVERMORE  
NATIONAL  
LABORATORY

LLNL-JRNL-439291

# Capsule Implosion Optimization during the Indirect-Direct National Ignition Campaign

O. L. Landen, T. R. Boehly, D. K. Bradley, D. G. Braun, D. A. Callahan, P. M. Celliers, G. W. Collins, E. L. Dewald, L. Divol, S. H. Glenzer, A. Hamza, D. G. Hicks, N. Hoffman, O. S. Jones, R. K. Kirkwood, G. A. Kyrala, P. Michel, J. Milovich, D. H. Munro, R. E. Olson, A. Nikroo, H. F. Robey, B. K. Spears, C. A. Thomas, S. V. Weber, D. C. Wilson, M. M. Marinak, L. J. Suter, B. A. Hammel, D. D. Meyerhofer, J. Atherton, J. Edwards, S. W. Haan, J. D. Lindl, B. J. MacGowan, E. I. Moses

June 30, 2010

Physics of Plasmas

## **Disclaimer**

---

This document was prepared as an account of work sponsored by an agency of the United States government. Neither the United States government nor Lawrence Livermore National Security, LLC, nor any of their employees makes any warranty, expressed or implied, or assumes any legal liability or responsibility for the accuracy, completeness, or usefulness of any information, apparatus, product, or process disclosed, or represents that its use would not infringe privately owned rights. Reference herein to any specific commercial product, process, or service by trade name, trademark, manufacturer, or otherwise does not necessarily constitute or imply its endorsement, recommendation, or favoring by the United States government or Lawrence Livermore National Security, LLC. The views and opinions of authors expressed herein do not necessarily state or reflect those of the United States government or Lawrence Livermore National Security, LLC, and shall not be used for advertising or product endorsement purposes.

## **Capsule Implosion Optimization during the Indirect-Drive National Ignition**

### **Campaign\***

O. L. Landen<sup>1</sup>, T. R. Boehly<sup>2</sup>, D. K. Bradley<sup>1</sup>, D. G. Braun<sup>1</sup>, D. A. Callahan<sup>1</sup>, P. M. Celliers<sup>1</sup>, D.S. Clark<sup>1</sup>, G. W. Collins<sup>1</sup>, E. L. Dewald<sup>1</sup>, L. Divol<sup>1</sup>, S. H. Glenzer<sup>1</sup>, A. Hamza<sup>1</sup>, D. G. Hicks<sup>1</sup>, N. Hoffman<sup>3</sup>, N. Izumi<sup>1</sup>, O. S. Jones<sup>1</sup>, R. K. Kirkwood<sup>1</sup>, J. L. Kline<sup>3</sup>, G. A. Kyrala<sup>3</sup>, P. Michel<sup>1</sup>, J. Milovich<sup>1</sup>, D. H. Munro<sup>1</sup>, R. E. Olson<sup>4</sup>, A. Nikroo<sup>5</sup>, H. F. Robey<sup>1</sup>, B. K. Spears<sup>1</sup>, C. A. Thomas<sup>1</sup>, S. V. Weber<sup>1</sup>, D. C. Wilson<sup>3</sup>, M. M. Marinak<sup>1</sup>, L. J. Suter<sup>1</sup>, B. A. Hammel<sup>1</sup>, D. D. Meyerhofer<sup>2</sup>, J. Atherton<sup>1</sup>, J. Edwards<sup>1</sup>, S.W. Haan<sup>1</sup>, J. D. Kilkenny<sup>5</sup>, J. D. Lindl<sup>1</sup>, B. J. MacGowan<sup>1</sup>, and E. I. Moses<sup>1</sup>

<sup>1</sup>Lawrence Livermore National Laboratory, Livermore, CA, 94550, USA

<sup>2</sup>Laboratory for Laser Energetics, Rochester, NY, USA

<sup>3</sup>Los Alamos National Laboratory, Los Alamos, NM, USA

<sup>4</sup>Sandia National Laboratory, Albuquerque, NM, USA

<sup>5</sup>General Atomics, San Diego, CA, USA

### **Abstract**

Capsule performance optimization campaigns will be conducted at the National Ignition Facility [G.H. Miller, E.I. Moses and C.R. Wuest, Nucl. Fusion **44**, 228 (2004)] to substantially increase the probability of ignition. The campaigns will experimentally correct for residual uncertainties in the implosion and hohlraum physics used in our

radiation-hydrodynamic computational models using a variety of ignition capsule surrogates before proceeding to cryogenic-layered implosions and ignition experiments. The quantitative goals and technique options and downselections for the tuning campaigns are first explained. The computationally derived sensitivities to key laser and target parameters are compared to simple analytic models to gain further insight into the physics of the tuning techniques. The results of the validation of the tuning techniques at the OMEGA facility under scaled hohlraum and capsule conditions relevant to the ignition design are shown to meet the required sensitivity and accuracy. In addition, a roll-up of all expected random and systematic uncertainties in setting the key ignition laser and target parameters due to residual measurement, calibration, cross-coupling, surrogacy, and scale-up errors has been derived that meets the required budget. Finally, we show how the tuning precision will be improved after a number of shots and iterations to meet an acceptable level of residual uncertainty.

\*This work was performed under the auspices of the U.S. Department of Energy by Lawrence Livermore National Laboratory under Contract DE-AC52-07NA27344.

## I. INTRODUCTION

The National Ignition Facility (NIF)<sup>1</sup> is a 192 beam, 1.8 MJ 0.35  $\mu\text{m}$  laser designed to drive inertial confinement fusion (ICF) capsules to ignition<sup>2</sup>. In the indirect-drive approach<sup>3</sup>, the laser energy is converted to thermal x-rays inside a high Z cavity (hohlraum). The x rays then ablate the outer layers of a DT-filled capsule placed at the center of the hohlraum, causing the capsule to implode, compress and heat the DT and ignite.

The main attributes of a representative ignition design (cryogenic hohlraum target<sup>4</sup> and NIF laser<sup>5</sup>) are shown in Fig. 1. A cm-long high Z cylindrical hohlraum, currently designed with Au-lined U walls filled with 0.9 mg/cc of He tamping gas, is equipped with two Laser Entrance Holes (LEH) of  $\approx 50\text{--}55\%$  the hohlraum diameter. Details of the LEH and other features of the target will be finalized to optimize performance based on the results of ongoing hohlraum energetics experiments<sup>6</sup> that precede the capsule tuning experiments. To provide low mode symmetry, 24 sets of beams arranged in quads of 4 beams each enter from each side in sets of 4, 4, 8 and 8 at  $23.5^\circ$ ,  $30^\circ$ ,  $44.5^\circ$  and  $50^\circ$ . The hohlraum is driven by a 1.3 MJ, 20 ns-long shaped pulse with 5 distinct phases: a 2 ns front picket to burn through the fill gas and set the initial shock, a 9 ns long trough to maintain a constant first shock velocity in the fuel, two further spikes to launch the second and third shocks, and a 4<sup>th</sup> rise to peak power for final acceleration of the shell at a peak radiation temperature  $T_r$  of 300 eV.

The current design<sup>7</sup> for the cryogenic capsule at hohlraum center is a graded Ge-doped<sup>8,9</sup> CH ablator of 918  $\mu\text{m}$  inside radius and 190  $\mu\text{m}$  shell thickness enclosing a 68

$\mu\text{m}$ -thick layer of solid DT fuel initially held near the triple point<sup>10</sup>. However, a variety of hohlraum and capsule options<sup>11,12,13</sup> have been designed, spanning peak radiation temperatures between 270 and 310 eV, and using either Cu-doped Be<sup>14</sup>, Ge-doped CH<sup>15</sup> or undoped or Mo-doped High Density Carbon<sup>16</sup> (HDC) capsules. A subset of these designs have a detailed set of target and laser parameter tolerances based on 1D, 2D and 3D<sup>17</sup> sensitivity simulations<sup>18,19,20,21,22</sup>. Unless otherwise noted, the tuning techniques and their required accuracy described in later sections of this paper are based on the design and sensitivity simulations for a 285 eV, 1.2 MJ graded-doped Be capsule<sup>22</sup> shown in Figure 2 developed during an earlier simulated campaign before the decision was made to focus on CH. Detailed sensitivity analyses for the current CH design are part of the preparations for the upcoming late 2010 campaign. In general, while the starting point target and laser parameters can vary between designs by more than the tolerable variation within a design, the sensitivity of key implosion parameters such as entropy and asymmetry to target and laser parameters variations are calculated to be similar to within a factor of 30% across both designs, within the tuning budget and simulation sensitivity uncertainty. When differences in the capsule material or laser pulseshape choice significantly affect specifics of the tuning technique, this will be addressed on a case-by-case basis.

The first tuning campaign is preceded by hohlraum energetics campaigns to validate or change the go-forward peak  $T_r$ , hohlraum and LEH liner material, and laser spot smoothing choices. Although originally planned to start by using only the first 96 beams<sup>23</sup>, the energetics campaign started in 2009 is accomplishing these goals using both 83%-scale 700 kJ and full scale up to 1.3 MJ 192 beam gas-filled Au hohlraums<sup>6</sup>. The

campaign has so far demonstrated  $> 90\%$  laser-plasma absorption using backscatter<sup>24</sup> and near backscatter<sup>25</sup> optical diagnostics on a  $30^\circ$  and  $50^\circ$  beam quad, adequate ( $< 5\%$  peak) hot electron levels using a filter-fluorescer diagnostic<sup>26</sup>, peak hohlraum thermal x-ray production to at least  $90\%$  of expected using the multi-channel soft x-ray power diagnostic Dante<sup>27</sup>, and the ability to control imploded core symmetry diagnosed using a gated imager<sup>28</sup> to better than  $20\%$  out of round. These 2009 hohlraum energetics experiments also confirmed earlier 2004 20 kJ-class single-ended vacuum hohlraum x-ray drive results<sup>29</sup> using the first 4 beams of NIF (the NIF Early Light (NEL) campaign<sup>30</sup>). The NEL drive results in turn matched modeling validated by prior similar energy Nova<sup>31</sup> and OMEGA<sup>32</sup> facility hohlraum data<sup>33</sup> taken with the same type of Dante detector, itself shown to agree<sup>34</sup> with the analogous soft x-ray power diagnostic for the LMJ facility<sup>35</sup>, DMX<sup>36</sup>. This x-ray drive consistency across facilities<sup>37</sup> has lent further credence to an observed improvement<sup>38</sup> in x-ray C.E. at fixed laser intensity as vacuum hohlraum scale is increased on NIF, attributed to increased volume-to-surface area. Finally, gas-filled hohlraums<sup>39</sup> and tubes<sup>40</sup> demonstrated the efficacy of laser spot smoothing in improving beam propagation using continuous phase plates<sup>41</sup>, Polarization Smoothing<sup>42</sup> (PS) and Smoothing by Spectral Dispersion (SSD) for the case of a NIF quad geometry.

The overall goal of the following planned capsule performance optimization campaign<sup>43</sup> is to empirically correct for residual uncertainties in the implosion and hohlraum physics used in our radiation-hydrodynamic computational models<sup>44,45</sup>. We will interleave cryogenic-layered targets<sup>46</sup> with the non-layered targets described below as we work toward an optimal fuel assembly before proceeding to ignition attempts..

This will be accomplished using a variety of surrogate targets that will set key laser, hohlraum and capsule parameters to maximize ignition capsule implosion velocity, while minimizing fuel entropy (or adiabat), core shape asymmetry and ablator-fuel mix. Regardless of the final scale chosen for ignition attempts (1.2 - 1.7 MJ), the initial tuning is planned at 1.2 MJ to reduce total laser energy requirements, representing  $\approx (1.2/1.7)^{1/3} \approx 0.84$  linear scale if we pursue for example a 1.7 MJ ignition design. This is followed by intentionally-dudged tritium-rich but deuterium-poor cryogenically layered implosions<sup>47</sup> to check the efficacy of the tuning through shared observables such as core symmetry and bangtime, and from implosion performance. Finally, if the chosen ignition design called for larger scale, the tuning would be checked at this scale, before proceeding to tests of alpha-heating and ignition attempts.

Extensive computational multivariable sensitivity studies have shown that, the probability of ignition is well correlated<sup>7</sup> to the four key implosion parameters of 1D peak fuel implosion velocity  $v$ , 1D burn-averaged imploded fuel adiabat  $\alpha$ , rms asymmetry  $\Delta R_{\text{hotspot}}/R_{\text{hotspot}}$  at the hotspot-main fuel interface, and fraction  $\Delta R_{\text{mix}}/\Delta R_{\text{fuel}}$  of fuel mixed with ablator. The fuel adiabat is defined as the ratio of the ion + electron pressure to the electron Fermi pressure at zero temperature. As described by the companion paper by Haan *et. al.*<sup>7</sup>, the product of power laws of these four parameters, for small excursions, can be used to define an Ignition Threshold Factor (ITF) given by the following equation:

$$ITF = \frac{E_{\text{fuel}}}{3.2\text{kJ}} \left( \frac{v}{380\text{km/sec}} \right)^8 \left( \frac{\alpha}{1.46} \right)^{-4} \left( 1 - 1.2 \frac{\Delta R_{\text{hotspot}}}{R_{\text{hotspot}}} \right)^{4.5} \left( 1 - \frac{\Delta R_{\text{mix}}}{\Delta R_{\text{fuel}}} \right)^{0.5} \quad (1)$$



The constants 380 km/s and 1.46 in the denominators are specific to a particular design (the 285 eV 1.2 MJ Be design in this case). The values of the exponents can also vary by about 10% depending on the capsule design choice. The probability of ignition versus ITF is shown as the bold dashed line in Figure 2, where by definition, an ITF of 1 equates to 50% probability of ignition by normalizing to 3.2 kJ of stored capsule fuel energy. The slope on the rise of the ignition probability curve is set by uncertainties in conduction and charged particle stopping power physics as they affect ignition and residual deviations between the ITF power law fit and individual realizations. Also shown on Figure 3 are the expected ITF distributions before tuning, after tuning with capsules having no cryogenic fuel layers (the subject of this paper), and after further tuning using cryogenically layered implosions as described in the companion paper by Edwards et al.<sup>47</sup>. Figure 3 shows that tuning is expected to increase the mean ITF from 0.2 to 1.5. The width of the initial distribution is set by the target physics models uncertainties, and the width of the intermediate and final distributions set by the quadrature sum of expected residual shot-to-shot variability in laser and target parameters and residual errors in tuning.

The expected initial and final uncertainties in the four implosion parameters are given in the second and third columns in Table I. The initial uncertainties have been estimated based on a combination of level of confidence in extrapolating radiation hydrodynamics models fitting Nova, OMEGA and Z facility hohlraum energetics<sup>48</sup>, x-ray driven planar hydrodynamics<sup>49,50</sup> and gas-filled hohlraum implosions data<sup>51,52</sup> and residual differences between EOS<sup>53,54</sup>, opacity<sup>55,56</sup> and conductivity<sup>57,58</sup> models for the hohlraum, ablator and DT fuel plasmas. These uncertainties translate to uncertainties in capsule ablation rate<sup>59</sup>

affecting implosion velocities, to uncertainties in hohlraum x-ray conversion efficiency<sup>60</sup> albedo<sup>61,62</sup> and radiation hydrodynamics<sup>63</sup> affecting drive symmetry, and to uncertainties in hard x-ray preheat levels<sup>64</sup>, ablator compressibility and dopant opacity affecting fuel adiabats through shock transit times<sup>65,66</sup>, and affecting the level of ablator-fuel mix<sup>67</sup> through the ablator-fuel interface Atwood number<sup>68</sup>.

The tuning campaign is based on the principal that these physics uncertainties can be empirically corrected for by adjusting key laser and target parameters around their nominal values, thereby increasing the ITF by increasing implosion velocity, and lowering fuel adiabat, asymmetry and mix. Fourteen principal adjustable parameters have been identified, schematically shown in Figure 4 and listed in the fourth column in Table I alongside the implosion parameter they affect. For the laser, they are the power levels for the 5 phases in the laser pulse, the launch time for the second, third and fourth steps, the end-point in the 4<sup>th</sup> rise of laser power (when the pulse first reaches peak power), and the power balance between inner and outer cones during the first and last phase. For the target, there are three parameters; the hohlraum length, capsule ablator thickness for fixed inside diameter, and capsule ablator mid-Z dopant fraction. The fifth and sixth columns show the expected initial and final  $1\sigma$  uncertainties in setting these parameters that are consistent with the uncertainties quoted for the four implosion parameters. From Figure 4, it is clear that we choose not to vary some apparently equally fundamental laser and target parameters, such as the inner cone fraction during the trough, second and third pulse, and the radii of the hohlraum and capsule. The reasons are as follows. First, simulations show that we expect the contribution to the core asymmetry to remain below 5% rms (well below the  $< 10\%$  rms requirement) for a

maximum plausible uncertainty of  $\pm 25\%$  in setting the optimum inner cone fraction during the second and third shock phase. Second, the symmetry of the trough is expected to mimic the tuned symmetry of the first 2 ns by virtue of the quiescent conditions in the trough consisting of nearly constant laser power and high albedo. Third, the ratio of the hohlraum to capsule radius is set to minimize the geometric transfer of any hohlraum drive  $P_4$  asymmetry component onto the capsule<sup>3</sup>, so varying the hohlraum radius to change the illumination pattern at the hohlraum wall would require also varying the capsule radius. The  $P_4$  asymmetry at the wall can be minimized more independently by optimum choice of the laser pointing and the hohlraum length.

To adjust these key laser and target parameters by experimentation so as to optimize the implosion performance, we have chosen a set of non-igniting tuning shots equipped with a set of clear observables. Section II will discuss the goals, observables, expected accuracy and experimental demonstrations of the tuning techniques. Section III will present the goals and sequencing of the tuning shots and briefly discuss further experimental techniques for isolating capsule physics issues if required based on early implosion results. Section IV will summarize the tuning accuracy, and a more detailed appendix on the tuning accuracy breakdown is also included.

## II. TUNING TECHNIQUES

Extensive sets of shots were completed at the Nova and OMEGA facility to demonstrate and downselect between proposed tuning techniques. The mainline tuning targets chosen are the high Z re-emission spheres<sup>69</sup> setting the foot cone power balance

from the observed foot drive symmetry, liquid D<sub>2</sub>-filled “keyhole” targets setting the laser power profile up to peak power from the observed shock speeds and overtake distances and times<sup>70</sup>, x-ray imaged imploded capsules setting the peak cone power balance and hohlraum length from observed core symmetry<sup>71</sup>, and streaked or gated x-ray backlit imploding capsules<sup>72</sup> setting the initial ablator thickness and peak laser power from the radiographically-inferred ablator mass remaining<sup>73</sup> and implosion velocity. In addition, the Dante diagnostic will be used to set the 4<sup>th</sup> rise launch time from the 4<sup>th</sup> rise slope and to set the ablator dopant fraction from the measured hard ( $> 1.8$  keV) x-ray preheat levels. For the rest of this section, we will be discussing pulse-shapes and tuning targets appropriate for the full 1.2 MJ, 285 eV Be design scale. Unless otherwise stated, all uncertainties and errors are  $1\sigma$  values assuming Gaussian distributions. The tuning accuracy requirements have been balanced in terms of uncertainty to mean ITF (typically set at  $\pm 10\%$  for each term) which is referred back to in each section.

### **A. Drive Symmetry of First 2 ns**

The NIF cylindrical hohlraum ignition design has chosen inner (23.5 and 30°) and outer cone angles (44.5° and 50°) with respect to the hohlraum axis such that the centroids of these beams pass near the center of the LEH at optimum hohlraum length and initially point at hohlraum wall positions  $\approx$  subtending  $\theta = 90^\circ$  and  $40^\circ$  to the capsule pulse, representing the nodes of  $P_3$ . Hence, for an appropriate choice of inner to outer power ratio, one can simultaneously zero  $P_2$  and  $P_4$  (and all odd moments) at a particular value of wall albedo. Ensuring spherical symmetry of the first shock launch is important

for two reasons. First, simulations show that for an initial plausible 12%  $P_2$  incident flux asymmetry averaged over the first 2 ns, the final ignition core asymmetry could be outside the requirement of  $<10\%$  rms. We can relate this level of flux asymmetry to an uncertainty in setting the first 2 ns inner versus outer cone energy ratio. Defining the fraction of energy in the inner cone as CF, the change in  $P_2$  around zero at the capsule due to change in cone fraction is given by  $0.5[P_2(90^\circ) - P_2(40^\circ)](\Delta CF/CF)/(F+1) \approx 0.5 \times 2P_2(90^\circ)(\Delta CF/CF)/(F+1)$ , where 0.5 accounts for the geometric radiation transfer factor, diluted by the ratio of recirculating to spot flux<sup>3</sup>  $F = \alpha / [(1-\alpha) + (\Omega_{LEH} + \Omega_{Caps})/\Omega_W]$ . So a 12% incident  $P_2/P_0$  for  $F = 1$  given an average albedo  $\alpha = 0.6$  over the first 2 ns corresponds to an initial cone fraction uncertainty  $\Delta CF/CF = 50\%$ , as listed In Table I. Second, since shock timing is performed as a single point measurement (at the capsule equator,  $\theta = 90^\circ$ , see Section B), one must ensure that the measured first shock strength which sets 90% of the final compressed fuel entropy is representative of the solid angle averaged first shock strength. In the presence of an  $x\%$   $P_n$  flux asymmetry, the offset from optimum in the solid-angle averaged first shock pressure after setting the optimum shock pressure over a narrow range of angles  $90 \pm \Delta\theta$  is given by:

$$\Delta P = (7/8) \int x [P_n(\theta) - P_n(90 \pm \Delta\theta)] \sin \theta d\theta / \int \sin \theta d\theta \quad (2)$$

where the 7/8 factor accounts for the relationship between shock pressure and drive flux<sup>3</sup> and  $P_n(90 \pm \Delta\theta)$  is the average value of the  $P_n$  Legendre mode over polar angles  $90 \pm \Delta\theta$ . So, for  $\Delta\theta = \pm 4^\circ$  characteristic of the “keyhole” shock timing geometry described in Section B,  $\Delta P = 0.44x$  and  $-0.33x$  for a pure  $x\%$   $P_2$  and  $P_4$  asymmetry, respectively.

Hence, for a plausible  $x = 12\%$  initial  $P_2$  drive asymmetry, the average first shock pressure offset would be  $5.3\%$  corresponding to an  $\approx 1\%$  change in fuel entropy. Since entropy  $S$  can be substituted for adiabat  $\alpha$  in Eq. (1) through  $S \sim \alpha^{0.4}$ , ITF scales as  $S^{10}$ , and hence a  $1\%$  change in entropy equates to a significant  $10\%$  change in ITF. The preceding discussion ignored intrinsic azimuthal asymmetries; the plausible maximum first shock pressure offset at the capsule in the presence of an  $m = 4$  drive asymmetry at the equator due to differences in x-ray conversion efficiency between the  $23.5^\circ$  and  $30^\circ$  subcones is a negligible  $2\%$ . Finally, while the trough drive from 2- 6 ns will be shown in Section B to play an even more important role in setting the first shock velocity transiting the fuel at 8 – 12 ns, as mentioned earlier, the expected symmetry in the trough should change little from its measured initial state at 2 ns.

Based on these two considerations, the goal is to set the first 2 ns  $P_2$  and  $P_4$  drive asymmetry to  $0 \pm 5$  and  $7\%$ , respectively. Since a  $5\%$   $P_2$  flux asymmetry over the first 2 ns would only lead to a few % ignition core asymmetry that could be masked or mistaken for other asymmetries later in the pulse, we needed a different technique to isolate the first shock asymmetry. Two of the candidates, thin capsules that implode early<sup>74</sup> and backlit thinshells<sup>75</sup> that integrate the drive over shorter periods of time, were successfully tested and evaluated at OMEGA at 70% NIC-scale. Both have calculated undesirable heightened hydroinstability and shape distortion sensitivity to thickness non-uniformities since ensuring a relevant few ns bangtime requires starting with a much thinner  $10\text{-}\mu\text{m}$ -shell. The backlit thinshell symmetry is recorded earlier in its trajectory (typically having imploded  $1/3$  to  $1/2$  of its initial radius) that still allows for a sufficiently accurate measure of asymmetry simply due to having more spatial resolution elements around its larger

circumference. However, both techniques only sense an average asymmetry over a time period when the  $P_2$  asymmetry is varying strongly due to increasing hohlraum albedo and when it is most sensitive to uncertainties in differential hohlraum gas burnthrough rates of inner versus outer beam cones. Moreover both have a strong time-dependent symmetry sensitivity, being most sensitive at the onset of acceleration<sup>75</sup> (at typical 0.5 ns break-out times for 20  $\mu\text{m}/\text{ns}$  shock speeds), and their trajectories and hence geometric smoothing factors deviate after that compared to the much thicker, higher inertia ignition capsule. Both techniques remain back-up options for studying the symmetry during the first 2 ns and primary options if we need to isolate the asymmetry between the first 2 ns and the peak of the drive.

To record the instantaneous asymmetry during the first shock launch time (the first 2 ns), we have chosen instead to take multiple images in time of the soft x-ray reemission from a non-imploding Bi ball replacing the ignition capsule. Since the ignition capsule radius only shrinks from shock compression by  $\approx 2/(\gamma+1) \times 20 \mu\text{m}/\text{ns} \times 2 \text{ ns} \approx 30 \mu\text{m}$  out of 1 mm during the first 2 ns, the geometric drive symmetry smoothing factor between hohlraum and sphere vs ignition capsule remain similar to a few %. Simulations have shown that the hohlraum gas-fill environment through which the beams are traversing is not affected for at least the required 2 ns by having Bi rather than ignition capsule ablation. Each point on the Bi sphere is radiatively heated locally, and the local re-emission flux is a measure of the local incident flux. Bi is chosen as it is a higher  $Z$  material than the Au hohlraum wall that the beams interact with during the foot, mitigating fluorescence concerns. In practice, the re-emission from the ball limb is imaged through a diagnostic hole or LEH, providing an instantaneous measure of the flux

incident on the ball vs. polar or azimuthal angle, respectively. After 2 ns, the Bi ablation smears out the limb and reduces accuracy. The accuracy on the measurement of the flux asymmetry is enhanced by choosing a re-emission photon energy  $h\nu$  that is many times the thermal reemission temperature  $kT_{\text{re}}$  of the hohlraum drive. Specifically, in the limit of Planckian sources, an  $n$  % incident flux asymmetry should result in an  $n \times (h\nu/4kT_{\text{re}})$  % re-emission flux asymmetry. Figure 5 shows that the calculated asymmetry amplification factor at various reemission photon energies using a more realistic incident drive spectrum (corresponding to  $T_r = 97$  eV at  $t = 3$  ns, hence  $T_{\text{re}} = 97\alpha^{1/4} = 90$  eV for calculated albedo  $\alpha = 0.75$ ) also matches closely the analytic Planckian  $h\nu/4kT_{\text{re}}$  formula. There is a practical limit however to the maximum usable  $h\nu$  as the re-emission flux falls off exponentially with photon energy.

The first reemission experiments at Nova diagnosed early time symmetry at higher temperature drives ( $T_r = 100$ -200 eV) using 2 keV reemitted x-rays<sup>69</sup>, corresponding to values of  $h\nu/4kT_{\text{re}} = 4$ -8. Subsequently, viable reemission designs for measuring the foot symmetry of various 1 MJ ignition designs were documented<sup>76</sup>. Figure 6 shows the planned experimental set-up for the NIC tuning and the starting point truncated pulse powers for the first 2 ns. A 2x magnification, 50  $\mu\text{m}$ -resolution, 200 ps gated pinhole imager with thin high-pass filtering (e.g. 6  $\mu\text{m}$  of Al) appropriate for  $> 900$  eV x-rays is used. The spatial resolution is set as a balance of providing sufficient signal throughput while avoiding too much radial smearing of the limb profile. No grazing incidence x-ray mirrors for better spectral definition<sup>77</sup> are planned since they would cut down signal significantly, and we expect the natural drop in the Planckian flux from the Bi sphere to provide the cut-off on the high energy side. The combination of filter and Planckian



spectrum lead to a 300-400 eV bandpass. Up to 16 images are recorded, in 4 adjustable time periods, with the possibility of recording at 2 different values of  $h\nu$  on the same shot for crosschecks of reemission sensitivity.

Of note are the large 2.7 mm diameter low  $Z$  patches required to view soft x-rays from the Bi sphere along the hohlraum equator and to avoid high  $Z$  background wall emission blending with the Bi limb emission. The patch sizes are chosen as 0.7 mm larger than the 2 mm reemission sphere to allow for 200  $\mu\text{m}$  of view on all sides of the reemission sphere from all pinhole views subtending up to  $\pm 50$  mrad of parallax. In addition, to avoid adding further hohlraum background emission, the 4 inner  $30^\circ$  quads that would fully hit the patches are turned off (see Figure 6b) after they burn through the gas-fill (to maintain fidelity as long as possible for the laser heating at the gas-fill near the LEH where all beams cross) but before or soon after they reach the patches. The combination of having 25% of the inner beams turned off and the low  $Z$  patches leads to a deficit of drive at the equator and hence a positive  $P_2$  offset at the reemission sphere compared to the ignition capsule. This is partially cancelled by the higher albedo of the reemission sphere that preferentially heats the more proximate equatorial wall regions.

Figure 7 compares 3D Hydra<sup>45</sup> calculations including all the above-mentioned differences between the incident  $P_2/P_0$  flux inferred from a reemission sphere and the incident  $P_2/P_0$  flux on an ignition capsule averaged over the first 2 ns as a function of inner cone fraction. We note that the surrogacy offset in  $P_2$  is relatively small, +8%, because the viewfactor<sup>78</sup> between the patch areas and the Bi sphere limb from which the equatorial view data is extracted is small. The error in this offset is estimated based on 10% uncertainties in 100 eV low<sup>56</sup>  $Z$  and high<sup>62</sup>  $Z$  albedoes at  $\pm 2\%$ , well within the

requirement to tune to  $\pm 5\%$  in  $P_2$ . Moreover, a second identical imager viewing down the pole will check the azimuthal asymmetry expected from missing inner beams and patches. The starting point optimum reemission  $P_2/P_0$  is hence  $= +24 \pm 15\%$  based on multiplying the  $+8\%$  incident  $P_2/P_0$  offset shown in Figure 7 and the required accuracy of  $\pm 5\%$  by the design asymmetry amplification value of  $h\nu/4kT_{re} = 3$ . This  $\pm 15\%$  required accuracy in the observable, accounting for all target, laser and tuning systematic and random imperfections and errors, is also listed in the last column in Table I. If the measured reemission  $P_2/P_0$  on the first shot were outside these limits, we would vary the inner versus outer laser cone fraction while keeping the total power fixed by an amount set by the slope of Figure 7 to reach the offset goal of  $+24\%$  reemission  $P_2/P_0$ . Further shots would be required if the Figure 7 slope were found to be sufficiently different than expected or if we found more scatter than expected. The expected data scatter from existing 10% random shot-to-shot laser power imbalances between quads during the first 2 ns of the drive on the foot symmetry has been quantified using 3D Hydra simulations. The rms variation in inferred incident  $P_2/P_0$  along the reemission line-of-sight extracted from several 3D simulations with different realizations of this level of power imbalance is  $\pm 2.4\%$ , well below the  $\pm 5\%$  tuning requirement.

While the gated reemission sphere technique records  $P_n/P_0$  averaged over 200 ps at 4 separate times on any given shot, we ultimately require control of  $P_2/P_0$  averaged over 2 ns. Figure 2c shows that the  $P_0$  drive varies strongly over the first 2 ns. Calculations show that the drive below 10% of the local maximum at 1.5 ns would not be visible for any practical measurement at  $h\nu > 600$  eV. Fortunately, time-dependent simulations assuming a variety of cone fractions show that the  $P_2$  asymmetry component seeded by

the  $<10\%$   $P_0$  drive phase is only 1%, well below the required tuning accuracy. At later times, we can use either or both the relative brightness of the reemission images to weight each image  $P_2/P_0$  properly, or the soft x-ray foot drive measured through the LEH using the calibrated<sup>79</sup> Dante and correcting for unconverted light plasma emission<sup>80</sup>. For realistic 10% errors in relative  $P_0$  between frames (due to residual uncertainties in relative gains between the gated camera MCP microstrips, reemission albedo and pinhole sizes), and including the effect of a finite number of sampling times, we calculate that these sampling errors in inferring the incident time-integrated  $P_2$  are no more than  $\pm 2\%$  for a realistic range of  $P_2$  swings in time. Should target shrapnel and debris<sup>81</sup> prove to be too much of a threat to the fragile microchannel-plates in gated imagers, then the fallback option is to switch to time-integrating Image Plate<sup>82</sup> detection using Fuji BAS TR plates sensitive to soft x-rays.

The uncertainty in the Planckian approximation for the asymmetry amplification factor  $h\nu/4kT_{re}$  must also be taken into account since we are tuning the drive on the reemission sphere to an offset  $P_2$  to ensure symmetry at the ignition capsule. To estimate this error, we use the 40% difference between calculated versus measured relative sensitivities of the reemission asymmetry (see later Figure 9a) at two different reemission photon energies, 900 and 1200 eV. Hence a 5%  $P_2$  offset with such a  $\pm 20\%$  amplification uncertainty leads to a 1%  $P_2$  uncertainty. Finally, we have considered the reemission technique as applied to the CH capsule ignition designs that use a lower temperature foot drive (per Fig 1c, 75 instead of 95 eV) since they do not need to ensure melting of a polycrystalline ablator<sup>50</sup> during the foot. The plan is to use a softer channel

with its centroid at about 700 eV requiring thinner filtering (2.5  $\mu\text{m}$  Al) to maintain the same signal levels and amplification factors  $h\nu/4kT_{\text{re}}$ .

Figure 8a shows a schematic of the experimental set-up at OMEGA used to validate the technique at NIC-relevant scale and  $T_{\text{r}}$ . Nearly identical diagnostic distances and parameters were used as for the planned NIC set-up. Also shown is an example of a 2x magnification, 100  $\mu\text{m}$  by 70 ps resolution re-emission image at  $t = 0.7$  ns,  $h\nu = 900$  eV from a 1.4-mm diameter Bi sphere sampling a 100 eV, 1 ns drive in a 6.4-mm-long by 3.6-mm-diameter vacuum hohlraum irradiated by 21.4° and 59° OMEGA beams<sup>83</sup>. Figure 8b shows an example of the measured reemitted  $P_2$  asymmetry versus time at  $h\nu = 900$  eV for an inner cone fraction = 0.12.  $P_2$  decreases in time as the hohlraum heats up because the negative  $P_2$  from the cold LEH becomes relatively more prominent as the Au wall albedo increases in time. Also shown are two 3D Hydra post-shot simulations that match the trend, the upper curve showing the effect of an assumed 10% reduction in the inner cone coupling. Figure 9a plots the extracted  $P_2$  reemission asymmetry at  $t = 0.7$  ns as a function of imposed inner cone fraction for both 900 and 1200 eV channels. It shows that both data and the four postshot 3D Hydra simulations connected by lines agree on the expected decrease in  $P_2$  with increased inner beam fraction, higher sensitivity at the higher photon energy, and consistency between channels for the cone fraction of best symmetry. Since  $h\nu/4kT_{\text{re}} \approx 3$  at 1200 eV, the typical  $\pm 6\%$   $P_2$  reemission asymmetry error bar shown in Fig. 9 translates to  $\pm 2\%$  accuracy in inferred instantaneous incident  $P_2$  asymmetry. This accuracy is consistent with estimates based on shot noise and frame-to-frame variability and is well under the  $\pm 5\%$  requirement. Figure 9b compares a reemit image at later times ( $t = 1$  ns) vs simulations, in this case for the 1200

eV channel at an inner cone fraction = 0.12. We note the localized emission spike at the equator ( $\theta = 90^\circ$ ) not predicted by simulations where the thin ( $\approx 0.5 \mu\text{m}$ ) polyimide sheets stretched between hohlraum halves that hold the reemission sphere in place leave a gap. Recent experiments successfully eliminated this equatorial non-uniformity by mounting the reemission sphere using a thin stalk rather than polyimide sheets. They also extended the technique to near full-scale (2.1 mm Bi ball in a 9 mm by 5 mm hohlraum)<sup>84</sup> and demonstrated the required accuracy for also inferring  $P_4/P_0$ .

### **B. Timing and Strength of First 3 Shocks**

Ignition requires a pulse shape with a low power foot designed to send a carefully timed series of shocks through the frozen DT shell such that they overtake each other soon after they travel into the enclosed DT gas. If the shocks are too closely spaced, they will coalesce within the DT ice leading to an increase in the entropy at the inside surface of the DT ice, reducing compressibility. If they are too widely spaced, the DT ice decompresses between shocks. Unless the first 3 shocks are spaced correctly (at the level of  $\pm 50$  ps when including all other sources of error and imperfections), the DT will fail to reach the required high fuel  $\rho r$  at the end of the implosion. Since typical uncertainties in ablator and DT compressibility are at least 5%, even for those with measured first shock Hugoniot, the uncertainties in transit times of successive shocks scaling as  $1/\sqrt{\rho}$  can be expected to be at least  $\pm 2.5\%$  out of typical 4 ns transit times, hence  $> \pm 100$  ps, with  $\pm 200$  ps quoted in Table I.

As discussed in Section A, controlling the time-dependent strength of the first shock

in the fuel (to 10% in pressure, 5% in shock velocity as the first shock traverses the fuel) is also important in setting 90% of the final fuel entropy. This is achieved by using an independently adjustable first picket followed by a trough as shown in Fig 1c or 2c. In addition, the first shock pressure in the ablator must be kept high enough ( $> 2.6 \pm 0.1$  Mbar to promote complete melting)<sup>85</sup> in the case of polycrystalline Be. For the case of the lower melt point CH ablator, the first shock pressure is designed to be  $\approx 2\times$  lower ( $\approx 1.5$  Mbar), leading to a 15% lower first shock velocity and hence longer foot phase. We note that the 5% uncertainty in the melt pressure and uncertainty in the shock steadiness across the ablator are consistent with setting a minimum first shock velocity to 5% accuracy from fuel entropy considerations.

For the second and third shocks, a range<sup>3</sup> of launch times and compensating shock strengths can provide the optimum overtake distance<sup>86</sup> (a few  $\mu\text{m}$ s inside of the DT solid–gas interface) with a small effect on the final adiabat. The ratios of shock pressures and hence velocities are constrained to avoid large entropy jumps between successive shocks without resorting to adding more intermediate shocks<sup>3</sup>. The initial uncertainties of 20 and 10% in relating laser power to imposed shock pressure for the first shock and trough, and for the second and third shock in Table I are based on existing 10-15% Dante flux<sup>79</sup> and albedo accuracies<sup>61</sup> at these low drive temperatures.

Based on these considerations, the goals listed in the final column of Table I are to set the first shock velocity and steadiness to  $\pm 5\%$  of its design value near  $20 \mu\text{m}/\text{ns}$ , and to set the overtake point for the second and third shocks to within  $\pm 6 \mu\text{m}$  of its design distance of about  $10 \mu\text{m}$  past the DT fuel-gas interface. The latter goal will be accomplished by a combination of setting the second and third shock launch times to  $\pm 50$

ps and setting their velocities after overtaking the prior shocks to  $\pm 2\%$  of their design values near 37 and 60  $\mu\text{m}/\text{ns}$ , respectively. Since radiographic methods of assessing shock front velocities to these accuracies would require unrealistic sub- $\mu\text{m}$  accuracy after accounting for the fuel compression that occurs after each shock passage, we opted for a direct continuous measurement of the shock velocity. We achieve this by reflecting off the shock front<sup>87</sup> using a streaked 1D imaging laser-based interferometry system<sup>88</sup>, commonly known as VISAR, from which shock front velocities are extracted from fringe shifts and overtake distances extracted by integrating the velocity between the time of first shock break-out from the ablator-fuel interface and time of next shock overtake seen as a sudden jump in fringe shift. The initial design<sup>86</sup> proposed a planar liquid  $\text{D}_2$  cell sandwiched between the ablator and a transparent quartz window and placed on the side of the hohlraum to approximately mimic the DT ice drive conditions inside a capsule at the center of the hohlraum. Since then, with the realization that a 1 mm radius capsule provides an adequately large ( $>100 \mu\text{m}$  diameter) reflecting surface collected by the  $f/3$  optics of the VISAR, the experimental design has evolved to using a liquid  $\text{D}_2$ -filled Au cone reentrant inside the capsule, greatly increasing the fidelity<sup>89</sup> of the drive conditions.

A schematic of the experimental geometry is shown in Figure 10a with a simulated 659 nm VISAR streak showing the abrupt fringe shifts expected upon first shock breakout into the liquid  $\text{D}_2$  and from the second shock overtake a few ns later. The re-entrant cone is made of Au to reduce its wall losses and kept sufficiently thick (100  $\mu\text{m}$ ) to avoid side shock breakout into the  $\text{D}_2$  adding background self-emission. The tip of the cone is slightly oversized to allow for a reflecting endcap that will provide a spatial and intensity fiducial. The total return field-of-view will be 200  $\mu\text{m}$ , magnified by 15x onto

two optical streak cameras<sup>90</sup>. The two cameras allow the VISAR to be run with simultaneous high and low sensitivity channels with non-multiple values of  $\approx 3.1$  and  $1.2$  fringe shift/ $20 \mu\text{m}/\text{ns}$  to extract unique solutions to the velocities with high accuracy.

The tuning strategy is to first set the velocity of the first shock by adjusting the total power in the first pulse and in the trough, and then the overtake distance and coalesced second shock velocity by adjusting the second launch time and second pulse total power. Figure 10b shows the starting point laser powers for inner and outer cones, truncated to reduce laser fluence, debris energy and to avoid blanking of optics and windows by the much higher x-ray fluences from the peak of the pulse. The truncation strategy is based on simulations that show that any prompt preheat from the 4<sup>th</sup> pulse that would normally be present will have minimal effect on the transit times of earlier shocks at the accuracy required. Of note, the third pulse has been intentionally delayed by 1 ns to ensure the second shock velocity can be measured after it overtakes the first shock but before it itself is overtaken by the third shock. Figure 10c represents a simulated analyzed VISAR trace showing the three jumps in the leading shock velocity that might be expected in such a case. We also have the option of truncating after the second pulse to reduce total fluence and debris. The final step is to bring the third shock forward at the correct strength by adjusting third pulse total power and launch time so all shocks coalesce at same time and place.

Figure 11 plots the radial derivative in the pressure in initial Lagrangian coordinates versus time to highlight the shock front trajectories. Figure 11 shows that the calculated tuned shock trajectories in liquid D<sub>2</sub> vs solid DT (scaled to the same size design) are well matched, with no more than a known 100 ps timing offset for the first shock. In



particular, because the shocks are designed to coalesce within a few  $\mu\text{ms}$  of entering the DT gas, the rarefaction occurring at the solid–gas DT interface but of course absent in the liquid  $\text{D}_2$  surrogate has insufficient leverage time ( $< 200$  ps) to necessitate a correction offset in the desired coalescence point. The points in Figure 12 show three examples of the calculated sensitivity between key observables (the first and second shock velocity in the fuel and second shock overtake distance) and adjustable laser parameters (the trough power, and second pulse laser power  $P_L$  and launch time). By contrast, the laser power in the first pulse primarily sets the first shock velocity in the ablator, for which the observable is the shock breakout time into the  $\text{D}_2$ .

The calculated points of Figure 12 are fairly well matched by simple analytic scalings shown as the lines and described below. To a good approximation, the shock velocities in Figure 12a scale as  $\sqrt{P_L}$ , hence laser powers have to be set to  $\pm 10\%$ ,  $10\%$ ,  $4\%$  and  $4\%$  accuracy in the first, trough, second and third pulse to meet the  $\pm 5\%$ ,  $5\%$ ,  $2\%$  and  $2\%$  shock velocity requirements as listed in Table I, well within the demonstrated capabilities of the NIF laser<sup>5</sup>. The overtake distances depend on both relative and absolute shock velocities. Since the trough and second pulse ablation rates (per  $T_r^3$  scaling<sup>3</sup> and Figure 2c, calculable as the 4<sup>th</sup> pulse ablation rate of  $\approx 150 \mu\text{m} / 3 \text{ ns}$  multiplied by  $(100 \text{ eV} / 285 \text{ eV})^3$ , hence  $< 4 \mu\text{m/ns}$  in the initial uncompressed Lagrangian reference frame) can be neglected compared to the second and third shock velocities in the ablator ( $33$  and  $45 \mu\text{m/ns}$  in the same reference frame per Figure 11a), the change in either overtake time  $\Delta\tau$  or overtake distance  $\Delta x$  as a function of change in second or third shock launch time  $\Delta t_n$  is given by simple kinematics as:

$$\Delta\tau_n = [c_n/(c_n - 1)]\Delta t_n \text{ and } \Delta x_n = u_{n-1}\Delta\tau_n \quad (3)$$

where  $c_n$  is the ratio of the overtaking to overtaken shock velocity  $u_{n-1}$  in the  $D_2$ . Extracting these velocity ratios from Figure 11a and other such detuned plots in the initial Lagrangian reference frame,  $c_2 = 100/20 = 5$ , and  $c_3 = 240/100 = 2.4$  or  $150/37 \approx 4$  depending on whether the 3<sup>rd</sup> shock overtakes the second shock (early) or coalesced second shock (late). By Eq. (3), the budgeted  $\Delta t = \pm 50$  ps uncertainty in second or third shock launch time leads to  $\Delta\tau_2 \approx \pm 65$  ps and  $\Delta\tau_3 = -85, +70$  ps, and  $\Delta x_2 = \pm 1.5$   $\mu\text{m}$  and  $\Delta x_3 = -3, +2.5$   $\mu\text{m}$ . Applying a similar analysis for the sensitivity of coalescence times and distances to variability in second and third shock velocities  $\Delta u_n$ :

$$\Delta\tau_n/(\tau - t_n) = \Delta x_n/x = -[c_n/(c_n - 1)]\Delta u_n/u_n \quad (4)$$

where the coalescence time  $\tau$  is  $\approx 12.5$  ns per Figure 11 and the shock launch times  $t_2$  and  $t_3$  are  $\approx 7$  and 9 ns per Figure 2c. Hence, the budgeted 2% variability in second and third shock velocities will translate to 2.2 and 2.9% variability in  $\Delta\tau_n/(\tau - t_n)$ , leading to  $\Delta\tau_2 \approx \pm 120$  ps and  $\Delta\tau_3 = \pm 100$  ps. Moreover, for the design value of  $x = \text{ablator} + \text{fuel thickness} + 5$   $\mu\text{m} \approx 240$   $\mu\text{m}$  per Figure 2b,  $\Delta x_2 = \pm 6$   $\mu\text{m}$  and  $\Delta x_3 = \pm 7$   $\mu\text{m}$ . We note that the contributions to variations in  $\tau$  and  $x$  are comparable between the budgeted variability in launch times and shock strengths as expected for balancing risk. We also note that since the first shock breakout time and velocity will be observable on every shot, we can apply a postshot correction for its variability to the measured shock coalescence distance.

The drive fidelity of the “keyhole” target relative to the ignition target has been evaluated using 3D Hydra simulations. The simulations show between 4% less (during the trough) and 0.5% more (during the third pulse) hohlraum x-ray flux at the ablator opposite the VISAR line-of-sight. This can be attributed to the extra 3% by area high albedo Au cone being unable to match at all relevant  $T_r$  the losses from the  $\approx 1$  sr section of low albedo ablator it replaced. Nevertheless, given the previously quoted high Z wall and low Z ablator albedo uncertainties of  $\pm 10\%$ , we would thus expect  $< \pm 1\%$  errors after correcting for relative fluxes between the keyhole and ignition hohlraum, and hence negligible  $\pm 0.5\%$  fidelity errors in shock velocities. In addition, the 10, 6 and 5% random shot-to-shot laser power imbalances between quads during the first, second and third pulse drives is expected to yield  $< 2$ , 1 and 1% flux variability at the capsule surface on the VISAR line-of-sight, small compared to the  $\pm 10$ , 4 and 4% required accuracies in setting the drive, respectively. The combined effect of residual uncertainties in as-built 1D capsule parameters such as ablator dopant concentration (e.g.  $\pm 0.1\%$ ) and ablator thickness (e.g.  $\pm 1 \mu\text{m}$ ) are expected to provide  $< 1\%$  and  $2 \mu\text{m}$  variability in observed first shock speed and shock coalescence distance, small contributors compared to the laser performance tolerances described above. Based on the simulations shown in Figure 11 and these analytic estimates, the accuracy required in setting coalescence depth is set at  $\pm 6 \mu\text{m}$  in Table I.

The systematic error in VISAR traces is  $\pm 5\%$  of a fringe shift<sup>88</sup>, with an additional random variability of  $\pm 5\%$  per temporal resolution element. The temporal resolution is 30 ps, set by dividing the required 6 ns sweep (to cover from first shock break-out at about 8 ns to at least 1 ns after the 12.5 ns coalescence time) by the number of 100  $\mu\text{m}$

resolution elements across the 2 cm central part of the sweep<sup>90</sup>. The second random component is hence negligible averaged over typical ns observation times. Hence, for the higher sensitivity channel set at 3.1 fringes/20 $\mu$ m/ns, the fractional accuracies of the inferred velocities for the 20  $\mu$ m/ns first, 37  $\mu$ m/ns second and 65  $\mu$ m/ns third shocks are  $\approx$  1.6, 0.9 and 0.5%, well within the tuning requirements. The accuracy in coalescence distance is the quadrature sum of velocity and timebase errors. The 1.6% systematic first shock velocity error that dominates represents  $\pm 1.3$   $\mu$ m over an 80  $\mu$ m travel distance in D<sub>2</sub>. By contrast, the accuracy in defining the time between the first shock break-out and successive shock overtake will be a small fraction of the 30 ps temporal resolution, typically 10 ps, hence  $\approx$  0.2% over the 4.5 ns first shock transit time in the liquid D<sub>2</sub>. The contribution from the residual uncertainty in calibrating in situ the sweep speed using an optical comb fiducial<sup>91</sup> is expected to be 1% for both shock velocities and coalescence depth, as long as any non-reproducible sweep speed non-linearities occur over periods longer than the 330 ps fiducial comb spacing.

The viability of this tuning technique was successfully tested<sup>70</sup> in phases at OMEGA. First, we proved that the quartz window capping the liquid D<sub>2</sub> will not blank<sup>92</sup> due to ionization from NIC-relevant levels of hard x-rays ( $> 2$  keV) emanating from Au laser plasmas that can be transmitted through a surrogate ablator BeCu sample. Second, we demonstrated strong reflection off shock fronts traversing a NIC-scale liquid-D<sub>2</sub> filled cone equipped with a planar (rather than spherical due to limitations on hohlraum size at OMEGA power levels) BeCu ablator of matched areal density (see Figure 12). The hohlraum conditions were again designed to be a stringent test of window blanking by delivering up to 10x more Au M-band radiation ( $> 2$  keV) than expected during the third

shock phase of NIF. We note that the other ignition capsule ablator designs, CH and HDC have about 2x the optical depth to these  $> 2$  keV x-rays, and will be even less at risk of window blanking. Third, we demonstrated VISAR measurements off overtaking shocks in the spherical converging geometry and shock strengths of interest by switching to mm-scale directly-driven liquid D<sub>2</sub>-filled CD capsules equipped with cones. Blanking of the D<sub>2</sub> was observed above third shock velocities (above 70  $\mu\text{m/ns}$ ), attributed to preheat from the shock front. This expected result has led to applying a different technique for monitoring the 4<sup>th</sup> shock as described in the next section.

### **C. Timing of 4<sup>th</sup> Shock**

As for the second and third shocks, a correctly timed 4<sup>th</sup> shock (overtaking the first three shocks only after they have coalesced per Figure 10) is critical for keeping the fuel adiabat low for maximum compressibility. Too early a 4<sup>th</sup> shock will lead to 4<sup>th</sup> shock overtake in the fuel and an increase in entropy. In addition, too fast a 4<sup>th</sup> rise at any launch time leads to too strong a 4<sup>th</sup> shock and increased entropy. Finally, too late or long a 4<sup>th</sup> rise delays the onset of peak power and leads to poorer coupling of the main drive to the capsule since its surface area is continually shrinking after the first three shocks' passage, resulting in reduced implosion velocity at fixed peak power. A convenient parameterization for the 4<sup>th</sup> rise is the mid-point time that sets the 4<sup>th</sup> shock coalescence time and its duration that sets the shock strength. This is schematically depicted in Figure 14 where the dashed 4<sup>th</sup> rise laser power profile launches an earlier shock, but given a slower rise, a weaker hence slower shock leading to the same shock

coalescence time as for the solid curve profile. Figure 15 quantifies the calculated sensitivities of average fuel entropy and peak implosion velocity deviations from nominal as a function of changes in the laser pulse 4<sup>th</sup> rise mid-point time (for fixed duration) and 4<sup>th</sup> rise duration around the optimum values. Specifically, Figure 15a shows that entropy increases if either the midpoint time in the 4<sup>th</sup> rise is too early or if the 4<sup>th</sup> rise duration is too short. Conversely, Figure 15b shows that the implosion velocity decreases as the time to reach peak power (i.e. the sum of the 4<sup>th</sup> rise midpoint time and half the duration) is delayed. For example, a 200 ps delay in reaching peak power at a time when the capsule combined first three shock induced particle velocity is  $\approx 50 \mu\text{m/ns}$  should lead to a 10  $\mu\text{m}$  radius or 2% capsule surface area shrinkage, hence a 1% drop in peak implosion velocity, as shown in Figure 15b. To maintain the entropy and peak velocity to 1% of their design values and hence by Eq. (1) the ITF to 10% of its design value requires  $\pm 100$  ps tuning accuracy on 4<sup>th</sup> rise mid-point time and duration. Applying the same kinematic analysis as for the first 3 shocks, with  $c_4 \approx 4$  per Figure 11a, the budgeted  $\Delta t = \pm 100$  ps tolerance in 4<sup>th</sup> shock midpoint time leads to  $\Delta T_4 \approx \pm 135$  ps, and for an allowed variability in 4<sup>th</sup> shock velocity  $\Delta u_4 = 2\%$  over a 3 ns transit time leads to  $\Delta T_4 \approx \pm 40$  ps.

While the clear path to setting the 4<sup>th</sup> pulse timing was quickly recognized to be through measuring shock break-out time through an opaque witness plate<sup>93</sup>, several options have been considered for setting the 4<sup>th</sup> rise duration or slope. These include using a stepped witness plate to measure the coalesced 4<sup>th</sup> shock velocity from the differential shock break-out time, using an absolute measurement of the brightness of the shock break-out, and using Dante to measure the rate of 4<sup>th</sup> pulse hohlraum temperature rise. For the first option, a  $\pm 100$  ps shock transit time change over the  $\approx 2.5$  ns transit

time of the 4<sup>th</sup> shock would appear to translate to an experimentally realizable<sup>93</sup>  $\pm 4\%$  shock velocity accuracy from a stepped witness plate. However, it is the  $\pm 50$  ps tolerance between the 4<sup>th</sup> rise mid-point setting the shock break-out time and the 4<sup>th</sup> rise end-point setting the final shock strength that is relevant here (see Figure 14). This leads to a tighter  $\pm 2\%$  shock velocity accuracy requirement, difficult to meet for a shock breakout technique for which both witness plate and streak timebase errors contribute. For the second option, the brightness temperature of the shock<sup>65</sup> scaling  $\approx$  as the square of the shock velocity would have to be monitored to  $\pm 4\%$  absolute accuracy in the optical Rayleigh-Jeans part of the blackbody spectrum, a difficult calibration proposition and subject to a systematic interpretation error due to any preheat taking it off the Hugoniot<sup>66</sup>. For the third option, the 4<sup>th</sup> rise laser power slope and hence duration can be directly related to the slope in  $T_r$  between  $\approx 10$  and  $11.5$  ns on Figure 2c. For a nominal 4<sup>th</sup> rise slope of  $56$  eV/ns averaged over the  $1.6$  ns 4<sup>th</sup> rise shown in Fig. 2c, an uncertainty of  $\pm 0.1$  ns corresponds to  $56 \times \pm 0.1 / 1.6 = \pm 3.5$  eV/ns in  $T_r$  slope. We have chosen the latter technique as it provides an achievable, orthogonal constraint in the parameter space of 4<sup>th</sup> rise duration and mid-point time as shown by the black contour lines in Figure 15.

Figure 16a shows the keyhole target design<sup>94</sup> modified from that used for the first three shocks that will be used for tuning the 4<sup>th</sup> shock characteristics using the VISAR, an associated Streaked Optical Pyrometer (SOP)<sup>95</sup>, and the Dante. The 4<sup>th</sup> shock geometry uses an identical re-entrant Au cone as for the first three shocks, but with a closed  $20\text{-}\mu\text{m}$ -thick Au tip, spherically concentric with the ablator, with liquid  $D_2$  only between ablator and cone tip. The distance between the inside of the ablator and the outside of the tip is set to measure the 4<sup>th</sup> shock  $\approx 100$   $\mu\text{m}$  ( $\approx 1$  ns) after it has coalesced with the prior 3

shocks. The Au end-piece serves as a witness plate that lights up in the optical regime when the 4<sup>th</sup> shock breaks-out, its high Z providing hard x-ray preheat shielding to avoid pre-expansion of its surface facing the SOP and potential temporal smearing of the shock break-out signature. The SOP uses the same line-of-sight, optics and cross-timing system as the VISAR, which will be essential for minimizing experimental timing offsets between these two diagnostics and for cross-timing to  $\pm 50$  ps with respect to the earlier first 3 shock timing campaign. The SOP is equipped with a  $600 \pm 40$  nm bandpass filter, to avoid contamination from the 690 nm VISAR laser light and the 527 nm residual NIF laser second harmonic. Based on Nova<sup>93</sup> and OMEGA<sup>66</sup> experience, the expected accuracy in defining the risetime of the shock breakout signal on the SOP is  $\pm 25$  ps. The contribution from the residual uncertainty in the sweep speed timebase after in situ correction using the 3 GHz optical comb fiducial is expected to be  $\pm 30$  ps.

The Dante has a fixed view at  $37^\circ$  to the hohlraum axis through the bottom LEH, near optimum for spanning both the inner and outer cone plasmas but not the capsule. More importantly, the average azimuthal location of the Dante view is within  $40^\circ$  of the wall area facing the capsule surface diagnosed by VISAR and SOP. The principal errors in decreasing importance for the Dante Tr slope measurement are the uncertainty in the time-dependent LEH closure to soft x-rays, the uncertainty in the correspondance between the Dante measured wall flux and the average flux at the capsule, Dante component calibrations errors between 160 and 250 eV temperature spectra, residual scope timebase calibration errors, and residual errors in the 60 m signal cable dispersion compensation. A time-integrated multichannel 0.9 and  $>2$  keV imager<sup>96</sup> with 100 and 50  $\mu\text{m}$ -resolution viewing at  $18^\circ$  to the hohlraum axis will be used to infer the average LEH



size<sup>97</sup> during the 4<sup>th</sup> rise. Based on simulations showing up to 10% LEH diameter closure by peak power (at  $Tr = 250$  eV) representing a current overprediction of  $\approx 25\%$  on estimated 3% accuracy measurements, there will likely remain a  $\pm 5\%$  uncertainty in LEH area closure rate translating to a  $\pm 3$  eV uncertainty over a 1.6 ns-long 4<sup>th</sup> rise, hence an error of  $\pm 2$  eV/ns. From simple viewfactor<sup>78</sup> arguments, the uncertainty in the ratio of x-ray flux measured by Dante to flux on the capsule is dominated by the uncertainty in relative fraction of laser illuminated solid angle to total wall solid angle  $\Omega_W$  seen by Dante versus the capsule divided by the ratio<sup>3</sup>  $F$  of recirculating flux to laser spot flux. For a plausible 20% error in the ratio of illuminated wall fractions to account for uncertainties in relative brightness (i.e. due to cone-to-cone power transfer) between cones subtending different solid angle to Dante and to the capsule, and with  $F = \alpha / [(1-\alpha) + (\Omega_{LEH} + \Omega_{Caps}) / \Omega_W] \approx 2$  for a typical 4<sup>th</sup> rise albedo  $\alpha \approx 0.7$ , this gives a 10% error in relative flux and hence  $\pm 2.6$  eV over 1.6 ns =  $\pm 1.6$  eV/ns. The Dante calibration slope error is estimated as the absolute error<sup>78</sup> of  $\sqrt{2} \times 4$  eV at these  $Tr$  multiplied by the 20% fraction of energy channels recording the bulk of the spectrum that are not common at 160 vs 250 eV, yielding  $\pm 1$  eV over 1.6 ns, hence  $\pm 0.6$  eV/ns. The Dante oscilloscope timebases that show up to 7% deviations from the nominal trace speed are correctable over the long term to 1% accuracy averaged over all significant channels and over the 1.6 ns 4<sup>th</sup> rise duration, hence representing a  $\pm 0.6$  eV/ns error. The uncertainty in the typical 20% signal cable risetime compensation is estimated at  $\pm 3\%$  error in flux rise based on variability in deconvolution technique results during the NEL campaign, hence  $\pm 0.8\% \times 56$  eV/ns =  $\pm 0.4$  eV/ns. These four uncertainties added up in quadrature remain less than the  $\pm 3$  eV/ns budget.

3D Hydra simulations<sup>89</sup> predict <1% differences in hohlraum flux at the ignition capsule and at the ablator facing the SOP line-of-sight during the 4<sup>th</sup> rise, which translate to < 0.5% uncertainty in shock velocity correction and hence negligible  $\pm 10$  ps uncertainty in shock breakout time. A plausible unmeasured 2%  $P_2/P_0$  flux asymmetry due to uncertainties in the rising albedo and differential cone backscatter losses during the 4<sup>th</sup> rise would lead to a  $\pm 30$  ps break-out time error over the  $\approx 3$  ns transit time of the 4<sup>th</sup> shock. The uncertainty in 4<sup>th</sup> shock-relevant speeds between liquid D<sub>2</sub> and solid DT are estimated at  $\pm 0.5\% = \pm 15$  ps over the 3 ns 4<sup>th</sup> shock transit time.

Figure 16b shows the starting point inner and outer pulse-shapes, truncated at peak power since simulations show the rest of the pulse has no impact on 4<sup>th</sup> shock arrival time or strength. Based on the measured shock break-out time and Dante 4<sup>th</sup> rise slope between about 160 and 250 eV, the midpoint on the 4<sup>th</sup> rise and rise duration would be varied between shots without changing the earlier pulse profile or the peak power.

The viability of using the VISAR and SOP for this re-entrant witness plate shock breakout measurement was successfully tested<sup>70,94</sup> at OMEGA using the experimental set-up shown in Figure 17a. To test the system under the hard x-ray background expected at NIF at up to peak power, we drove the hohlraum to 230 eV over 1 ns, but with up to 12x more M-band x-rays because the OMEGA beams were at higher intensity than expected at peak power on NIF. A VISAR trace with superimposed self-emission typical of an SOP signature is shown in Figure 17b. While the VISAR signal is first lost due to hard x-ray preheat-induced expansion for the thinner ( $< 35$   $\mu\text{m}$ ) Au witness plates (at 4-5 ns), an abrupt rise in optical signal upon thermal shock break-out is observed at later times. These experiments also showed that a sufficiently thick (40- $\mu\text{m}$ ) Au witness

plate can delay significant preheat-induced expansion until after the thermal shock has broken out at a time in agreement with simulations. Moreover, calculations using the lower fraction of M-band preheat expected for NIF hohlraums due to lower beam intensities predict 20- $\mu\text{m}$ -thick Au witness plates should be viable at NIF for ensuring the soft x-ray driven 4<sup>th</sup> shock breaks out before the preheat induced shock. Since the 4<sup>th</sup> shock transit time through such a Au witness plate is predicted to be 500 ps, a plausible  $\pm 5\%$  uncertainty in shock velocity in Au would contribute a  $\pm 25$  ps error to 4<sup>th</sup> shock timing. Simulations also show that preheat-induced expansion of the Au witness plate facing the capsule ablator leads to a  $\pm 10$  ps uncertainty in shock transit time for a maximum plausible 30% measurement error in M-band fraction during the 4<sup>th</sup> rise. The full roll-up of errors for all techniques will be tabulated later.

The fidelity and repeatability of the main part of the drive as measured by Dante (see Figure 18a) was evaluated for several NIF shots using 5.44 mm diameter hohlraums driven with 19 ns-long 840 kJ 300 eV CH design pulses. Fig. 18b shows that a blow-up of the 4<sup>th</sup> rise portion between 170 and 220 eV between 15.5 and 17 ns met the expected slope of 48 eV/ns within  $\pm 4$  eV/ns, close to the requirement of  $\pm 3$  eV/ns, even though the drives at peak power varied, ascribed due to differential backscatter from changing cone wavelength separation and gas-fill.

#### **D. Ablator Mass Remaining and Implosion Velocity**

For a given ignition design characterized by a peak laser power and laser energy, choice of hohlraum and capsule type and size, and initial assumptions on hohlraum and

capsule coupling efficiency, there is an optimum setting for the combination of peak implosion velocity and amount of ablator mass remaining at implosion stagnation. An initially thin capsule can be driven to high implosion velocity in 1D, but per the rocket equation<sup>3</sup>, that leads to little residual ablator mass remaining, hence enhanced feed-through of Rayleigh-Taylor instability growth and eventually to DT fuel preheating by x-rays. An initially thicker capsule will be more immune to shell break-up by hydroinstabilities, but reach insufficient peak implosion velocity to provide enough PdV work to ignite the hotspot. To maximize the product of the implosion velocity term and mix term of the ITF (Eq. 1) that vary in opposite directions as the initial ablator mass is varied, we need to understand their dependencies on the remaining mass  $M_r$ . From the rocket equation, the sensitivity to  $M_r$  is given by:

$$\Delta M_r / M_r = -\left(v_i / v_{ex}\right) \left[ \left( \Delta v_i / v_i \right) - \left( \Delta v_{ex} / v_{ex} \right) \right] \approx -3 \left( \Delta v_i / v_i \right) \quad (5)$$

where the final approximation is for a typical peak implosion velocity  $v_i$  of 360  $\mu\text{m/ns}$ , exhaust velocity  $v_{ex} = \sqrt{(Z\text{Tr}/m_i)} \approx 120 \mu\text{m/ns}$  and hence fractional mass remaining of  $M_r/M_i = \exp(-v_i/v_{ex}) \approx \exp(-3) \approx 5\%$ . Eq. (5) suggests the scaling  $v_i \sim M_r^{-1/3}$ . Including the fact that the Be ignition design apportions about 60% of the final mass to DT fuel to balance the risk of feedthrough to the hot spot of hydroinstability growth seeded at the ablator-fuel interface<sup>67,68</sup> with the risk of preheating the fuel, we have the final ablator mass remaining  $M_a$  scaling locally as  $M_r^{2.5}$ , hence  $v_i \sim M_a^{-1/7.5}$ . If we first consider the case where the peak power  $P_L$  is varied, since  $v_i \sim \sqrt{P_L}$  and  $v_{ex} \sim \sqrt{\text{Tr}} \sim P_L^{1/7}$ , there is partial cancellation per Eq. (5) leading to  $v_i \sim M_a^{-1/5.4}$ . close to the  $v_i \sim M_a^{-1/5.2}$

scaling found in full radiation-hydrodynamic simulations. By contrast, capsule only calculations typically show  $v_i \sim M_a^{-1/12}$  and  $\sim M_a^{-1/27}$  when we just choose to vary the thickness (hence initial mass) of the capsule by changing the inner or outer radius, respectively. The large difference in scalings is attributable to the nearly self-regulating dynamic<sup>98</sup> of a spherically converging system. For example, by increasing the initial outer radius, the absorbed energy is increased due to starting with a larger surface area, partly compensating for the extra payload mass. However, a larger capsule also represents a larger hohlraum energy sink, hence we would expect the true  $v_i$  vs  $M_a$  power law with changing capsule thickness to be an admixture of the constant flux and constant thickness scalings. For example, a 10% thicker capsule equates to 2% larger diameter, hence 4% larger area and for typically 25% hohlraum drive coupling to the capsule, a 1% sink in drive fluence. By Table II, +10% in thickness compared to -1% in fluence equates to -3% vs -0.5% in  $v_i$ , hence we expect the final power law to be  $1/6^{\text{th}}$  of  $-1/5.2$  and  $5/6^{\text{th}}$  of  $-1/27 = -1/16$ , thus  $v_i \sim M_a^{-1/16}$ . This still leaves us the option of choosing the two adjustable laser and capsule parameters, in this case the peak power and the outer radius for changing thickness keeping the initial radius fixed, that are most different in their relative dependencies on  $v_i$  and  $M_a$ , for simultaneously controlling  $v_i$  and  $M_a$ . The choice of changing the outer versus the inner radius to change the ablator thickness is also clearly preferable from a target coating process point of view.

To calculate the optimum mass remaining, we fit the results of hydrodynamic simulations plotted as squares in Figure 19 that show that the  $\Delta R_{\text{mix}}/\Delta R_{\text{fuel}}$  term in the ITF equation, representing the fraction of DT fuel mixed with hotter ablator making it less compressible and hence useful, varies  $\approx$  as  $0.023/(M_a/M_i)^{1.7}$  or  $2.3/M_a^{1.7}$ , with  $M_a$  now in

units of % of initial mass  $M_i$ . Substituting the dependencies on  $M_a$  in the product of the implosion velocity and mix terms in Eq. (1), we are left with finding the maximum of  $(1/M_a)^{0.5}[1-2.3/M_a^{1.7}]^{0.5}$  that occurs for  $M_a = 2.9\%$  and a mix fraction = 37%. The starting point design value for the peak implosion velocity represented by the denominator 380  $\mu\text{m/ns}$  in Eq. 1 is a result of such an optimization based on detailed hydrodynamics calculations allowing a mix fraction  $\Delta R_{mix}/\Delta R_{fuel} = 30\%$  and a corresponding 3.5% ablator mass remaining. The uncertainty on the 30% value has been set conservatively based on the complexity of modeling mix<sup>99,67</sup> at  $\pm 20\%$  mix fraction, corresponding to a possible 16% reduction in ITF. From the above  $2.3/M_a^{1.7}$  mix fraction sensitivity, this dictates an acceptable uncertainty in ablator mass remaining at  $\pm 1\%$  of the initial mass. Due to the self regulating effect described above, that in turn translates to setting the initial ablator thickness to only  $\pm 6\%$ , or  $\pm 10 \mu\text{m}$  precision. To ensure a balanced  $\pm 16\%$  variability in ITF, the accuracy in setting the peak implosion velocity has been set at  $\pm 2\%$ , representing a  $\pm 4\%$  accuracy in setting peak flux as listed in Table I. Comparing the 300 eV CH(Ge) design with the 285 eV Be(Cu) design, the ratio  $v_i/v_{ex}$  is by design less ( $\approx 2.5$  with  $v_i = 360 \mu\text{m/ns}$ ) to leave more (10%) ablator mass remaining to counteract less ablative stabilization of hydrodynamic instabilities due to the lower ablation rate<sup>108</sup> of the higher Z ablator. The calculated dots on Figure 19 for various thickness CH(Ge) capsules shows that the same  $\pm 1\%$  accuracy in ablator mass remaining will be required to keep the mix fraction within tolerable limits.

Table II summarizes the expected Be(Cu) design sensitivities of three observables (ablator mass remaining, peak implosion velocity and bangtime) to 10% increases in the capsule thickness (for fixed inside radius), peak laser flux, ablator thermal opacity and

M-band fraction around the optimum point (380  $\mu\text{m}/\text{ns}$ , 3.5% ablator mass remaining). Figure 20 graphs the expected sensitivity of the two principal observables, mass remaining and implosion velocity to initial capsule thickness for varying outer radius (the red constant peak flux contours spaced by 10 % in peak flux) and to peak flux (the black constant thickness contours spaced by 7 % in thickness). In general, both parameters will have to be varied to reach the required regime in peak implosion vs. ablator mass remaining space shown as the box on Figure 20.

We experimentally and computationally evaluated various approaches for measuring the ablated or remaining mass, including Cu dopant activation by DT burn neutrons<sup>11,73</sup>, shock-flash or burn proton spectroscopy<sup>100,101,102</sup> using wedge-range filters in front of charged particle CR-39 foil detectors (WRF), tracer emission burnthrough spectroscopy<sup>103</sup>, x-ray burnthrough<sup>65</sup>, and x-ray gated or streaked radiography<sup>104</sup>. The nuclear activation technique's principal drawbacks are contamination from other sources of Cu in the chamber, and interpretation of shell  $\rho\Delta r$  in the face of difficult to calculate Cu mix between the last Cu-doped layer and the 5- $\mu\text{m}$ -thick initially pure Be ablator inside layer (see Figure 2b) which is the principal source of remaining ablator mass. In addition, the technique does not port easily to the CH(Ge) and HDC(Mo) designs without adding special tracers.

The D-<sup>3</sup>He 15 MeV protons are created both during shock coalescence at the center of the capsule gas-fill (occurring at a shell radius of about 250  $\mu\text{m}$ , 400 ps before bangtime and commonly denoted shock-flash) and at peak compression, commonly denoted bangtime. To use the peak compression protons would require a higher-fill lower convergence implosion to keep the final shell  $\rho\Delta r$  well below the ignition design value of

0.4 g/cm<sup>2</sup> to avoid protons ranging out after 0.2 g/cm<sup>2</sup>. Such a higher fill leads to loss of trajectory fidelity due to earlier deceleration. By contrast, the expected total areal density during shock flash is only 0.06 g/cm<sup>2</sup>, leading to an easily observable  $\approx 2.5$  MeV downshift of protons born at that time. The principal issue with the shock flash proton spectroscopy is that the unablated shell areal density we are interested in is only 50% of the measured total areal density for the optimum mass remaining. Specifically, calculations show that the total areal density only increases 20% for a 2x increase in ablator mass remaining, with 10% scatter in this correlation, hence leading to only a 25% accuracy in inferring the unablated areal density. This is in contrast to OMEGA implosions<sup>105</sup> for which the unablated areal density at shock flash dominates since the mass remaining is typically 3x greater due to the lower implosion velocities reached per Eq. (5). Moreover, the mass remaining  $\sim r^2 \rho \Delta r$  will be most sensitive to the  $r^2$  term, hence the shell radius at shock flash, not a direct observable unless the protons bursts are time-resolved<sup>106</sup>. Both the activation and burn proton spectroscopy techniques would use the nuclear bangtime<sup>107</sup> (either from neutrons or gamma-rays) to infer peak implosion velocity for which  $\pm 2$  % in implosion velocity over the 3 ns peak drive phase shown in Figure 2c is equivalent to a measurable  $\pm 60$  ps in bangtime. However, both bangtime pr and bangtime are more integrated measurements that can be directly affected by late time mix.

Burnthrough techniques are difficult to transpose from their usual planar geometry to a re-entrant keyhole-like geometry for better fidelity, because unlike shock timing, one must follow the capsule for at least 2/3 of its trajectory before it is ballistic. However, a series of planar x-ray burnthrough experiments<sup>108</sup> have been carried out at the OMEGA



facility on all 3 ablator candidates at up to NIC-relevant peak radiation temperatures ( $T_r \approx 270$  eV). They have constrained our understanding of the ablation rates to  $\pm 5\text{-}10\%$ , corresponding to  $\pm 3\%$  in remaining ablator mass when including uncertainties in transposing to a convergent system,  $= \pm 80\%$  of the  $3.5\%$  optimum ablator mass remaining as listed as the initial uncertainty on Table I.

We elected to use time-resolved x-ray radiography that will extract through Abel inversion the time-resolved ablator density profile from which remaining mass, areal density, position, and velocity of the ablator as a function of time can all be derived. Like the *pr* measurements, it has the advantage of measuring the small fraction of remaining mass for an ignition capsule design that has a much larger fractional tolerance than the ablated mass sensed by burnthrough techniques. Specifically, even accounting for adding  $5\%$  extra Be mass to these non-cryogenically layered implosions to match the DT fuel areal density, the required accuracy in the mass remaining observable is  $8.5 \pm 1\%$  ( $16 \pm 1\%$  for the current  $300$  eV CH(Ge) design), a  $\pm 7\text{-}12\%$  relative error bar. In addition, we should be able to see an x-ray flash at bangtime for further corroboration of the implosion dynamics. The optimum point in the capsule trajectory for inferring mass remaining and peak implosion velocity has been found to be around  $r = 300$   $\mu\text{m}$ . The shell has not yet started to thicken at a rate comparable to its average implosion speed or reach a thickness comparable to its average radius due to convergence effects, which would impair accurate velocity and mass remaining measurements. Simulations show that  $99\%$  of all the ablator mass that will be ablated is gone by the time the capsule reaches a radius of  $300$   $\mu\text{m}$ , with peak velocity occurring about  $300$  ps later. Moreover, from the results of many simulations using different realizations of laser and target residual shot-to-shot

variations within specifications, we find that the extrapolation errors in ablator mass remaining and peak implosion velocity from measurements taken earlier at  $r = 300 \mu\text{m}$  are 2-3x less than the  $\pm 1\%$  and  $\pm 2\%$  error budgets, respectively.

An example of a calculated 6.7 keV streaked radiograph across a Be capsule diameter and a transmission lineout across the image when the shell has reached the radius of interest are shown in Fig. 21. We note that the minimum limb transmission is designed to be 20-30% by appropriate choice of backlighter energy. This value is chosen based on balancing desirable improved signal-to-noise with deleterious increased sensitivity to uncertainties in correcting for the instrument spatial modulation transfer function (typically 0.8 on limb spatial scales) as the limb contrast is increased. The backlighter energy is also chosen to be below the K edge of the dopant material (9 keV for Cu, 11 keV for Ge) to minimize extra absorption from partially ionized ablated dopant material.

The experimental set-up for NIC is shown in Fig 22a. The capsule is identical to the ignition capsule except that the 75  $\mu\text{m}$  of DT ice is replaced by an equivalent areal density of 10- $\mu\text{m}$  thick Be on the inside, and a DT hot spot equivalent capsule fill density of  $\approx 0.4 \text{ mg/cc}$  is used to maintain fidelity in its trajectory. The radiography source is an area backlighter in transmission mode created using two  $50^\circ$  quads irradiating a 5-7  $\mu\text{m}$ -thick Fe backlighter foil placed on the side of the hohlraum producing 6.7 keV Fe He-alpha (9 keV Zn He-alpha for the CH(Ge) and HDC designs). Slots, 110- $\mu\text{m}$  tall by 1.2-mm long, are cut out of the hohlraum wall opposite each other to allow a fan of x-rays to backlight the capsule equator. They will be filled and encased in  $\approx 150 \mu\text{m}$ s of HDC to delay slot closure<sup>109</sup>, as already demonstrated. We choose to backlight around the equator rather than through the poles since by viewfactor considerations (see Figure 22a)

the equator is least affected by the absence of the 2 missing outer beam quads. Viewfactor analyses also suggest the presence of the modest sized slots (representing < 0.5% of solid angle) and the 2 missing drive quads even if not compensated for will have negligible effect on the perceived trajectory or Abel inversion in the face of the small 1% drive asymmetry. The backlighter quads are equipped with phase-plates creating elliptical 700 by 1200  $\mu\text{m}$  spots to illuminate a 1.5 mm diameter of interest. The 110  $\mu\text{m}$  slot width is chosen to maximize photon throughput while avoiding excessive sensitivity to 20-30- $\mu\text{m}$  misalignments in position of capsule with respect to hohlraum, the far slot, parallax from residual few mrad hohlraum tilt, and residual capsule  $P_1$  or  $m=1$  drive asymmetry. To avoid saturating the streak camera electron optics leading to space charge distortion effects by the self-emission flash expected to be 10,000x brighter at bangtime on axis, we will use a high Z block over the central 50-100  $\mu\text{m}$  of the field-of-view. We calculate that a bangtime flash of similar strength to the backlighter should still be seen from Compton scattering from the hohlraum fill and ablator plasmas. Calculations with simulated data show the partial absence of radiography data should have negligible effect on the required accuracy of the Abel inversion for extraction of the various moments of the limb profile. A 16x magnification 1D imaging system<sup>110</sup> equipped with a 20- $\mu\text{m}$ -wide slit set orthogonal to the slots casts a 1D-resolved image onto an x-ray streak camera photocathode providing a 4 ns sweep with 30 ps resolution. The slit width is chosen to maximize throughput by matching the expected limb widths. A 4 $\omega$  UV comb fiducial<sup>111</sup> has been designed to provide 100 ps pulses every 300 ps in a 2 ns train for correcting for any local sweep speed deviations and non-linearities in situ at the required level of accuracy of  $\pm 1\%$  over a 300 ps measurement interval.

An alternate experimental design has been fielded recently using multiple short slit imaging onto an x-ray framing camera spanning  $\approx 1$  ns of the capsule trajectory. This has the advantage of a fixed gate propagation speed and interstrip timing that can be calibrated and shown to be repeatable to 1-2 % accuracy. It has the disadvantage of poorer time resolution (70 ps currently, 35 ps possible on the future) leading to more motional blurring of the radiographed limb (25  $\mu\text{m}$  at 350  $\mu\text{m}/\text{ns}$  currently). The plan is to compare both the streaked and gated x-ray radiography results to increase confidence in both before choosing one for the remaining shots. In addition, the capsules will be filled with a mixture of D- $^3\text{He}$  to gather an independent measure of total capsule areal density during shock flash from the proton slowing as measured by the WRFs. We are also designing a suitably-dudded cryogenically layered version of this in-flight capsule radiography technique as a final check of surrogacy.

Figure 22b shows that the hohlraum is driven with the full pulseshape for best fidelity. The baseline backlighter pulseshape is a  $\approx 2$  TW/beam pulse, kept short to maximize power given energy limits but suitably delayed and long enough at 1.5 ns to cover the time-frame for capturing the  $r = 600$  to  $r = 200$   $\mu\text{m}$  phase of a capsule imploding on average 300  $\mu\text{m}/\text{ns}$ . We will use a prepulse shown to double the x-ray conversion efficiency of the main pulse<sup>112</sup>. Simple photometrics estimate based on known backlighter efficiencies<sup>113</sup> suggest the shot noise limited accuracy will be sufficiently good to provide  $\pm 3(2)\%$  accuracy in relative mass remaining (vs. the  $\pm 7\text{-}12\%$  required tuning accuracy) and  $\pm 1(2)\%$  accuracy in velocity for the streaked (gated) radiography cases, respectively.

A host of other random errors and systematic errors have been evaluated. For the target, they include uncertainties in initial thickness ( $\pm 1 \mu\text{m}$ , small compared to  $\pm 10 \mu\text{m}$  required tuning accuracy) and in initial ablator areal density and dopant fractions ( $\pm 1\%$  and  $0.1\%$ , leading to  $\pm 3\%$  in relative mass remaining). The major uncertainty, however, lies in the  $0.25\%$  Ar fraction by atom required for ensuring adequate Be coating uniformity (not present for CH or HDC designs). Since the Ar contributes about  $45\%$  to the remaining ablator opacity at  $7\text{-}8 \text{ keV}$ , the demonstrated Ar characterization accuracy<sup>114</sup> of  $\pm 0.05\%$  corresponds to  $\pm 9\%$  to the opacity and to the relative mass remaining. For the laser, an expected  $\pm 1.5\%$  uncertainty in peak power delivered corresponds to about  $\pm 3\%$  in the remaining mass, while the shot-to-shot variability will be  $2\times$  larger.

For the physics, errors include uncertainties in unablated material opacities at the backlighter photon energy of interest (contributing  $< 5\%$  to the uncertainty in inferring mass remaining) and in the distribution of remaining Cu or Ge in the presence of hydroinstability growth for properly weighting the ablator opacity. The latter has been estimated based on highly resolved 2D hydrodynamic simulations<sup>67</sup> predicting up to  $10\%$  mixing of  $0.5\%$  Cu-doped Be into the inner pure Be (CH) remaining at the time of interest just before deceleration. Since the unablated opacity of  $0.5\%$  Cu-doped Be is  $2.5\times$  higher than pure Be below the Cu K edge, this provides a  $15\%$  increase in perceived mass remaining if unaccounted for, matching the error budget. We do note that the dominant perturbation mode numbers are sufficiently high ( $100$  corresponding to  $20 \mu\text{m}$  spikes) that the sampling error along the  $110\text{-}\mu\text{m}$  tall line-of-sight will be negligible ( $< 2\%$ ). Should the level of mixing between doped and pure Be or CH prove to be of

greater concern, the back-up plan is to switch to uniformly-doped ablators of equivalent areal density over the inner 15  $\mu\text{m}$ . Separate from the dopant mixing issue, hydroinstability growth will lead to an overestimate of the mass remaining in that the radiographed limb along its line-of-sight will be a mixture of unablated spikes and ablated bubbles. Since 3D simulations show that the bubble and spike mass are similar, the overestimate will be of order the fraction of unablated material that is in spikes (typically 10-20%) times the ratio of residual opacity of the ablated material (dominated by the dopant) to the opacity of the unablated material, also typically 30%, hence a 3-5% effect. Figure 23 provides an upper bound on the effects of Rayleigh-Taylor (RT) growth on the radiography by comparing simulated transmission lineouts at near peak velocity with and without ablation front RT growth for the same mass remaining (15%). It is based on a current 300 eV, 1.3 MJ CH(Ge) design<sup>7</sup> using a 9 keV backlighter and assuming 70  $\mu\text{m}$ -long spikes at the mass fraction assumed above. It shows that such RT spikes should show up as a 70  $\mu\text{m}$ -wide 20%-level absorption wing outside the main limb, alerting us that a 3-5% correction for ablated bubbles carrying residual dopant opacity between spikes is required.

An experimental demonstration<sup>72</sup> of the streaked radiography technique on 0.5-mm-diameter graded-doped Be(Cu<sub>0.03</sub>) capsules driven by 200 eV, 2.5 ns-long shaped drives was completed at the OMEGA facility using a similar set-up as planned for NIF. The experiments were designed to check backlighter uniformity, sensitivity to thickness and to position of the Cu dopant which was even a greater contributor to the optical depth here due to the higher concentration of Cu required to approximate the same level of optical depth as for NIC with a smaller capsule. A typical streaked radiograph at the V

He-alpha 5.2 keV line is shown in Figure 24a. The Abel-inverted analyzed results plotted in terms of pairs of measured peak velocities versus inferred ablator mass remaining are shown in Figure 24b for two different initial thickness capsules. Overplotted as squares are the Lasnex postshot calculations. We note that the statistical accuracy on its own met the  $\pm 1\%$  of the initial mass requirement despite having 3-4x larger fraction of the mass remaining than expected for NIC implosions. In addition, Figure 24b shows that the data with the lowest statistical inaccuracy just met the  $\pm 2\%$  peak implosion velocity accuracy (no in situ fiducial was used). Despite the scatter in the data for the nominally identical shots, it is promising to see that all the points follow the expected trend of less mass remaining if higher velocity. Specifically, for the conditions of this experiment,  $v_i/v_{ex} = 130/100 = 1.3$ , hence expect  $\exp(-1.3) \approx 30\%$  mass remaining as seen. Equation (5) then predicts a slope of  $dM_r/M_r \approx -dv_i/v_i$ , also close to what is observed.

### **E. Peak Drive Symmetry**

The time-integrated imploded core symmetry is mainly set by the drive symmetry during the peak power phase of the pulse. For example, a 0.4% applied  $P_2$  flux asymmetry will lead to a core asymmetry magnified<sup>71</sup> by the (convergence ratio (CR) – 1), yielding a 15%  $P_2$  on the ignition capsule hot spot. The close to cubic power law in the symmetry term in the ITF reflects the fact that a  $\Delta R/R$  relative distortion of the hotspot of radius  $R$  will reduce the burnable spherical volume by  $3\Delta R/R$ , requiring  $3\Delta R/R$  more energy to recover that volume by increasing the scale by  $\Delta R/R$ . The power law is greater than cubic to reflect the more damaging effect of more penetrating isolated

jets of ablator material causing radiative cooling of the hotspot<sup>47</sup>. The specification on the acceptable rms hotspot asymmetry listed in Table I is set at 16% making it the largest contributor to reducing the ITF, about a factor of 2 from its nominal 1D value. The rms hotspot asymmetry is based on the quadrature sum of calculated growth of known residual low and mid-mode imperfections of the shell and DT fuel<sup>115</sup> and from expected post-tune drive asymmetries. The drive asymmetry budget is further divided into 9% rms for intrinsic tuning errors and 7% for random asymmetries due to power imbalances. In terms of Legendre modes applicable to these cylindrical hohlraums (neglecting for the moment non  $m=0$  modes), the intrinsic asymmetry budget further breaks down as  $7\sqrt{5} \approx 15\%$  in  $P_2$  and  $5\sqrt{9} = 15\%$  in  $P_4$  coefficient since an rms value =  $P_n$  coefficient /  $\sqrt{(2n+1)}$ .

We will control  $P_2$  and  $P_4$  independently by a combination of changing the peak power ratio between laser beam cones and by changing the hohlraum length and axial displacement of the cone pointing defined by the intersection point of all beams within a cone. Besides the traditional technique of changing the input laser power on a cone-by-cone basis, we have also recently shown control of core  $P_2$  asymmetry through power transfer between cones due to three-wave mixing<sup>116</sup> where they cross in the flowing LEH plasmas, controllable by just changing the relative wavelengths of the cones<sup>6</sup>. Similarly, the choice of either changing the hohlraum length and pointing or just the pointing depends on the amount of clearance for the spots with respect to the LEH edges.

By the peak drive portion of the pulse, simulations predict that a combination of high  $Z$  inward blow-off from the hohlraum wall and fill-gas densification and refraction from wall and capsule ablation has moved the centroid laser absorption regions  $\approx 1$  mm back along the incoming beam paths. This is shown schematically in Figure 25 by the laser



beam arrows ending at some radius  $r$  before reaching the hohlraum walls. Such simple spot motion analysis (based on either soft<sup>117</sup> or hard<sup>118</sup> x-ray imaging) was successfully used to explain time-integrated<sup>119</sup> and time-varying<sup>120</sup>  $P_2$  asymmetry in vacuum Nova and OMEGA hohlraums. The spot motion in the NIC ignition hohlraums reduces the average angles subtended by the beam absorption locations such that they have moved from being near the  $P_3$  nodes at  $40^\circ$  and  $90^\circ$  to being near the nodes of  $P_4$  ( $30^\circ$  and  $70^\circ$ ). Hence, we again have simultaneous symmetry control for all modes through  $P_5$  by in general applying a different inner to outer cone power fraction than used during the foot portion (close to 1:2, matching the number of beams per cone ratio).

Figure 25 also shows how the core  $P_2$  asymmetry can be varied on its own by changing the inner to outer cone power ratio at the nodes of  $P_4$ . The change in  $P_2$  around zero at the wall due to change in peak cone fraction at the wall  $\Delta CF/CF$  is given by  $[P_2(70^\circ) - P_2(30^\circ)](\Delta CF/CF)/(F+1) \approx 2P_2(70^\circ)(\Delta CF/CF)/(F+1)$ , = 0.7% for a  $\Delta CF/CF = 5\%$  and  $F = 4$  for a typical peak power albedo  $\alpha = 0.85$ . Accounting for a cone averaged radiation transfer function<sup>3</sup> of 60% leaves 0.4%  $P_2$  at the capsule magnified by 35x convergence to 15%  $P_2$  on the hotspot, the budgeted precision. Hence we list  $\pm 5\%$  in required accuracy in setting the peak  $\Delta CF/CF$  in Table I.

To vary  $P_4$ , the key is to change the difference in angle  $\Delta\theta$  subtended by the inner and outer cone spot centroids at the capsule. For example, if one reduces  $\Delta\theta$ , the part of the capsule at a polar angle of  $\approx 50^\circ$  subtending an angle in between the cones will experience greater drive than the parts outside the cones at  $0^\circ$  and  $90^\circ$  (for a spot-to-capsule radius ratio  $< 4$ ), leading to a diamond-shaped core as shown on the right-hand side in Figure 25. One could change  $\Delta\theta$  by simply axially displacing inner and outer cones with respect

to each other, but that would reduce clearance at the LEHs where cones cross, requiring a larger LEH size and reducing hohlraum efficiency, or requiring a smaller spot size increasing intensity and hence susceptibility to LPI instabilities. Thus, in general, we would choose to change the hohlraum length by  $\Delta L$  while keeping the beams locations fixed at the LEH. This moves the inner and outer cones together by  $\pm\Delta L/2$  per side, maintaining their axial separation at the wall, but providing a cone dependent angular change  $= \Delta L \sin^2\theta/2r$ . For example, for  $\Delta L = 400 \mu\text{m}$ ,  $r = 2200 \mu\text{m}$ ,  $\theta = 70^\circ$  and  $30^\circ$ , the change in  $\Delta\theta$  is .057,  $\approx 3^\circ$ . Given  $|dP_4/d\theta| = 2$  near nodes, the change in  $P_4$  at the wall is hence  $0.1/(F+1) = 2\%$ . Accounting for a cone averaged geometric radiation transfer function<sup>3</sup> of 10% leaves 0.2%  $P_4$  at the capsule magnified by convergence to 8%  $P_4$  on the hotspot. Of course, such an overall beam shift will also change the core  $P_2$ , as schematically shown in Figure 25. In this case,  $|dP_2/d\theta|$  is less,  $\approx 1$ , but the average transfer function is much greater at 60%, leading to a 20% change in core  $P_2$ .

Figure 26 shows Lasnex radiation hydrodynamics simulation results of the core  $P_2$  and  $P_4$  asymmetry for a typical 20x convergence symmetry capsule (in this case for a CH(Ge) 300 eV design) as a function of 4<sup>th</sup> pulse inner cone energy fraction for three hohlraum lengths differing by  $\pm 400 \mu\text{m}$ . The optimum hohlraum length per this calculation is represented by the curve in blue for which the core  $P_2$  and  $P_4$  are both near zero (marked by blue point) for the same inner cone fraction of 0.345. The change in  $dP_4/dCF$  slope sign versus hohlraum length in Figure 26 can be explained by fact that the more beam centroids move off the nodes of  $P_4$  through a hohlraum length change, the more the asymmetry becomes sensitive to the cone power balance. The simple analytic model predicts  $dP_4/dCF$  should be zero when  $P_4 = 0$ , while Figure 26 shows that  $dP_4/dCF$

= 0 at a non-zero value of  $P_4$ , ascribed to neglecting mode coupling for a spherical capsule in a cylindrical hohlraum<sup>3</sup>. The analytic predictions, corrected for a 40% reduction in symmetry capsule sensitivity due to 1.8x lower convergence and use of gold versus higher albedo U hohlraums ( $F = 3.5$  instead of 4), do compare well with other simulation sensitivities near the point of best symmetry:  $\Delta P_2 = +9\%$  vs.  $+10\%$  for  $\Delta CF/CF = +5\%$ ,  $\Delta P_2 = -12\%$  vs.  $-10\%$  for  $\Delta L = +400 \mu\text{m}$ , and  $\Delta P_4 = +5\%$  vs.  $+8\%$  for  $\Delta L = +400 \mu\text{m}$ .

The experimental set-up and surrogate symmetry capsule cross-section for peak power core symmetry measurements on NIF are shown in Figures 27a and b. Besides x-ray imaging, we will be simultaneously monitoring the hohlraum Tr profile with Dante, and the neutron bangtime and yield with nToF<sup>107</sup>. As for the convergent ablation radiography measurement, the DT fuel is replaced by an equivalent areal density of pure Be or CH to emulate the ignition capsule trajectory and hence drive symmetry history sampled (see Figure 28). As shown in Fig 27c, the full 1.2 MJ pulse is best for certifying that the symmetry is adequately tuned (to  $0 \pm 7.5\%$  in hotspot  $P_2$  and  $P_4$  as listed in Table I) before proceeding to cryogenic-layered implosions and ignition attempts. However, assuming late-time laser-plasma coupling physics has been assessed and can be accounted for computationally, simulations show that the  $P_2$  and  $P_4$  components vary by only  $\pm 15\%$  for cases where the pulses have been either truncated by  $\approx 0.5$  ns in time or reduced in peak power to 1 MJ levels.

To avoid large core distortions when tuning starts (potentially  $> 40\%$  as listed in Table I based mainly on several  $100 \mu\text{m}$  uncertainties in where the inner cone energy deposits its energy) that can lead to cross-coupling between modes complicating the

inference to drive asymmetry, the capsule convergence ratio will be reduced by filling with 50 atm. of He and H isotopes at room temperature. This corresponds to 8 mg/cc compared to the 0.3 mg/cc DT ignition gas-fill that represents about 1/3 of the final hot spot fill after accounting for partial fuel inner surface ablation. Including the 2x higher temperatures expected of THD cores, we would hence expect for equivalent back pressure =  $nkT$  a reduced symmetry capsule convergence by  $4^{1/3} \approx 1.6x$ . The reduced convergence should have minimal effect on drive symmetry sampled since the capsule trajectories are ballistic a few 100 ps before onset of deceleration. A mixture of He and 5-10%  $D_2$  that remain gaseous at the cryogenic hohlraum conditions will be used for maximizing Bremsstrahlung emission ( $\sim Z^2$ ) and providing a nuclear bangtime at yields below  $10^{11}$  to avoid damage to the CCDs<sup>121</sup> used as recording medium behind the gated x-ray framing cameras<sup>28</sup>.

The x-ray detection is filtered for  $> 7$  keV to provide a strong signal from the predicted 3 keV temperature core self-emission unobstructed by shell reabsorption. The imaging is accomplished through a 500  $\mu m$  diameter CH-tamped hole in the hohlraum by an array of 5-10  $\mu m$  pinholes at 8 – 10 cm casting 12-15x magnification images onto a 4 stripline MCP providing 900 ps of continuous time coverage over 70 ps gate times. 3D Hydra simulations show the hole was not expected to close appreciably before the bangtime at  $\approx 16$  ns, as witnessed experimentally during the 2009 hohlraum energetics campaign. Furthermore, representing 0.1% of the hohlraum wall area, it is a negligible source of asymmetry or loss. In addition, the bandpass is set by the filters at the back of the detector to avoid distortion of the images by potentially non-uniform transmission of the tamped CH that is subject to hydroinstability growth. The expected core x-ray yields

are of order a few J/sr over a few keV at 8 keV, which should provide 2-3% statistical accuracy in decomposing core asymmetries / frame. Besides the equatorial view for assessing Legendre modes, Figure 27a shows that an axial imager is also fielded to check for azimuthal asymmetries such as an  $m = 4$  on the capsule equator due to unexpected differential behavior between the  $23.5^\circ$  and  $30^\circ$  subcones in their absorption, x-ray conversion efficiency or transmitted intensity, the latter for example due to cross-beam transfer<sup>116</sup>.

The data analysis consists of extracting contours from a set of images that span 200 (100) ps x-ray emission duration for convergence ratio 15 (30) implosions. The 20% emission contour appears best correlated to the shape of the hot spot-shell interface we are interested in, and is at a sufficiently large perimeter and low contour level that higher modes such as  $P_6$  could be resolved. In general all contours will provide information. The extracted  $P_2$  component can vary over the x-ray emission duration, but sufficiently slowly that a 70 ps gate for the lower convergence implosions should be sufficient. In general, any  $P_2$  swing means that the peak brightness image will have to be identified for a proper interpretation to simulations. Accounting for a 20% variability in relative pinhole diameters and hence 40% in throughput, and in uncertainty in MCP gain profile corrections, we expect to be able to find the peak emission time to  $\pm 15$  ps, corresponding to a  $\pm 3\%$  uncertainty in core  $P_2$  for a maximum plausible  $P_2$  swing of  $20\% / 100$  ps. This is expected to be an upper limit as recent data (see later Fig. 31b) has shown far smaller  $P_2$  swings. A typical tuning campaign would consist of varying the cone fraction by  $\pm 10\%$  and hohlraum length by  $\pm 400$   $\mu\text{m}$  on separate shots to check sensitivities and interpolate to the optimum tune. The goal of the symmetry capsule tuning campaign is to

set the hohlraum length to  $\pm 200 \mu\text{m}$  and the inner cone power ratio to  $\pm 5\%$  as listed in Table I. In addition, we will be able to confirm peak velocity from either the x-ray bangtime using the brightest gated x-ray camera (to  $\pm 50 \text{ ps}$  when including cross-timing uncertainty) or nuclear bangtime. Finally, we will use full pulse shots such as these to assess the time-resolved  $> 1.8 \text{ keV}$  hard x-ray component using several dedicated high energy Dante channels to an expected accuracy of  $\pm 10\%$ . This uncertainty translates to  $\pm 8\%$  in mix fraction. If the  $> 1.8 \text{ keV}$  fraction at peak power were measured to be say 30% greater than expected, then we would need to increase the ablator dopant concentration. In the recent experiments using CH(Ge) capsules driven by up to 290 eV hohlraums, the  $> 1.8 \text{ keV}$  fraction was indeed 30% larger than the 10.5% predicted using our baseline hohlraum models, leading to an 80% increase in Ge content designed into future targets.

We have computationally evaluated in 3D the fidelity in  $P_2$  and  $P_4$  core shape of symmetry capsules with respect to ignition capsules as shown in Figure 29 for a variety of intentionally mistuned drives. The simulation slopes show the expected higher sensitivity (1.5-2x) for the higher convergence ratio ignition capsules. They also show that the correlation is typically 2x better than the  $\pm 15\%$  ignition core  $P_2$  and  $P_4$  required tuning accuracies, that there is no apparent systematic offset in  $P_2$  but a potential +5% symmetry capsule offset in  $P_4$  corresponding per Figure 26 and Table I to an  $\approx +150 \mu\text{m}$  hohlraum length offset. In addition, 3D simulations show that the presence of random 3D drive asymmetries (usually at modes 1-4) dominated by residual quad-to-quad power imbalances (2% at peak power) only changes the perceived  $P_2$  and  $P_4$  asymmetries from the planned single equatorial line-of-sight by  $\pm 3$  and 2%, small compared to the  $\pm 7.5\%$

budgets (set by dividing the ignition capsule requirements of  $\pm 15\%$  by  $\approx$  the ratio of ignition to symmetry capsule convergences) shown on the last column in Table I.

The symmetry capsule became a robust technique for tuning both vacuum and gas-filled hohlraums<sup>51,52</sup> in Nova hohlraums where changing hohlraum length and/or beam pointing set the time-averaged single beam cone location near the  $P_2$  node. At OMEGA, the NIC concept of setting symmetry by balancing opposite sign  $P_2$  from different beam cones was first demonstrated<sup>122</sup>, followed by rudimentary beam cone phasing<sup>123</sup>. The expected simultaneous improvements in  $P_2$  and  $P_4$  control<sup>124</sup> and associated implosion performance<sup>125</sup> followed. Recently, symmetry tuning at OMEGA has been extended to demonstrating sensitivity to cone fraction using small NIC-relevant case-to-capsule ratios of  $<2.5$  at radiation temperatures approaching 300 eV<sup>101,126</sup>. 1.2-mm-diameter OMEGA hohlraums illuminated with 260 eV, 1-ns-duration  $21^\circ$  and  $59^\circ$  cones imploded 560  $\mu\text{m}$ -diameter 45- $\mu\text{m}$ -thick CH(Ge.<sub>02</sub>) capsules filled with a mixture of 36 atm.  $\text{D}_2 + {}^3\text{He}$ . Figure 30 displays the  $>4$  keV 120- $\mu\text{m}$ -diameter core images recorded and the core  $P_2$  asymmetry extracted vs.  $21.4^\circ$  inner cone energy fraction for fixed total energy. The convergence ratio is small, 4x, attributed to the high level of penetrating preheat for these thickness capsules, leading to an inefficient exploding pusher compression mode for Tr above 220 eV<sup>127</sup> that will not exist for the thicker, NIC capsules driven by higher albedo, lower illumination intensity hohlraums. The symmetry goes to more positive  $P_2$  as expected as the inner cone fraction is increased. Applying the same analysis for the  $P_2$  variation versus cone fraction discussed earlier, for the  $\Delta\text{CF}/\text{CF} = \pm.09/0.21$  applied here, diluted by  $F = 2$  for a peak power albedo  $\alpha = 0.75$  and amplified by the measured convergence  $-1$  factor = 3, yields  $\pm 16\%$  core  $P_2$ , close to the measured  $\pm 10\%$ . In

addition, a  $\pm 1\%$  statistical accuracy in  $P_2/P_0$  was demonstrated as expected, similar to the measurement accuracy predictions for larger NIF capsules. These accuracies have been validated at NIF for 500-1000 kJ hohlraums driving convergence 15x CH(Ge) symmetry capsules<sup>128</sup> imaged at 10 keV with 10  $\mu\text{m}$ , 70 ps resolution (see Figure 31a). Specifically, Figure 31b shows  $\pm 1\%$  variability in core  $P_2$  and  $P_4$  symmetry between images taken within 50 ps of each other for a shot that met  $\pm 5\%$  low mode symmetry requirements.

While the symmetry capsules for NIF are driven on a higher adiabat than ignition capsules due to shocks being left performance mistimed when substituting 75  $\mu\text{m}$  of DT fuel at 0.25 g/cc with 10  $\mu\text{m}$  of Be at 1.85 g/cc, they are driven at lower adiabats than their counterparts at OMEGA. They have a higher in-flight aspect ratio (IFAR) and less mass remaining (comparing for example Figures 20 and 24), and hence will be prone to more feedthrough of hydroinstability growth from residual target imperfections<sup>129</sup>. In addition, the presence of a filltube may lead to injection of a jet<sup>130</sup> of Cu-doped Be (or Ge-doped CH) deep in the He fill, locally increasing the x-ray Bremsstrahlung intensity and distorting the perceived core shape. Both jets traversing cores launched from surrogate filltubes and x-ray bright spots spatially correlated with known capsule surface imperfections were observed in 5  $\mu\text{m}$ , 50 ps gated imaging OMEGA experiments using indirectly-driven Ti-doped CH shells filled with  $\text{D}_2$ <sup>131</sup>. For the CH(Ge) design, we have already confirmed at NIF such signatures of penetration of the Ge dopant using a monochromatic version<sup>132</sup> of the gated imager designed for spectroscopic diagnosis<sup>133, 134</sup> of Ge He-like and H-like lines at 10-12 keV. At the 1 MJ level, the bright spots caused by mixing of doped shell into the gas-fill penetrate ahead of the 20% contour used to infer



core asymmetry and so provide an insignificant bias. If dopant penetration from target imperfections is problematic for core symmetry interpretation at higher drive levels, we will either thicken up capsules or stay with reduced or truncated drives for symmetry measurements as mentioned earlier. The effect of mix between the inside of the Be and the He fill at stagnation on the perceived core asymmetry has also been computationally investigated using different mix models. The simulations show different levels (5-50%) of reduced sensitivity at 20% image contours to a given level of applied asymmetry when including plausible levels of mix, and only predict occasional systematic offsets for high levels of mix. Moreover, we will have indications of levels of mix from measured yields and core sizes ( $P_0$ ).

### III. SHOT PLAN

The goals of the capsule tuning campaign are to deliver the adjustable parameter value and uncertainty in that parameter, and to assess that shot-to-shot variability is as expected (look for unknown unknowns by repeating shots). An illustrative example output plot is shown in Figure 32 for the case of mass remaining vs. initial capsule thickness. A cluster of  $N$  shots at a nominal laser and target setting would be taken to assess the  $1\sigma$  shot-to-shot variability and compare to expectations. The error bars on each data point here are the  $1\sigma$  random measurement error bars, which in the preceding sections have been shown to be less than or comparable to the expected data scatter. Since the standard error in the data scatter  $\sigma$  is  $\approx \sigma/\sqrt{2(N-1)}$ , we expect a 40% error in  $\sigma$  for a reasonable choice of  $N = 4$ , allowing us to detect scatter that is significantly

greater or less than expected. The second step is to correct the data for known preshot shot-to-shot target variations and postshot shot-to-shot laser variations using precalculated sensitivities, examples of which were discussed in the prior sections. This should reduce the scatter in the data to just target and laser diagnostic metrology errors and errors in measuring the observable. In general, the mean of this corrected data will be offset from the optimum value of the observable we are aiming for, precorrected for any known surrogacy offset. The second step is to gather another set of  $M$  data points, where in general  $M < N$  since data scatter has already been evaluated, for another value of the adjustable parameter that would bracket the optimum setting based on the precalculated slope sensitivity of the observable to the adjustable parameter. The optimum value of the adjustable parameter is then found by where the linear interpolation between the 2 datasets crosses the optimum value of the observable. The statistical accuracy in defining the optimum setting for the adjustable parameter will then be  $= \sigma/\sqrt{(M+N)}/\text{mean slope}$ . Finally, one will have to add in quadrature systematic errors due to uncertainty in surrogacy, physics of the technique and calibrations, as detailed in Appendix A. The various contributions to the tuning accuracy for each of the adjustable laser and target parameters is shown in Figure 33 in terms of their variance normalized to the tuning budget listed in the last Column in Table I. Many of these terms are themselves rms sums of various contributors outlined in Section II and in Appendix A, and some of them have already been validated or updated by the results of the 2009 hohlraum energetics campaign. We see that we meet the tuning accuracy budget for all parameters.

The preferred tuning sequence follows closely the sequence of tuning techniques presented in Section II. The primary strategy is to first set early parameters in the laser pulse that are not affected by causality by choices later in the pulse. This also has the merit that truncated low environmental impact pulses can be used earlier in the life of the NIF laser. A proposed sequence is shown in Figure 34 as a matrix of rows of observables and columns of adjustable parameters. Green boxes on the principal diagonal designate the principal adjustable parameter set by a particular observable. Yellow boxes below the diagonal designate adjustable parameters set later that depend significantly on tuning performed earlier. Orange boxes above the diagonal designate adjustable parameters already set that can be affected significantly by tuning performed later. If we understood those cross-couplings perfectly, then we could just correct as we proceed. However, there is uncertainty in the magnitude of these cross-couplings that will require looping back as shown schematically in Figure 34. The chronological tuning sequence has been tailored to minimize the ratio of cross-couplings above versus below the diagonal. The three principal reasons for looping back are as follows: A change in total foot laser power to set the first shock velocity will affect the relative inner vs. outer cone drive flux and hence foot symmetry due to uncertainty in relative burnthrough of the inner and outer beams. A change in hohlraum length to zero  $P_4$  will affect  $P_2$ , will affect the total x-ray drive flux and hence the shock velocity and by the connection above, the foot symmetry. A change in initial mass to set residual mass will affect the shock timing and the implosion velocity. We also tabulate on Figure 34 the calculated cross-coupling sensitivities normalized to the tuning accuracy budget. For example,  $\Delta P_2 / \Delta P_4 = -1$  means that changing the hohlraum length to change  $P_4$  x% of its budgeted accuracy for  $P_4$  will

also change  $P_2$  by  $x\%$  of its budget. The fact that these cross-coupling terms are usually 1 or less is a reflection of the choice of target design and balancing of risk. In addition to these mainline shots, a set of contingency shots has been identified. These include: increasing ablator dopant content to eliminate the VISAR window blanking by hard x-rays; testing if laser-plasma backscattering of the  $30^\circ$  beams hitting the keyhole cone are responsible for a measured change in drive at the capsule by using a dedicated shot to orient the cone towards the  $30^\circ$  quad equipped with a backscatter station; switching to uniform ablator doping if mix complicates interpretation of the residual ablator mass; and using thinner symmetry capsules to tune out suspected  $P_2$  symmetry swings during the 4<sup>th</sup> rise or earlier. Finally, a set of shots at the full-scale ignition target if larger than 1.2 MJ are planned to check for scale-up extrapolation errors.

The chronological progress in increasing the mean ITF by tuning as schematically shown in Figure 3 has also been quantified. Moreover, a new figure-of-merit<sup>7</sup> that better characterizes the full ITF function with respect to the probability of ignition has been applied. The Margin over Uncertainty (M/U) is defined as the  $(\text{Mean ITF} - 1)/\sqrt{((1\sigma \text{ ITF})^2 + (\text{Rise in Prob. Ignition})^2)}$ . For example a final mean ITF of 2 with a  $1\sigma$  in ITF distribution = 0.7 and a 15 to 85% rise in ignition probability = 0.2 ITF as shown in Figure 3 translates to an  $M/U = 1/0.9 = 1.1$ . To plot the progression in M/U vs. shot number, we start with the initial  $1\sigma$  uncertainties in the tuning parameters listed in column 5 on Table I which relate back to the ITF and uncertainty in ITF through column 2. We then update the uncertainties using the formulae in Appendix A as we follow the tuning strategy for each parameter as shown in Fig. 32 in the sequence shown in Figure 34. Finally we include the impact of iterations, of checks of the surrogacy of shared

observables such as core symmetry, bangtime, mass remaining and peak implosion velocity using interleaved cryogenic layered implosions<sup>47</sup>, and of scale-up checks. The first successful shot of a particular tuning campaign will eliminate the offset error, leaving measurement errors, data scatter, extrapolation, cross-coupling, and systematic errors due to uncertainties in surrogacy and scale-up. Successive shots taken under nominally the same conditions will reduce data scatter. The second set of shots varying the adjustable parameter will reduce extrapolation errors. Iterations will reduce cross-coupling errors, and cryogenically layered shots and scale-up shots eliminate some systematic errors. We can thus calculate progression in Margin = ITF-1, uncertainty, M/U and probability of ignition versus shot number for various scenarios. The first 40 shots have been largely dedicated to the hohlraum energetics campaign setting the go-forward hohlraum design after having evaluated and optimized the laser-plasma coupling efficiency. 40-60 shots is then deemed necessary for capsule tuning, followed by 15-20 shots for checking tuning fidelity and performance of cryogenically-layered THD-filled capsules. Barring unexpected physics issues, this number of shots is predicted to reach an end-point ITF > 1.7, M/U > 0.85 and probability of ignition on any given shot > 85% as a necessary prelude to the first DT ignition experiment.

A further set of shots are planned before, or after the first ignition attempts if still required, to isolate particular capsule physics not addressed directly by the tuning campaigns, principally fuel preheat and ablator mix into the fuel or hot spot. In the realm of preheat raising fuel adiabat, the 2009 results for 280 eV, 1 MJ drives infer up to 2% hot electron fractional preheat<sup>135</sup> from the Au wall Bremsstrahlung, only a factor of three less than tolerable. In addition, a burst of suprahhot electrons above a certain laser

intensity threshold has been observed<sup>136</sup> during the initial laser-LEH window interaction on scaled OMEGA experiments, attributed to the two-plasmon decay instability<sup>137</sup>. The levels of hot electrons during the foot of the pulse is principally a surrogacy issue for shock timing in liquid D<sub>2</sub> that would not mimic the solid DT shell preheat expansion. Hence it seems prudent to attempt a more direct measure of the level of hot electron preheat reaching the capsule fuel, especially since the hot electron production mechanisms can be directional. This is being planned by absolutely calibrated, moderate spatial resolution (to discriminate capsule from hohlraum) 40-100 keV imaging of the capsule Bremsstrahlung through an LEH, both during the foot using the reemit capsule and during the peak using the symmetry capsule. A more advanced design for the future would measure the in-flight fuel adiabat (essentially  $1 + \frac{T_e}{T_i}$  the ratio of  $T_e$  to the Fermi energy) by x-ray spectrally resolved Thomson scattering<sup>138</sup>. For the latter, recent x-ray scattering experiments<sup>139</sup> at OMEGA have demonstrated the feasibility of diagnosing imploding capsule conditions using the Compton downshifted feature from a 9 keV Zn He-alpha resonance probe line. In the realm of hydroinstability, the bright spots of CH(Ge) dopant material observed jetting into the symmetry capsule hot spots and recognition of increased sensitivity of CH (vs Be) to surface roughness or isolated defects have spurred designs to measure the ablation front Rayleigh-Taylor growth by in-flight x-ray face-on or side-on radiography<sup>140</sup>. In addition, preliminary designs exist for assessing the in-flight density differential between ablator and fuel (and hence the Atwood number and susceptibility to ablator-fuel high-mode mix) using refraction-enhanced x-ray radiography<sup>141</sup>.

If a change in ablator material or hohlraum design is deemed necessary to either recover ignition margin from unfavorable physics or to optimize margin, then we would embark on a further capsule tuning campaign after having revalidated adequate hohlraum peak drive. The number of each type of tuning shot would be influenced by what we learned from the first campaign on reproducibility and level of surrogacy between the capsule tuning and cryogenically layered implosions.

#### **IV. SUMMARY**

A capsule performance optimization campaign has been presented with the goal of substantially increasing the probability of ignition on NIF. The campaign will experimentally correct for residual uncertainties in the implosion and hohlraum physics used in our radiation-hydrodynamic computational models before proceeding to ignition experiments. The sensitivity to laser and target tuning parameters extracted from detailed hydrodynamic simulations have been derived quantitatively using simple analytic models. The chosen tuning techniques have been shown experimentally and computationally to meet the required sensitivity and accuracy. The tuning campaign plans include checks of repeatability, iterations to overcome residual cross-couplings and contingency shots. Finally, a set of experiments has been outlined for isolating if needed capsule implosion physics issues.

#### **ACKNOWLEDGEMENTS**

This work was performed under the auspices of the U.S. Department of Energy by

## APPENDIX A: ERROR BREAKDOWN

The total  $1\sigma$  variability in either setting or getting the optimum value for any adjustable parameter for an ignition shot attempt is given by the following rms sum if we do not precompensate for known randomly distributed ignition target variability  $\sigma_{IgnTargetVar}$ :

$$\sigma_{Total}^2 = \sigma_{Tuning}^2 + \sigma_{LaserVar}^2 + \sigma_{IgnTargetVar}^2 + \sigma_{IgnTargetMetr}^2 \quad (A1)$$

where  $\sigma_{LaserVar}$  is the random rms variability in an ignition observable or parameter from the expected laser variability (e.g. power levels, cone balance) on any given ignition shot,  $\sigma_{IgnTargetVar}$  is the random rms variability in an ignition observable or parameter expected from known ignition target variations (e.g. capsule thickness, hohlraum length),  $\sigma_{IgnTargetMetr}$  is the random rms variability in an ignition observable or parameter expected from the residual ignition target metrology uncertainties (e.g. capsule thickness, dopant concentration), after precompensating for the known part of target variability,  $\sigma_{Tuning}$  is the  $1\sigma$  uncertainty in an ignition observable or parameter based on residual errors in the experimental tuning. If we do precompensate, the  $\sigma_{IgnTargetVar}$  term is removed.

The contribution discussed in this paper, the experimental tuning portion of the variability in setting ignition parameters, is itself the quadrature sum of the following:

$$\sigma_{Tuning}^2 = \sigma_{Random}^2 + \sigma_{Systematic}^2 + \sigma_{Sampling}^2 + \sigma_{Surrogacy}^2 + \sigma_{Scaleup}^2$$



(A2)

where  $\sigma_{Systematic}$  is the estimated  $1\sigma$  shot-to-shot repeatable errors in observables due to diagnostic and experimental uncertainties (e.g. calibration errors, LEH closure correction, cable compensation for Dante Tr),  $\sigma_{Sampling}$  is the estimated systematic  $1\sigma$  bias error due to limited FoV or sample size in time and space for observable (e.g. No  $23^\circ$  and  $44^\circ$  FABS, no symmetry tuning of 2<sup>nd</sup> and 3<sup>rd</sup> shock, wall vs capsule Tr sampling, the repeatable part of the azimuthal asymmetry),  $\sigma_{Surrogacy}$  is the estimated  $1\sigma$  shot-to-shot repeatable errors in the correction to an observable from known differences in hohlraum environment and/or surrogate capsule behavior (e.g. effect of patches and missing beams for re-emit),  $\sigma_{Scaleup}$  is the estimated  $1\sigma$  error in extrapolation correction to an observable as we scale-up in laser energy and target size (e.g. pop-up from a 1.3 MJ-scale where the performance is tuned to an  $\approx 10\%$  larger 1.7 MJ-scale).  $\sigma_{Random}$  is the estimated  $1\sigma$  shot-to-shot random variability in observables which breaks down further into:

$$\sigma_{Random}^2 = \frac{\frac{\sigma_{Msmt}^2}{\#Chan. \times View} + \sigma_{Statistical}^2 + \sigma_{LaserMetr}^2 + \sigma_{TargetMetr}^2}{\#Shots} \quad (A3)$$

where the first term  $\sigma_{Msmt}$  is the random rms variability in observable per channel expected from the experimental measurement statistical uncertainties (e.g. shot noise/signal for one image (i.e. one channel) on GXD strip) that can be averaged over a number of equivalent channels and/or views. Of the remaining terms,  $\sigma_{Statistical}$  is the random rms variability in observable per shot expected from having finite LoS (e.g. variability in  $P_2$  observed due to 3D random power imbalances),  $\sigma_{LaserMetr}$  is the random

rms variability in observable expected from the residual laser diagnostic uncertainties (e.g. power and cone balance) after normalizing each data point postshot for the known part of laser variability, and  $\sigma_{TargetMetr}$  is the random rms variability in observable expected from the residual tuning target metrology uncertainties (e.g. capsule thickness, hohlraum length), after normalizing each data point for the known part of the target variability.

## REFERENCES

- 
- <sup>1</sup> G.H. Miller, E.I. Moses and C.R. Wuest, Nucl. Fusion **44**, 228 (2004).
- <sup>2</sup> E.I. Moses, J. Phys.: Conf. Ser. **112**, 012003 (2008); J.D. Kilkenny, T.P. Bernat, B.A. Hammel, R.L. Kauffman, O.L. Landen, J.D. Lindl, B.J. Macgowan, J.A. Paisner and H.T. Powell, Laser and Part. Beams **17**, 159 (1999); Joseph D. Kilkenny, E. Michael Campbell, John D. Lindl, Grant B. Logan, Wayne R. Meier, L. John Perkins, Jeffrey A. Paisner, Michael H. Key, Howard T. Powell, Robert L. McCrory, and Wolf Seka, Phil. Trans. R. Soc. of Lond. A **357**, 533 (1999).
- <sup>3</sup> J.D. Lindl, Phys Plasmas **2**, 3933 (1995); J. D. Lindl, P. Amendt, R. L. Berger, S. G. Glendinning, S. H. Glenzer, S.W. Haan, R. L. Kauffman, O. L. Landen, and L. J. Suter, Phys. Plasmas **11**, 339 (2004).
- <sup>4</sup> J. L. Atherton, J. Phys.: Conf. Ser. **112**, 032063 (2008).
- <sup>5</sup> C. A. Haynam, P. J. Wegner, J. M. Auerbach, M. W. Bowers, S. N. Dixit, G. V. Erbert, G. M. Heestand, M. A. Henesian, M. R. Hermann, K. S. Jancaitis, K. R. Manes, C. D. Marshall, N. C. Mehta, J. Menapace, E. Moses, J. R. Murray, M. C. Nostrand, C. D. Orth, R. Patterson, R. A. Sacks, M. J. Shaw, M. Spaeth, S. B. Sutton, W. H. Williams, C. C. Widmayer, R. K. White, S. T. Yang, and B. M. Van Wonterghem, Appl. Optics **46**, 3276 (2007).
- <sup>6</sup> S. H. Glenzer, B. J. MacGowan, P. Michel, N. B. Meezan, L. J. Suter, S. N. Dixit, J. L. Kline, G. A. Kyrala, D. A. Callahan, E. L. Dewald, L. Divol, E. Dzenitis, M. J. Edwards, A. V. Hamza, C. A. Haynam, D. E. Hinkel, D. H. Kalantar, J. D. Kilkenny, O. L. Landen, J. D. Lindl, S. LePape, J. D. Moody, A. Nikroo, T. Parham, M. B. Schneider, R. P. J. Town, P. Wegner, K. Widmann, P. Whitman, B. K. F. Young, B. Van Wonterghem, J. E.

---

Atherton, E. I. Moses, *Science* **327** (2010) 1228; N. B. Meezan, L. J. Atherton, D. A. Callahan, E. L. Dewald, S. Dixit, E. G. Dzenitis, M. J. Edwards, C. A. Haynam, D. E. Hinkel, O. S. Jones, O. Landen, R.A. London, P. A. Michel, J. D. Moody, J. L. Milovich, M B. Schneider, C. A. Thomas, R. P. J. Town, A. L. Warrick, S. V. Weber, K. Widmann, S. H. Glenzer, L. J. Suter, B. J. MacGowan, J. L. Kline, G. A. Kyrala, and A. Nikroo, *Phys. Plasmas* **18**, (2010) 056304.

<sup>7</sup> S. W. Haan, L.J. Atherton, D.A. Callahan, D.S. Clark, R. Cook, M.J. Edwards, B. A. Hammel, A. Hamza, D.E. Hinkel, D. D. Ho, O.S. Jones, O. L. Landen, J. D. Lindl, B.J. MacGowan, M. M. Marinak, E.I. Moses, D. H. Munro, S. M. Pollaine, J. D. Salmonson, B.K. Spears, P.T. Springer, L. J. Suter, R.P. Town, and S.V. Weber, this *Phys. Plasmas* proceedings.

<sup>8</sup> Daniel S. Clark, Steven W. Haan, Bruce A. Hammel, Jay D. Salmonson, Debra A. Callahan, and Richard P. J. Town, *Phys. Plasmas* **17**, 052703 (2010).

<sup>9</sup> S. W. Haan, M. C. Herrmann, T. R. Dittrich, A. J. Fetterman, M. M. Marinak, D. H. Munro, S. M. Pollaine, J. D. Salmonson, G. L. Strobel, and L. J. Suter, *Phys. Plasmas* **12**, 056316 (2005).

<sup>10</sup> T. C. Sangster, R. Betti, R. S. Craxton, J. A. Delettrez, D. H. Edgell, L. M. Elasky, V. Yu. Glebov, V. N. Goncharov, D. R. Harding, D. Jacobs-Perkins, R. Janezic, R. L. Keck, J. P. Knauer, S. J. Loucks, L. D. Lund, F. J. Marshall, R. L. McCrory, P. W. McKenty, D. D. Meyerhofer, P. B. Radha, S. P. Regan, W. Seka, W. T. Shmayda, S. Skupsky, V. A. Smalyuk, J. M. Soures, C. Stoeckl, B. Yaakobi, J. A. Frenje, C. K. Li, R. D. Petrasso, F. H. Séguin, J. D. Moody, J. A. Atherton, B. D. MacGowan, J. D. Kilkenny, T. P. Bernat, and D. S. Montgomery *Phys. Plasmas* **14**, 058101 (2007).

- 
- <sup>11</sup> Douglas C. Wilson, Paul A. Bradley, Nelson M. Hoffman, Fritz J. Swenson, David P. Smitherman, Robert E. Chrien, Robert W. Margevicius, D. J. Thoma, Larry R. Foreman, James K. Hoffer, S. Robert Goldman, Stephen E. Caldwell, Thomas R. Dittrich, Steven W. Haan, Michael M. Marinak, Stephen M. Pollaine, and Jorge J. Sanchez, *Phys. Plasmas* **5**, 1953 (1998).
- <sup>12</sup> T. R. Dittrich, S. W. Haan, M. M. Marinak, S. M. Pollaine, D. E. Hinkel, D. H. Munro, C. P. Verdon, G. L. Strobel, R. McEachern, R. C. Cook, C. C. Roberts, D. C. Wilson, P. A. Bradley, L. R. Foreman, and W. S. Varnum, *Phys. Plasmas* **6**, 2164 (1999).
- <sup>13</sup> D. A. Callahan, D. E. Hinkel, R. L. Berger, L. Divol, S. N. Dixit, M. J. Edwards, S. W. Haan, O. S. Jones, J. D. Lindl, N. B. Meezan, P. A. Michel, S. M. Pollaine, L. J. Suter, R. P. J. Town and P.A. Bradley, *J. Phys.: Conf. Ser.* **112**, 022021 (2008).
- <sup>14</sup> A. Nikroo, K. C. Chen, M. L. Hoppe, H. Huang, J. R. Wall, H. Xu, M. W. McElfresh, C. S. Alford, R. C. Cook, J. C. Cooley, R. Fields, R. Hackenberg, R. P. Doerner and M. Baldwin, *Physics of Plasmas* **13**, 056302 (2006).
- <sup>15</sup> K. C. Chen, R. C. Cook, H. Huang, S. A. Letts, and A. Nikroo, *Fusion Sci. and Technol.* **49**, 750 (2006).
- <sup>16</sup> J. Biener, P. Mirkarimi, J. Tringe, S. Baker, Y. Wang, S. Kucheyev, N. Teslich, K. Wu, A. Hamza, C. Wild, E. Woerner, P. Koidl, K. Bruehlne, and H. Fecht, *Fusion Sci. and Technol.* **49**, 737 (2006).
- <sup>17</sup> M. M. Marinak, S. W. Haan, T. R. Dittrich, R. E. Tipton, and G. B. Zimmerman, *Phys. Plasmas* **5**, 1125 (1998).

- 
- <sup>18</sup> S. W. Haan, M. C. Herrmann, P. A. Amendt, D. A. Callahan, T. R. Dittrich, M. J. Edwards, O. S. Jones, M. M. Marinak, D. H. Munro, S. M. Pollaine, J. D. Salmonson, B. K. Spears, and L. J. Suter, *Fusion Sci. Technol.* **49**, 553 (2006).
- <sup>19</sup> S. W. Haan, P. A. Amendt, D. A. Callahan, T. R. Dittrich, M. J. Edwards, B. A. Hammel, D. D. Ho, O. S. Jones, J. D. Lindl, M. M. Marinak, D. H. Munro, S. M. Pollaine, J. D. Salmonson, B. K. Spears, and L. J. Suter, *Fusion Sci. Technol.* **51**, 509 (2007).
- <sup>20</sup> S.W. Haan, M.C. Herrmann J.D. Salmonson, P.A. Amendt, D.A. Callahan, T.R. Dittrich, M.J. Edwards, O.S. Jones, M.M. Marinak, D.H. Munro, S.M. Pollaine, B.K. Spears, and L.J. Suter., *Eur. Phys. J. D* **44**, 249 (2007).
- <sup>21</sup> Daniel S. Clark, Steven W. Haan, and Jay D. Salmonson, *Phys. Plasmas* **15**, 056305 (2008).
- <sup>22</sup> S. W. Haan, D.A. Callahan, M.J. Edwards, B. A. Hammel, D. D. Ho, O.S. Jones, J. D. Lindl, B. J. MacGowan, M. M. Marinak, D. H. Munro, S. M. Pollaine, J. D. Salmonson, B. K. Spears, and L. J. Suter, *Fusion Sci. Technol.* **55**, 227 (2009).
- <sup>23</sup> N. B. Meezan, S. H. Glenzer, and L. J. Suter, *J. Phys.: Conf. Ser.* **112**, 022022 (2008).
- <sup>24</sup> D. H. Froula, D. Bower, M. Chrisp, S. Grace, J. H. Kamperschroer, T. M. Kelleher, R. K. Kirkwood, B. MacGowan, T. McCarville, N. Sewall, F. Y. Shimamoto, S. J. Shiromizu, B. Young, and S. H. Glenzer, *Rev. Sci. Instrum.* **75**, 4168 (2004).
- <sup>25</sup> A. J. Mackinnon, T. McCarville, K. Piston, C. Niemann, G. Jones, I. Reinbachs, R. Costa, J. Celeste, G. Holtmeier, R. Griffith, R. Kirkwood, B. MacGowan, S. H. Glenzer, and M. R. Latta, *Rev. Sci. Instrum.* **75**, 4183 (2004).

- 
- <sup>26</sup> J. W. McDonald, R. L. Kauffman, J. R. Celeste, M. A. Rhodes, F. D. Lee, L. J. Suter, A. P. Lee, J. M. Foster, and G. Slark, *Rev. Sci. Instrum.* **75**, 3753 (2004).
- <sup>27</sup> E. L. Dewald, K. M. Campbell, R. E. Turner, J. P. Holder, O. L. Landen, S. H. Glenzer, R. L. Kauffman, L. J. Suter, M. Landon, M. Rhodes, and D. Lee, *Rev. Sci. Instrum.* **75**, 3759 (2004).
- <sup>28</sup> John A. Oertel, Robert Aragonese, Tom Archuleta, Cris Barnes, Larry Casper, Valerie Fatherley, Todd Heinrichs, Robert King, Doug Landers, Frank Lopez, Phillip Sanchez, George Sandoval, Lou Schrank, Peter Walsh, Perry Bell, Matt Brown, Robert Costa, Joe Holder, Sam Montelongo, and Neal Pederson, *Rev. Sci. Instrum.* **77**, 10E308 (2006).
- <sup>29</sup> E. L. Dewald, L. J. Suter, O. L. Landen, J. P. Holder, J. Schein, F. D. Lee, K. M. Campbell, F. A. Weber, D. G. Pellinen, M. B. Schneider, J. R. Celeste, J.W. McDonald, J. M. Foster, C. Niemann, A. J. Mackinnon, S. H. Glenzer, B. K. Young, C. A. Haynam, M. J. Shaw, R. E. Turner, D. Froula, R. L. Kauffman, B. R. Thomas, L. J. Atherton, R. E. Bonanno, S. N. Dixit, D. C. Eder, G. Holtmeier, D. H. Kalantar, A. E. Koniges, B. J. MacGowan, K. R. Manes, D. H. Munro, J. R. Murray, T. G. Parham, K. Piston, B. M. Van Wonerghem, R. J. Wallace, P. J. Wegner, P. K. Whitman, B. A. Hammel, and E. I. Moses, *Phys. Rev. Lett.* **95**, 215004 (2005); E. L. Dewald, O. L. Landen, L. J. Suter, J. Schein, J. Holder, K. Campbell, S. H. Glenzer, J. W. McDonald, C. Niemann, A. J. Mackinnon, M. S. Schneider, C. Haynam, D. Hinkel, and B. A. Hammel, *Phys. Plasmas* **13**, 056315 (2006).
- <sup>30</sup> O.L. Landen, S.H. Glenzer, D.H. Froula, E.L. Dewald, L.J. Suter, M.B. Schneider, D.E. Hinkel, J.C. Fernandez, J.L. Kline, S.R. Goldman, *et. al.*, *Eur. Phys. J. D* **44**, 273-281 (2007).

- 
- <sup>31</sup> E.M. Campbell, J.T. Hunt, E.S. Bliss, D.R. Speck, and R.P. Drake, Rev. Sci. Instrum. **57**, 2101 (1986).
- <sup>32</sup> J. M. Soures, R. L. McCrory, C. P. Verdon, A. Babushkin, R. E. Bahr, T. R. Boehly, R. Boni, D. K. Bradley, D. L. Brown, R. S. Craxton, J. A. Delettrez, W. R. Donaldson, R. Epstein, P. A. Jaanimagi, S. D. Jacobs, K. Kearney, R. L. Keck, J. H. Kelly, T. J. Kessler, R. L. Kremens, J. P. Knauer, S. A. Kumpan, S. A. Letzring, D. J. Lonobile, S. J. Loucks, L. D. Lund, F. J. Marshall, P. W. McKenty, D. D. Meyerhofer, S. F. B. Morse, A. Okishev, S. Papernov, G. Pien, W. Seka, R. Short, M. J. Shoup III, M. Skeldon, S. Skupsky, A. W. Schmid, D. J. Smith, S. Swales, M. Wittman, and B. Yaakobi, Phys. Plasmas **3**, 2108 (1996); T.R. Boehly, D.L. Brown, R.S. Craxton, R.L. Keck, J.P. Knauer, J.H. Kelly, T.J. Kessler, S.A. Kumpan, S.J. Bucks, S.A. Letzring, F.J. Marshall, R.L. McCrory, S.F.B. Morse, W. Seka, J.M. Soves, and C.P. Verdon, Opt. Comm. **133**, 495 (1997).
- <sup>33</sup> E. Dattolo, L. Suter, M.C. Monteil, J.P. Jadaud, N. Dague, S. Glenzer, R. Turner, D. Juraszek, B. Lasinski, C. Decker, O. Landen and B. MacGowan, Phys. Plasmas **8**, 260 (2001).
- <sup>34</sup> J.L. Bourgade, B. Villette, P. Stemmler, G. Oudot, G. Pien, O. Landen, C. Sorce, K. Widmann, and V. Tran, submitted to Rev. Sci. Instrum. (2010).
- <sup>35</sup> Didier Besnard, J. Phys.: Conf. Ser. **112**, 012004 (2008).
- <sup>36</sup> J. L. Bourgade, B. Villette, J. L. Bocher, J. Y. Boutin, S. Chiche, N. Dague, D. Gontier, J. P. Jadaud, B. Savale, R. Wrobel, and R. Turner, Rev. Sci. Instrum. **72**, 1173 (2001).



---

<sup>37</sup> J. L. Kline, K. Widmann, P. Torres, A. Warrick, C.A. Thomas, L.J. Suter, O.L.

Landen, D. Callahan, N.B. Meezan, R.E. Olson, and S.H. Glenzer, to be published in Rev. Sci. Instrum. (2010).

<sup>38</sup> J. L. Kline, S. H. Glenzer, R. E. Olson, K. Widmann, D. A. Callahan, S. N. Dixit, C. A. Thomas, D. E. Hinkel, E. A. Williams, A. Moore, J. Celeste, E. Dewald, W. W. Hsing, A. Warrick, J. Atherton, S. Azevedo, R. Beeler, R. Berger, A. Condor, L. Divol, C. A. Haynam, D. H. Kalantar, R. Kauffman, G. A. Kyrala, J. Kilkenny, J. Liebman, S. LePape, D. Larson, N. B. Meezan, P. Michel, J. Moody, M. D. Rosen, M. B. Schneider, H. Scott, B. Van Wonterghem, R. J. Wallace, B. K. Young, O. L. Landen, B. J. MacGowan, and L. J. Suter, submitted to Phys. Rev. Lett. (2010).

<sup>39</sup> Juan C. Fernández, S. R. Goldman, J. L. Kline, E. S. Dodd, C. Gautier, G. P. Grim, B. M. Hegelich, D. S. Montgomery, N. E. Lanier, H. Rose, D. W. Schmidt, J. B. Workman, D. G. Braun, E. L. Dewald, O. L. Landen, K. M. Campbell, J. P. Holder, A. J. MacKinnon, C. Niemann, J. Schein, B. K. Young, J. R. Celeste, S. N. Dixit, D. C. Eder, S. H. Glenzer, C. A. Haynam, D. Hinkel, D. Kalantar, J. Kamperschroer, R. L. Kauffman, R. Kirkwood, A. E. Koniges, F. D. Lee, B. J. MacGowan, K. R. Manes, J. W. McDonald, M. B. Schneider, M. J. Shaw, L. J. Suter, R. J. Wallace, F. A. Weber, and J. L. Kaae, Phys. Plasmas **13**, 056319 (2006).

<sup>40</sup> S.H. Glenzer, P. Arnold, G. Bardsley, R.L. Berger, G. Bonanno, T. Borger, M. Bowers, R. Bryant, S. Buckman, S.C. Burkhart, *et. al.*, Nuclear Fusion **44**, S185 (2004); S. H. Glenzer, D. H. Froula, L. Divol, M. Dorr, R. L. Berger, S. Dixit, B. A. Hammel, C. Haynam, J. A. Hittinger, J. P. Holder, O. S. Jones, D. H. Kalantar, O. L. Landen, A. B. Langdon, S. Langer, B. J. MacGowan, A. J. Mackinnon, N. Meezan, E. I. Moses, C.

---

Niemann, C. H. Still, L. J. Suter, R. J. Wallace, E. A. Williams and B. K. F. Young, *Nature Physics* **3**, 709 (2007).

<sup>41</sup> S.N. Dixit, M.D. Feit, M.D. Perry, and H.T. Powell, *Opt. Lett.* **21**, 1715 (1996).

<sup>42</sup> S.N. Dixit, D. Munro, J.R. Murray, M. Nostrand, P.J. Wegner, D. Froula, C.A. Haynam and B.J. MacGowan, *J. de Phys IV* **133**, 717 (2006).

<sup>43</sup> O. L. Landen, T. R. Boehly, D. K. Bradley, D. G. Braun, D. A. Callahan, P. M. Celliers, G. W. Collins, E. L. Dewald, L. Divol, S. H. Glenzer, A. Hamza, D. G. Hicks, N. Hoffman, N. Izumi, O. S. Jones, R. K. Kirkwood, G. A. Kyrala, P. Michel, J. Milovich, D. H. Munro, A. Nikroo, R. E. Olson, H. F. Robey, B. K. Spears, C. A. Thomas, S. V. Weber, D. C. Wilson, M. M. Marinak, L. J. Suter, B. A. Hammel, D. D. Meyerhofer, J. Atherton, J. Edwards, S. W. Haan, J. D. Lindl, B. J. MacGowan, and E. I. Moses *Phys. Plasmas* **17**, 05631 (2010).

<sup>44</sup> G.B. Zimmerman and W.L. Kruer, *Comments Plasma Phys.* **2**, 51 (1975).

<sup>45</sup> M. M. Marinak, G. D. Kerbel, N. A. Gentile, O. Jones, D. Munro, S. Pollaine, T. R. Dittrich, and S. W. Haan, *Phys. Plasmas* **8**, 2275 (2001).

<sup>46</sup> T. C. Sangster, R. L. McCrory, V. N. Goncharov, D. R. Harding, S. J. Loucks, P. W. McKenty, D. D. Meyerhofer, S. Skupsky, B. Yaakobi, B. J. MacGowan, L. J. Atherton, B. A. Hammel, J. D. Lindl, E. I. Moses, J. L. Porter, M. E. Cuneo, M. K. Matzen, C. W. Barnes, J. C. Fernandez, D. C. Wilson, J. D. Kilkenny, T. P. Bernat, A. Nikroo, B. G. Logan, S. Yu, R. D. Petrasso, J. D. Sethian, and S. Obenschain, *Nucl. Fusion* **47**, S686 (2007).

<sup>47</sup> J. Edwards, et. al., this *Phys. Plasmas* proceedings.

- 
- <sup>48</sup> L.J. Suter, A.A. Hauer, L.V. Powers, D.B. Ress, N. Delamater, W.W. Hsing, O.L. Landen, A. R. Thiessen and R.E. Turner, Phys. Rev. Lett. **73**, 2328 (1994); S. H. Glenzer, L. J. Suter, R. E. Turner, B. J. MacGowan, K. G. Estabrook, M. A. Blain, S. N. Dixit, B. A. Hammel, R. L. Kauffman, R. K. Kirkwood, O. L. Landen, M.-C. Monteil, J. D. Moody, T. J. Orzechowski, D. M. Pennington, G. F. Stone, and T. L. Weiland, Phys. Rev. Lett., **80**, 2845 (1998).
- <sup>49</sup> D. K. Bradley, D. G. Braun, S. G. Glendinning, M. J. Edwards, J. L. Milovich, C. M. Sorce, G. W. Collins, S. W. Haan, R. H. Page, R. J. Wallace, and J. L. Kaae, Phys. Plasmas **14**, 056313 (2007).
- <sup>50</sup> O. L. Landen, D. K. Bradley, D. G. Braun, V. A. Smalyuk, D. G. Hicks, P. M. Celliers, S. Prisbrey, R. Page, T. R. Boehly, S. W. Haan, D. H. Munro, R. G. Wallace, A. Nikroo, A. Hamza, J. Biener, C. Wild, E. Woerner, R. E. Olson, G. A. Rochau, M. Knudson, D. C. Wilson, H. F. Robey, G. W. Collins, D. Ho, J. Edwards, M. M. Marinak, B. A. Hammel, D. D. Meyerhofer and B. J. MacGowan, J. Phys.: Conf. Ser. **112** 022004 (2008).
- <sup>51</sup> N.D. Delamater, E.L. Lindman, G.R. Magelssen, B.H. Failor, T.J. Murphy, A.A. Hauer, P. Gobby, J.B. Moore, V. Gomez, K. Gifford, R.L. Kauffman, O.L. Landen, B.A. Hammel, G. Glendinning, L.V. Powers, L.J. Suter, S. Dixit, R.R. Peterson, and A.L. Richard, Phys. Plasmas **7**, 1609 (2000).
- <sup>52</sup> S P Regan, T C Sangster, D D Meyerhofer, W Seka, R Epstein, S J Loucks, R L McCrory, C Stoeckl, V Y Glebov, O S Jones, D A Callahan, P A Amendt, N B Meezan, L J Suter, M D Rosen, O L Landen, E L Dewald, S H Glenzer, C Sorce, S Dixit, R E Turner and B J MacGowan, J. Phys.: Conf. Ser. **112**, 022077 (2008).

- 
- <sup>53</sup> M. D. Knudson, D. L. Hanson, J. E. Bailey, C. A. Hall, J. R. Asay, and W. W. Anderson, Phys. Rev. Lett. **87**, 225501 (2001); D. G. Hicks, T. R. Boehly, P. M. Celliers, J. H. Eggert, S. J. Moon, D. D. Meyerhofer, and G. W. Collins, Phys Rev. B **79**, 014112 (2009).
- <sup>54</sup> F. J. Rogers, Phys. Plasmas **7**, 51 (2000).
- <sup>55</sup> K. Eidmann, I.B. Foldes, Th. Lower, J. Massen, R. Sigel, G.D. Tsakiris, S. Witkowski, H. Nishimura, Y. Kato, T. Endo, H. Shiraga, M. Takagi, and S. Nakai, Phys. Rev. E **52**, 6703 (1995); I.B. Foldes, K. Eidmann, Th. Lower, J. Massen, R. Sigel, G.D. Tsakiris, S. Witkowski, H. Nishimura, T. Endo, H. Shiraga, M. Takagi, Y. Kato, and S. Nakai, Phys. Rev E **50**, R690 (1994).
- <sup>56</sup> M.D. Rosen, Phys. Plasmas **5**, 1803 (1996).
- <sup>57</sup> Y.T. Lee and R.M. More, Plasma Phys. Controlled Fusion **27**, 1273 (1984).
- <sup>58</sup> P.A. Sterne, S.B. Hansen, B.G. Wilson, and W.A. Isaacs, High Energy Density Physics **3**, 278 (2007); B. Wilson, V. Sonnad, P. Sterne, W. Isaacs, J. Quant. Spectrosc. Radiat. Transfer **99**, 658 (2006).
- <sup>59</sup> R. E. Olson, R. J. Leeper, S. C. Dropinski, L. P. Mix, G. A. Rochau, S. H. Glenzer, O. S. Jones, L. J. Suter, J. L. Kaae, C. H. Shearer, and J. N. Smith, Rev. Sci. Instrum. **74**, 2186 (2003).
- <sup>60</sup> E. L. Dewald, M. Rosen, S. H. Glenzer, L. J. Suter, F. Girard, J. P. Jadaud, J. Schein, C. Constantin, F. Wagon, G. Huser, P. Neumayer, and O. L. Landen, Phys. Plasmas **15**, 072706 (2008); F. Ze, S. H. Langer, R. L. Kauffman, J. D. Kilkenny, O. Landen, D. Ress, M. D. Rosen, L. J. Suter, R. J. Wallace, and J. D. Wiedwald, Phys. Plasmas **4**, 778 (1997).

- 
- <sup>61</sup> O.S. Jones, S.H. Glenzer, L.J. Suter, R.E. Turner, K.M. Campbell, E.L. Dewald, B.A. Hammel, R.L. Kauffman, O.L. Landen, M.D. Rosen, R.J. Wallace, and F.A. Weber, *Phys. Rev. Lett.* **93**, 065002 (2004).
- <sup>62</sup> Jochen Schein, Ogden Jones, Mordecai Rosen, Eduard Dewald, Siegfried Glenzer, Janelle Gunther, Bruce Hammel, Otto Landen, Laurence Suter, and Russell Wallace, *Phys. Rev. Lett.* **98**, 175003 (2007); O. S. Jones, J. Schein, M. D. Rosen, L. J. Suter, R. J. Wallace, E. L. Dewald, S. H. Glenzer, K. M. Campbell, J. Gunther, B. A. Hammel, O. L. Landen, C. M. Sorce, R. E. Olson, G. A. Rochau, H. L. Wilkens, J. L. Kaae, J. D. Kilkenny, A. Nikroo, and S. P. Regan, *Phys. Plasmas* **14**, 056311 (2007).
- <sup>63</sup> N. B. Meezan, R. L. Berger, L. Divol, D. H. Froula, D. E. Hinkel, O. S. Jones, R. A. London, J. D. Moody, M. M. Marinak, C. Niemann, P. B. Neumayer, S. T. Prisbrey, J. S. Ross, E. A. Williams, S. H. Glenzer, and L. J. Suter, *Phys. Plasmas* **14**, 056304 (2007).
- <sup>64</sup> H. F. Robey, T. S. Perry, H.-S. Park, P. Amendt, C. M. Sorce, S. M. Compton, K. M. Campbell, and J. P. Knauer, *Phys. Plasmas* **12**, 072701 (2005).
- <sup>65</sup> R. E. Olson, R. J. Leeper, A. Nobile, J. A. Oertel, G. A. Chandler, K. Cochrane, S. C. Dropinski, S. Evans, S. W. Haan, J. L. Kaae, J. P. Knauer, K. Lash, L. P. Mix, A. Nikroo, G. A. Rochau, G. Rivera, C. Russell, D. Schroen, R. J. Sebring, D. L. Tanner, R. E. Turner, and R. J. Wallace, *Phys. Plasmas* **11**, 2778 (2004).
- <sup>66</sup> R. E. Olson, R. J. Leeper, A. Nobile, and J. A. Oertel, *Phys. Rev. Lett.* **91**, 235002 (2003).
- <sup>67</sup> B.A. Hammel, S.W. Haan, D.S. Clark, M.J. Edwards, S.H. Langer, M.M. Marinak, M.V. Patel, J.D. Salmonson, and H.A. Scott, *High Energy Density Physics* **6**, xxx (2010).

- 
- <sup>68</sup> B. A. Hammel, M. J. Edwards, S. W. Haan, M. M. Marinak, M. Patel, H. Robey and J. Salmonson, J. Phys.: Conf. Ser. **112**, 022007 (2008).
- <sup>69</sup> N. D. Delamater, G. R. Magelssen, and A. A. Hauer, Phys. Rev. E **53**, 5240 (1996); G. R. Magelssen, N. D. Delamater, E. L. Lindman, and A. A. Hauer, Phys. Rev. E **57**, 4663 (1998).
- <sup>70</sup> T. R. Boehly, D. Munro, P. M. Celliers, R. E. Olson, D. G. Hicks, V. N. Goncharov, G. W. Collins, H. F. Robey, S. X. Hu, J. A. Morozas, T. C. Sangster, O. L. Landen, and D. D. Meyerhofer, Phys. Plasmas **16**, 056302 (2009).
- <sup>71</sup> A. A. Hauer, L. Suter, N. Delamater, D. Ress, L. Powers, G. Magelssen, D. Harris, O. Landen, E. Lindmann, W. Hsing, D. Wilson, and P. Amendt, Phys. Plasmas **2**, 672 (1995).
- <sup>72</sup> D. Hicks, Bull. Am. Phys. Soc. **53**, 2 (2008); D. G. Hicks, B. K. Spears, D. G. Braun, R. E. Olson, C. M. Sorce, P. M. Celliers, G. W. Collins, and O. L. Landen, to be published in Rev. Sci. Instrum. (2010); D. G. Hicks, B. K. Spears, D. G. Braun, P. M. Celliers, G. W. Collins, O. L. Landen, and R.E. Olson, submitted to Phys. Plasmas (2010).
- <sup>73</sup> B Spears, D Hicks, C Velsko, M Stoyer, H Robey, D Munro, S Haan, O Landen, A Nikroo and H Huang, J. Phys.: Conf. Ser. **112**, 022003 (2008).
- <sup>74</sup> N. M. Hoffman, D. C. Wilson and G. A. Kyrala, Rev. Sci. Instrum. **77**, 10E705 (2006); N. M. Hoffman, D. C. Wilson, M. J. Edwards, D. H. Kalantar, G. A. Kyrala, S. R. Goldman, S. V. Weber, N. Izumi, D. A. Callahan, N. Meezan, N. D. Delamater, I. L. Tregillis, M. J. Schmitt, P. A. Bradley, A. Seifter, O. S. Jones, J. L. Milovich and C. A. Thomas, J. Phys.: Conf. Ser., **112**, 022075 (2008).

- 
- <sup>75</sup> S.M. Pollaine, D.K. Bradley, O.L. Landen, R.J. Wallace, O.S. Jones, P.A. Amendt, L.J. Suter, and R.E. Turner, *Phys. Plasmas* **8**, 2357 (2001); R. K. Kirkwood, J. Milovich, D. K. Bradley, M. Schmitt, S. R. Goldman, D. H. Kalantar, D. Meeker, O. S. Jones, S. M. Pollaine, P. A. Amendt, E. Dewald, J. Edwards, O. L. Landen, and A. Nikroo, *Phys. Plasmas* **16**, 012702 (2009).
- <sup>76</sup> N. Delamater, P. Bradley, G. Magelssen, and D. Wilson, *Rev. Sci. Instrum.* **77**, 10E302 (2006).
- <sup>77</sup> F. Ze, R. L. Kauffman, J. D. Kilkenny, J. Wiedwald, P. M. Bell, R. Hanks, J. Stewart, D. Dean, J. Bower, and R. Wallace, *Rev. Sci. Instrum.* **63**, 5124 (1992).
- <sup>78</sup> D H. Cohen, O.L. Landen, and J .J. MacFarlane, *Phys. Plasmas* **12**, 122703 (2005).
- <sup>79</sup> K. M. Campbell, F. A. Weber, E. L. Dewald, S. H. Glenzer, O. L. Landen, R. E. Turner, and P. A. Waide, *Rev. Sci. Instrum.* **75**, 3768 (2004).
- <sup>80</sup> F. Girard, L. Suter, O. Landen, D. Munro, S. Regan and J. Kline, *Rev. Sci. Instrum.* **80**, 063104 (2009).
- <sup>81</sup> D C Eder, A E Koniges, O L Landen, N D Masters, A C Fisher, O S Jones, T I Suratwala, and L J Suter, *J. Phys.: Conf. Ser.* **112**, 032023 (2008)
- <sup>82</sup> A. L. Meadowcroft, C. D. Bentley, and E. N. Stott, *Rev. Sci. Instrum.* **79**, 113102 (2008).
- <sup>83</sup> E.L. Dewald, J. Milovich, J. Edwards, C. Thomas, R. Kirkwood, D. Meeker, O. Jones, N. Izumi, and O.L. Landen, *Rev. Sci. Instrum.* **79**, 10E903 (2008).
- <sup>84</sup> Eduard Dewald, Jose Milovich, Cliff Thomas, Steven Glenn, John Kline, Rahul Prasad, and O.L. Landen, *Bull. Am. Phys. Soc.* **54**, 28 (2009); E.L. Dewald, J. Milovich, C.

---

Thomas, J. Kline, J. Edwards, C. Sorce, S. Glenn, and O.L. Landen, submitted to Phys. Plasmas (2010).

<sup>85</sup> M.A. Knudson, Bull. Am. Phys. Soc. **51**, 340 (2006).

<sup>86</sup> David H. Munro, Peter M. Celliers, Gilbert W. Collins, David M. Gold, Luiz B. Da Silva, Steven W. Haan, Robert C. Cauble, Bruce A. Hammel, and Warren W. Hsing, Phys. Plasmas **8**, 2245 (2001).

<sup>87</sup> T. R. Boehly, D. G. Hicks, P. M. Celliers, T. J. B. Collins, R. Earley, J. H. Eggert, D. Jacobs-Perkins, S. J. Moon, E. Vianello, D. D. Meyerhofer, and G. W. Collins, Phys. Plasmas **11**, L49 (2004).

<sup>88</sup> P. M. Celliers, D. K. Bradley, G. W. Collins, D. G. Hicks, T. R. Boehly and W. J. Armstrong, Rev. Sci. Instrum. **75**, 4916 (2004); Robert M. Malone, John R. Bower, Gene A. Capelle, John R. Celeste, Peter M. Celliers, Brent C. Frogget, Robert L. Guyton, Morris I. Kaufman, Gregory A. Lare, Tony L. Lee, Brian J. MacGowan, Samuel Montelongo, Edmund W. Ng, Thayne L. Thomas, Jr., Thomas W. Tunnell, Phillip W. Watts, Proc. of SPIE **5523**, 148 (2004).

<sup>89</sup> H F Robey, D H Munro, B K Spears, M M Marinak, O S Jones, M V Patel, S W Haan, J D Salmonson, O L Landen, T R Boehly and A Nikroo, J. Phys.: Conf. Ser. **112**, 022078 (2008).

<sup>90</sup> P. A. Jaanimagi, R. Boni, D. Butler, S. Ghosh, W. R. Donaldson, and R. L. Keck, Proc. SPIE **5580**, 408 (2005).

<sup>91</sup> P. A. Jaanimagi, L. DaSilva, G. G. Gregory, C. Hestdalen, C. D. Kiikka, R. Kotmel, and M. C. Richardson, Rev. Sci. Instrum. **57**, 2189 (1986).



- 
- <sup>92</sup> W. Theobald, J. E. Miller, T. R. Boehly, E. Vianello, D. D. Meyerhofer, T. C. Sangster, J. Eggert, and P. M. Celliers, *Phys. Plasmas* **13**, 122702 (2006).
- <sup>93</sup> R. L. Kauffman, L. J. Suter, C. B. Darrow, J. D. Kilkenny, H. N. Kornblum, D. S. Montgomery, D. W. Phillion, M. D. Rosen, A. R. Theissen, R. J. Wallace, and F. Ze, *Phys. Rev. Lett.* **73**, 2320 (1994).
- <sup>94</sup> H. F. Robey, T. R. Boehly, R. E. Olson, A. Nikroo, P. Celliers, O. L. Landen, and D. D. Meyerhofer, *Phys. Plasmas* **17**, 012703 (2009).
- <sup>95</sup> R. J. Trainor, J. W. Shaner, J. M. Auerbach, and N. C. Holmes, *Phys. Rev. Lett.* **42**, 1154 (1979).
- <sup>96</sup> M. D. Landon, J. A. Koch, S. S. Alvarez, P. M. Bell, F. D. Lee, and J. D. Moody, *Rev. Sci. Instrum.* **72**, 698 (2001).
- <sup>97</sup> M. B. Schneider, O.S. Jones, N.B. Meezan, J.L. Milovich, R.P. Town, S.S. Alvarez, R.G. Beeler, D.K. Bradley, J. R. Celeste, S.N. Dixit, M.J. Edwards, M.J. Haugh, D. H. Kalantar, J.L. Kline, G.A. Kyrala, O.L. Landen, B.J. MacGowan, P. Michel, J.D. Moody, S. K. Oberhelman, K.W. Piston, M.J. Pivovarov, L. J. Suter, A.T. Teruya, C.A. Thomas, S.P. Vernon, A.L. Warrick, K. Widmann, R.D. Wood, B.K. Young, to be published in *Rev. Sci. Instrum.* (2010)
- <sup>98</sup> Peter Amendt, A. I. Shestakov, O. L. Landen, D. K. Bradley, S. M. Pollaine, L. J. Suter, and R. E. Turner, *Phys. Plasmas* **8**, 2908 (2001).
- <sup>99</sup> D. C. Wilson, A. J. Scannapieco, C. W. Cranfill, M. R. Clover, N. M. Hoffman, and J. Collins, *Phys Plasmas* **10**, 4427 (2003).
- <sup>100</sup> D. C. Wilson, R. L. Singleton, Jr., J. P. Grondalski, N. M. Hoffman, A. Nobile, Jr., F. H. Séguin, J. A. Frenje, C. K. Li, and R. D. Petrasso, *Rev. Sci. Instrum.* **77**, 10E711

---

(2006).

<sup>101</sup> N. D. Delamater, D. C. Wilson, G. A. Kyrala, A. Seifter, N. M. Hoffman, E. Dodd, R. Singleton, V. Glebov, C. Stoeckl, C. K. Li, R. Petrasso, and J. Frenje, *Rev. Sci. Instrum.* **79**, 10E526 (2008).

<sup>102</sup> J. A. Frenje, C. K. Li, J. R. Rygg, F. H. Séguin, D. T. Casey, R. D. Petrasso, J. Delettrez, V. Yu. Glebov, T. C. Sangster, O. Landen, and S. Hatchett, *Phys. Plasmas* **16**, 022702 (2009).

<sup>103</sup> David H. Cohen, Joseph J. MacFarlane, Paul Jaanimagi, Otto L. Landen, Donald A. Haynes, David S. Connors, Katherine L. Penrose, and Nathan S. Shupe, *Phys. Plasmas* **11**, 2702 (2004).

<sup>104</sup> B. A. Remington, B. A. Hammel, O. L. Landen, and R. A. Pasha, *Rev. Sci. Instrum.* **63**, 5083 (1992); B. A. Hammel, D. Griswold, O. L. Landen, T. S. Perry, B. A. Remington, P. L. Miller, T. A. Peyser, and J. D. Kilkenny, *Phys. Fluids B* **5**, 2259 (1993).

<sup>105</sup> J. A. Frenje, C. K. Li, F. H. Séguin, D. T. Casey, R. D. Petrasso, T. C. Sangster, R. Betti, V. Yu. Glebov, and D. D. Meyerhofer, *Phys. Plasmas* **16**, 042704 (2009).

<sup>106</sup> J. A. Frenje, C. K. Li, F. H. Seguin, J. Deciantis, S. Kurebayashi, J. R. Rygg, R. D. Petrasso, J. Delettrez, V. Yu. Glebov, C. Stoeckl, F. J. Marshall, D. D. Meyerhofer, T. C. Sangster, V. A. Smalyuk, and J. M. Soures, *Phys. Plasmas* **11**, 2798 (2004).

<sup>107</sup> V. Yu. Glebov, D. D. Meyerhofer, T. C. Sangster, C. Stoeckl, S. Roberts C. A. Barrera, J. R. Celeste, C. J. Cerjan, L. S. Dauffy, D. C. Eder, R. L. Griffith, S. W. Haan, B. A. Hammel, S. P. Hatchett, N. Izumi, J. R. Kimbrough, J. A. Koch, O. L. Landen, R. A. Lerche, B. J. MacGowan, M. J. Moran, E. W. Ng, T. W. Phillips, P. M. Song, R. Tommasini, B. K. Young, S. E. Caldwell, G. P. Grim, S. C. Evans, J. M. Mack, T. J.

---

Sedillo, M. D. Wilke, D. C. Wilson, C. S. Young D. Casey, J. A. Frenje, C. K. Li, R. D. Petrasso, F. H. Séguin, J. L. Bourgade, L. Disdier, M. Houry, I. Lantuejoul, O. Landoas, G. A. Chandler, G. W. Cooper, R. J. Leeper, R. E. Olson, C. L. Ruiz, and M. A. Sweeney, S. P. Padalino, C. Horsfield, and B. A. Davis., *Rev. Sci. Instrum.* **77**, 10E715 (2006).

<sup>108</sup> R. E. Olson, G. A. Rochau, R. J. Leeper, and O.L. Landen, submitted to *Phys. Plasmas* (2010).

<sup>109</sup> A.B. Bullock, O.L. Landen, B.E. Blue, J. Edwards and D.K. Bradley, *J. Appl. Phys.* **100**, 043301 (2006).

<sup>110</sup> R.E. Olson, M. Geissel, J.W. Kellogg, D.G. Hicks, B.K. Spears, J.P. Holder, O.L. Landen, G.R. Bennett, A.D. Edens, B.W. Atherton, R.J. Leeper, *Rev. Sci. Instrum.* **79**, 10E913 (2008).

<sup>111</sup> A. V. Okishev, R. G. Roides, I. A. Begishev, and J. D. Zuegel, *Proc. SPIE* **6053**, 60530J (2006).

<sup>112</sup> F. Girard, J. P. Jadaud, M. Naudy, B. Villette, D. Babonneau, M. Primout, M. C. Miller, R. L. Kauffman, L. J. Suter, J. Grun, and J. Davis, *Phys. Plasmas* **12**, 092705 (2005); D. Babonneau, M. Primout, F. Girard, J.-P. Jadaud, M. Naudy, B. Villette, S. Depierreux, C. Blancard, G. Faussurier, K. B. Fournier, L. Suter, R. Kauffman, S. Glenzer, M. C. Miller, J. Grun, and J. Davis, *Phys. Plasmas*. **15**, 092702 (2008).

<sup>113</sup> Jonathan Workman and George A. Kyrala, *Proc. SPIE Vol.* **4504**, 168 (2001).

<sup>114</sup> H. Huang, A. Nikroo, R. B. Stephens, S. A. Eddinger, D. R. Wall, K. A. Moreno, and H. W. Xu, *Fusion Sci. Technol.* **55**, 536 (2009).

- 
- <sup>115</sup> B.J. Kozioziemski, D.S. Montgomery, J.D. Sater, J.D. Moody, C. Gautier, and J.W. Pipes, Nucl. Fusion **47**, 1 (2007).
- <sup>116</sup> P. Michel, L. Divol, E. A. Williams, S. Weber, C. A. Thomas, D. A. Callahan, S. W. Haan, J. D. Salmonson, S. Dixit, D. E. Hinkel, M. J. Edwards, B. J. MacGowan, J. D. Lindl, S. H. Glenzer, and L. J. Suter, Phys. Rev. Lett. **102**, 025004 (2009); P. Michel, L. Divol, E. A. Williams, C. A. Thomas, D. A. Callahan, S. Weber, S. W. Haan, J. D. Salmonson, N. B. Meezan, O. L. Landen, S. Dixit, D. E. Hinkel, M. J. Edwards, B. J. MacGowan, J. D. Lindl, S. H. Glenzer, and L. J. Suter, Phys Plasmas **16**, 042702 (2009).
- <sup>117</sup> Robert L. Kauffman, L. V. Powers, S. N. Dixit, S. G. Glendinning, S. H. Glenzer, R. K. Kirkwood, O. L. Landen, B. J. MacGowan, J. D. Moody, T. J. Orzechowski, D. M. Pennington, G. F. Stone, L. J. Suter, R. E. Turner, T. L. Weiland, A. L. Richard and M. A. Blain Phys. Plasmas **5**, 1927 (1998).
- <sup>118</sup> E. L. Dewald, O. S. Jones, O. L. Landen, L. Suter, P. Amendt, R. E. Turner, and S. Regan, Rev. Sci. Instrum. **77**, 10E310 (2006).
- <sup>119</sup> L. J. Suter, A. A. Hauer, L. V. Powers, D. B. Ressler, N. Delameter, W. W. Hsing, O. L. Landen, A. R. Thiessen, and R. E. Turner, Phys. Rev. Lett. **73**, 2328 (1994).
- <sup>120</sup> O. L. Landen, P. A. Amendt, L. J. Suter, R. E. Turner, S. G. Glendinning, S. W. Haan, S. M. Pollaine, B. A. Hammel, M. Tabak, M. D. Rosen, and J. D. Lindl, Phys. Plasmas **6**, 2137 (1999).
- <sup>121</sup> J. Kimbrough, J.D. Moody, P.M. Bell, and O.L. Landen, Rev. Sci. Instrum. **75**, 4060 (2004).
- <sup>122</sup> T. J. Murphy, J. M. Wallace, N. D. Delamater, Cris W. Barnes, P. Gobby, A. A. Hauer, E. Lindman, G. Magelssen, J. B. Moore, J. A. Oertel, R. Watt, O. L. Landen, P.

---

Amendt, M. Cable, C. Decker, B. A. Hammel, J. A. Koch, L. J. Suter, R. E. Turner, R. J. Wallace, F. J. Marshall, D. Bradley, R. S. Craxton, R. Keck, J. P. Knauer, R. Kremens, and J. D. Schnittman., *Phys. Rev. Lett.* **81**, 108 (1998).

<sup>123</sup> R. E. Turner, P. Amendt, O. L. Landen, S. G. Glendinning, P. Bell, C. Decker, B. A. Hammel, D. Kalantar, D. Lee, R. Wallace, D. Bradley, M. Cable, R. S. Craxton, R. Kremens, W. Seka, J. Schnittman, K. Thorp, T. J. Murphy, N. Delamater, Cris W. Barnes, A. Hauer, G. Magelssen, and J. Wallace, *Phys. Plasmas* **7**, 333 (2000).

<sup>124</sup> R.E. Turner, P.A. Amendt, O.L. Landen, L.J. Suter, R.J. Wallace, and B.A. Hammel, *Phys. Plasmas* **10**, 2429 (2003).

<sup>125</sup> P.A. Amendt, R.E. Turner, and O. L. Landen, *Phys. Rev. Lett.* **89**, 165001 (2002).

<sup>126</sup> George A. Kyrala, Achim Seifter, John Kline. Nelson Hoffman, and S. Robert Goldman *Bull. Am. Phys. Soc.* **53**, 247 (2008); G. A. Kyrala, A. Seifter, J. L. Kline, S. R. Goldman, S. H. Batha, and N. M. Hoffman, submitted to *Phys. Rev. Lett.* (2010).

<sup>127</sup> Peter Amendt, C. Cerjan, D.E. Hinkel, J.L. Milovich, H.-S. Park, and H.F. Robey, *Phys. Plasmas* **15**, 012702 (2008).

<sup>128</sup> G. A. Kyrala, S. Dixit, S. Glenzer. D. Kalantar, D. Bradley, N. Izumi, N. Meezan, O.L. Landen, D. Callahan, S. V. Weber, J. P. Holder, S. Glenn, M. J. Edwards, P. Bell, J. Kimbrough, J. Koch, R. Prasad, L. Suter, and J. Kilkenny, to be published in *Rev. Sci. Instrum.* (2010).

<sup>129</sup> K.C. Chen, Y.T. Lee, H. Huang, J.B. Gibson, A. Nikroo, M.A. Johnson, and E. Mapoles, *Fusion Sci. Technol.* **51**, 593 (2007).

<sup>130</sup> John Edwards, Marty Marinak, Tom Dittrich, Steve Haan, Jorge Sanchez, Jeff Klingmann, and John Moody, *Phys. Plasmas* **12**, 056318 (2005); G. R. Bennett, M. C.

---

Herrmann, M. J. Edwards, B. K. Spears, C. A. Back, E. W. Breden, P. J. Christenson, M. E. Cuneo, K.L. Dannenburg, C. Frederick, K. L. Keller, T. D. Mulville, A. Nikroo, K. Peterson, J.L. Porter, C.O. Russell, D. B. Sinars, I. C. Smith, R. M. Stamm, and R. A. Vesey, *Phys. Rev. Lett.* **99**, 205003 (2007).

<sup>131</sup> S. Langer, Nobuhiko Izumi, Thomas R. Dittrich and Steven W. Haan, *High Energ. Dens. Phys.* **3**, 169 (2007).

<sup>132</sup> J. A. Koch, T. W. Barbee, Jr., N. Izumi, R. Tommasini, R. C. Mancini, L. A. Welser, and F. J. Marshall, *Rev. Sci. Instrum.* **76**, 073708 (2005).

<sup>133</sup> S.H. Langer, H.A. Scott, M.M. Marinak and O.L. Landen, *J. of Quant. Spectrosc. & Radiat. Transfer* **71**, 479 (2001).

<sup>134</sup> B. A. Hammel, C. J. Keane, M. D. Cable, D. R. Kania, J. D. Kilkenny, R. W. Lee, and R. Pasha, *Phys Rev. Lett.* **70**, 1263 (1993).

<sup>135</sup> E.L. Dewald, C. Thomas, S. Hunter, L. Divol, N. Meezan, S.H. Glenzer, L.J. Suter, E. Bond, J. Kline, J. Celeste, R.L. Kauffman, J. Kilkenny and O.L. Landen, to be published in *Rev. Sci. Instrum.* (2010).

<sup>136</sup> S. P. Regan, N. B. Meezan, L. J. Suter, D. J. Strozzi, W. L. Kruer, D. Meeker, S. H. Glenzer, W. Seka, C. Stoeckl, V. Yu. Glebov, T. C. Sangster, D. D. Meyerhofer, R. L. McCrory, E. A. Williams, O. S. Jones, D. A. Callahan, M. D. Rosen, O. L. Landen, C. Sorce, and B. J. MacGowan, *Phys. Plasmas* **17**, 020703 (2010).

<sup>137</sup> A. Simon, R. W. Short, E. A. Williams, and T. Dewandre, *Phys. Fluids* **26**, 3107 (1983).

<sup>138</sup> H. Sawada, S. P. Regan, D. D. Meyerhofer, I. V. Igumenshchev, V. N. Goncharov, T. R. Boehly, R. Epstein, T. C. Sangster, V. A. Smalyuk, B. Yaakobi, G. Gregori, S. H.

---

Glenzer and O. L. Landen, *Phys. Plasmas* **14**, 122703 (2007); Andrea L. Kritcher, Paul Neumayer, John Castor, Tilo Döppner, Roger W. Falcone, Otto L. Landen, Hae Ja Lee, Richard W. Lee, Edward C. Morse, Andrew Ng, Steve Pollaine, Dwight Price, Siegfried H. Glenzer, *Science* **322**, 69 (2008); H. J. Lee, P. Neumayer, J. Castor, T. Döppner, R. W. Falcone, C. Fortmann, B. A. Hammel, A. L. Kritcher, O. L. Landen, R. W. Lee, D. D. Meyerhofer, D. H. Munro, R. Redmer, S. P. Regan, S. Weber, and S. H. Glenzer, *Phys. Rev. Lett.* **102**, 115001 (2009).

<sup>139</sup> Andrea Kritcher, Tilo Doeppner, Hae Ja Lee, Paul Davis, Otto Landen, and Siegfried Glenzer, *Bull. Am. Phys. Soc.* **54**, 354 (2009);

<sup>140</sup> G. R. Bennett, D. B. Sinars, D. F. Wenger, M. E. Cuneo, R. G. Adams, W. J. Barnard, D. E. Beutler, R. A. Burr, D. V. Campbell, L. D. Claus, J. S. Foresi, D. W. Johnson, K. L. Keller, C. Lackey, G. T. Leifeste, L. A. McPherson, T. D. Mulville, K. A. Neely, P. K. Rambo, D. C. Rovang, L. E. Ruggles, J. L. Porter, W. W. Simpson, I. C. Smith, and C. S. Speas, *Rev. Sci. Instrum.* **77**, 10E322 (2006).

<sup>141</sup> Jeffrey A. Koch, Otto L. Landen, Bernard J. Kozioziemski, Nobuhiko Izumi, Eduard L. Dewald, Jay D. Salmonson, and Bruce A. Hammel, *J. Appl. Phys.* **105**, 1 (2009).

TABLE I. Expected initial and residual post-tune  $1\sigma$  offset from optimum ignition implosion performance, associated initial and post-tune  $1\sigma$  offsets in optimal laser and target parameters, and required accuracy for tuning associated observables.

Implosion Performance Offsets			Laser or Target Offsets			Tuning Accuracy	
Parameter	Initial	Final	Parameter	Initial	Final	Observable	Value
DT Fuel	+10%	+3%	1 <sup>st</sup> 2ns Inner Cone	$\pm 50\%$	$\pm 10\%$	Reemit P <sub>2</sub> flux	$\pm 15\%$
Adiabat			Energy Fraction			asymmetry	
Implosion Core	50%	15%	1 <sup>st</sup> 2ns Inner Cone	$\pm 50\%$	$\pm 10\%$	Reemit P <sub>2</sub> flux	$\pm 15\%$
Asymmetry	rms	rms	Energy Fraction			asymmetry	
DT Fuel	+10%	+3%	1 <sup>st</sup> 2ns Laser	$\pm 20\%$	$\pm 10\%$	1 <sup>st</sup> Shock	$\pm 5\%$
Adiabat			Power			velocity	
DT Fuel	+10%	+3%	Trough Laser	$\pm 20\%$	$\pm 10\%$	1 <sup>st</sup> Shock	$\pm 5\%$
Adiabat			Power			velocity	
DT Fuel	+10%	+3%	2 <sup>nd</sup> Shock Laser	$\pm 10\%$	$\pm 4\%$	2 <sup>nd</sup> Shock	$\pm 2\%$
Adiabat			Power			velocity	
DT Fuel	+10%	+3%	3 <sup>rd</sup> Shock Laser	$\pm 10\%$	$\pm 4\%$	3 <sup>rd</sup> Shock	$\pm 2\%$
Adiabat			Power			velocity	
DT Fuel	+10%	+3%	2 <sup>nd</sup> Shock Launch	$\pm 200\text{ps}$	$\pm 50\text{ps}$	2 <sup>nd</sup> Shock	$\pm 6$
Adiabat			Time			overtake point	$\mu\text{m}$
DT Fuel	+10%	+3%	3 <sup>rd</sup> Shock Launch	$\pm 200\text{ps}$	$\pm 50\text{ps}$	3 <sup>rd</sup> Shock	$\pm 6$
Adiabat			Time			overtake point	$\mu\text{m}$
DT Fuel	+10%	+3%	4 <sup>th</sup> Shock Launch	$\pm 200\text{ps}$	$\pm 100\text{ps}$	4 <sup>th</sup> Shock	$\pm 100$
Adiabat			time			breakout time	ps
DT Fuel	+10%	+3%	4 <sup>th</sup> Rise Duration	$\pm 200\text{ps}$	$\pm 100\text{ps}$	4 <sup>th</sup> rise Tr slope	$\pm 5\%$
Adiabat						to peak power	
Ablator Mass	$\pm 80\%$	$\pm 25\%$	Initial Ablator	$\pm 30$	$\pm 10$	Symcap Mass	$\pm 13\%$
Remaining			Thickness	$\mu\text{m}$	$\mu\text{m}$	Remaining	
Peak Implosion	$\pm 10\%$	$\pm 2\%$	Peak Laser Power	$\pm 20\%$	$\pm 4\%$	Velocity at r =	$\pm 2\%$
Velocity						300 $\mu\text{m}$	
Implosion Core	50%	16%	Peak Inner Cone	$\pm 20\%$	$\pm 5\%$	Symcap P <sub>2</sub> core	$\pm 7.5$
Asymmetry	rms	rms	Energy Fraction			asymmetry	%
Implosion Core	50%	16%	Hohlraum Length	$\pm 400$	$\pm 200$	Symcap P <sub>4</sub> core	$\pm 7.5$
Asymmetry	rms	rms		$\mu\text{m}$	$\mu\text{m}$	asymmetry	%
Ablator-fuel	$\pm 40\%$	$\pm 15\%$	Mid-Z Ablator	$\pm 0.5\%$	$\pm 0.1\%$	2-5 keV x-rays	$\pm 10\%$
Mix			Dopant Fraction			in hohlraum	
Peak Implosion	$\pm 10\%$	$\pm 2\%$	Peak Laser Power	$\pm 20\%$	$\pm 4\%$	Symcap	$\pm 50$
Velocity						Bangtime	ps



TABLE II. Expected sensitivities of capsule implosion observables to 10% increase in key target, laser and physics parameters.

Parameter Increased by 10%	Change in Observable		Bangtime
	Ablator Mass Remaining (% of Initial Mass)	Peak Velocity	
Capsule Thickness	+1.6 %	-3 %	+100 ps
Laser Peak Flux	-0.9 %	+5 %	-150 ps
Ablator Opacity	+2.5 %	-2 %	+70 ps
M-band Flux	-0.4 %	+0.25 %	-7 ps

## Figure Captions

Figure 1. a) Schematic of the 300 eV CH indirect-drive ignition target. b) Capsule cross-section. c) Total laser power (solid) and radiation temperature  $T_r$  at capsule (dashed) versus time.

Figure 2. a) Schematic of the alternate 285 eV Be indirect-drive ignition target. b) Capsule cross-section. c) Total laser power (solid) and radiation temperature  $T_r$  at capsule (dashed) versus time.

Figure 3. Predicted probability of ignition versus Ignition Threshold Factor (ITF) is long dashed curve. Predicted ITF distributions before after capsule tuning experiments and after cryogenically layered capsule experiments are short dashed, solid and dot-dashed curves, respectively.

Figure 4: Schematic of 14 laser and target parameters varied.

Figure 5. a) Re-emission sphere experimental set-up for NIF shots. b) Power per beam for 48 inner cone beams (solid), 128 outer cone beams (dashed), and for 16 inner cone beams that would hit patches (dot-dashed).

Figure 6. Ratio of reemitted  $P_2/P_0$  asymmetry at 400, 700 and 1200 eV photon energies to incident spectrally integrated  $P_2/P_0$  asymmetry 3 ns into a calculated drive equivalent to a 97 eV Planckian. Solid line is analytic Planckian prediction.

Figure 7. Calculated incident  $P_2/P_0$  integrated over 1<sup>st</sup> 2 ns for re-emission sphere (black circles) versus ignition capsule (red squares) as a function of inner cone energy fraction.

Figure 8. a) Re-emission sphere experimental set-up with example OMEGA data. b) Instantaneous  $P_2/P_0$  x-ray emission data at 900 eV for inner cone fraction = 0.12 from 1.4 mm diameter re-emission sphere using 6.4 mm long hohlraums and 100 eV peak drive. Solid curves are postprocessed results from 3D Hydra simulations assuming full coupling (black) and 90% coupling on the inner cone (blue).

Figure 9. a)  $P_2/P_0$  of 900 eV (open squares) and 1200 eV (closed circles) x-ray emission from 1.4 mm diameter re-emission sphere versus inner cone fraction at 0.7 ns using 6.4 mm long hohlraums and 100 eV drive. Solid and dashed lines are postprocessed results from 3D Hydra simulations for 1200 and 900 eV channels, respectively. b) Comparison of measured vs calculated reemission sphere image at 1200 eV for inner cone fraction = 0.12 at  $t = 1$  ns.

Figure 10. a) 1<sup>st</sup> three shock tuning experimental set-up for NIF shots and simulated VISAR fringe data. b) Power per beam for 64 inner cone beams (solid), 128 outer cone

beams (dashed). c) Simulated output of leading shock velocity versus time that might be expected with third shock delayed intentionally.

Figure 11. Calculated late time shock trajectories in ablator and fuel in initial Lagrangian coordinates for a) surrogate capsule filled with liquid D<sub>2</sub> and b) ignition capsule with DT solid and gas.

Figure 12. Computed (symbols) and analytic (line) a) change in first shock velocity versus change in power in trough of NIC pulse, b) change in second shock overtake distance versus change in second shock laser power and c) change in second shock overtake distance versus change in second shock launch time.

Figure 13. OMEGA experimental set-up for testing 1<sup>st</sup> three shocks reentrant geometry, including example VISAR data.

Figure 14. Schematic showing important parts of 4<sup>th</sup> rise, with 2 examples (solid and dashed) yielding same shock coalescence time.

Figure 15. Calculated a) average fuel entropy deviations and b) peak shell velocity deviations from nominal vs. up to  $\pm 300$  ps changes in 4<sup>th</sup> rise duration and 4<sup>th</sup> rise mid-point time. The horizontal contours represent  $\pm 3.5$  eV/ns variability in 4<sup>th</sup> rise Tr slope and the vertical contours represent  $\pm 90$  ps in 4<sup>th</sup> shock breakout time.

Figure 16. a) 4<sup>th</sup> rise tuning experimental set-up for NIF shots. b) Power per beam for 64 inner cone beams (solid), 128 outer cone beams (dashed).

Figure 17. a) OMEGA experimental set-up for testing 4<sup>th</sup> rise tuning reentrant probing geometry. b) Example VISAR streak showing signature of shock breakout of interest later in time.

Figure 18. Measured Dante Tr during a) last 5 ns and b) zooming in on 4<sup>th</sup> rise of 19 ns long 840 kJ pulses driving 5.44 mm diameter hohlraums at NIF. Different colors represent three separate shots. Dashed lines are linear fits to the data. Shots had nominally identical pulseshapes but smaller wavelength separation (3 vs 8.5Å) for shot N091030 (red curve) and 50% lower gas-fill for shot N091120 (blue curve).

Figure 19. Calculated ablator-fuel mix fraction versus ablator mass remaining for Be (squares) and CH (circles) designs, with analytic fits overplotted.

Figure 20. Calculated peak implosion velocity and remaining ablator mass sensitivity to variations in peak laser power (along black contours spaced every 7% in thickness) and initial ablator mass (along red contours spaced every 10% in peak flux). The black and red arrows signify increasing flux and thickness, respectively.

Figure 21. a) Calculated streaked radiograph of BeCu target with 6.7 keV backlighter. b) Extracted transmission lineout corresponding to  $r = 300 \mu\text{m}$  shell radius.

Figure 22. Streaked capsule radiography experimental set-up for NIF shots. b) Power per beam for 64 inner cone beams (solid), 120 outer cone beams (dashed), and 8 50° beams used for backlighter (dot-dashed).

Figure 23. Simulated 9 keV transmission profiles at near peak velocity for 15% mass remaining of 300 eV, 1.3 MJ CH(Ge) implosion including (blue solid) and without (black dashed) idealized Rayleigh-Taylor spike growth at the ablation front.

Figure 24. a) Example of streaked 5.2 keV radiograph of 0.5 mm initial diameter BeCu capsule driven by OMEGA 200 eV, 2.5 ns shaped drive hohlraum. b) Solid points are extracted peak implosion velocity versus % ablator mass remaining from 6 shots using 30  $\mu\text{m}$  (black) and 40  $\mu\text{m}$  (red) initial thickness graded doped BeCu shells. Open squares are postshot Lasnex simulations.

Figure 25. Schematics of qualitative variations in  $P_2$  and  $P_4$  core shapes as a function of changes in cone power balance and in hohlraum length, with pointing staying fixed with respect to LEH plane.

Figure 26. Calculated symmetry capsule core  $P_2/P_0$  (solid) and  $P_4/P_0$  (dashed) as a function of 4<sup>th</sup> pulse inner cone fraction for three hohlraum lengths: nominal + 400  $\mu\text{m}$  (red), nominal (black) and nominal – 400  $\mu\text{m}$  (blue).

Figure 27. a) Symmetry capsule core x-ray imaging experimental set-up for NIF shots. b) Power per beam for 64 inner cone beams (solid) and 128 outer cone beams (dashed).

Figure 28. Comparison of calculated trajectory of inner ablator of symmetry capsule (black) versus trajectory of DT fuel of ignition capsule (red). Also shown is total laser power profile.

Figure 29. a) Calculated a)  $P_2/P_0$  and b)  $P_4/P_0$  asymmetry for symmetry capsule versus ignition capsule core images for various imposed levels of flux asymmetry.

Figure 30. OMEGA 5 keV core images and  $P_2/P_0$  of emission shape versus inner cone fraction from imploded 50 atm.-fill CH capsule driven by 1 ns-duration 270 eV peak hohlraum drive.

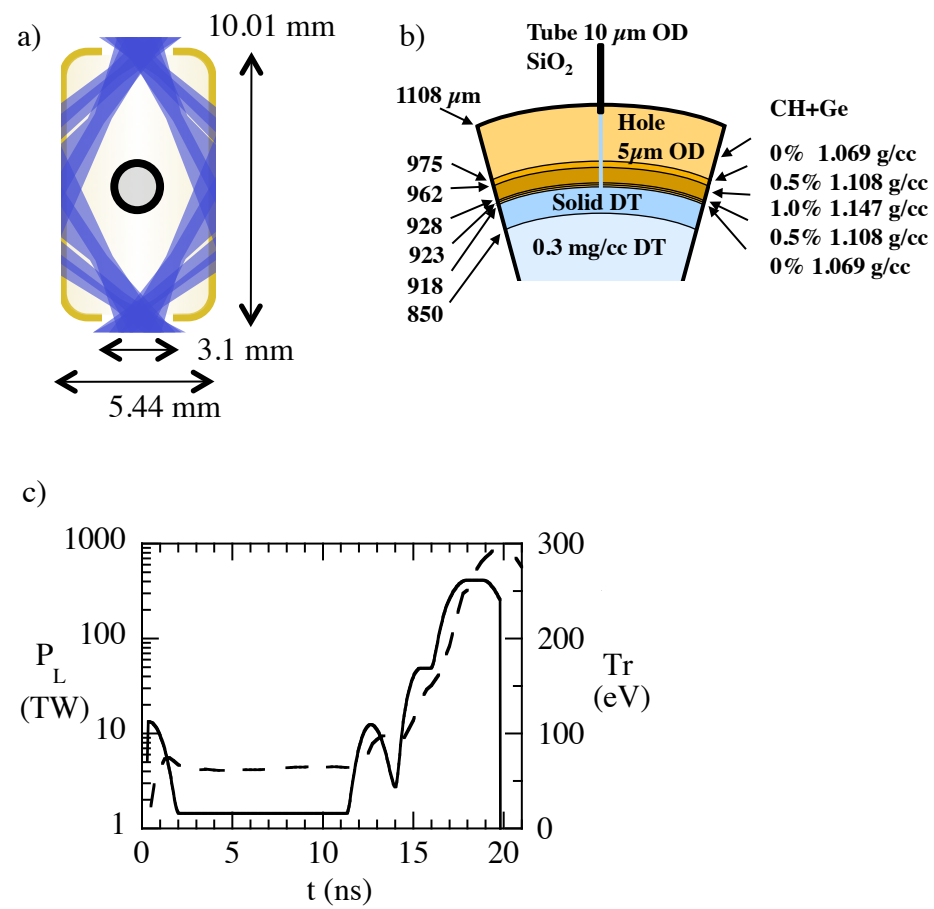
Figure 31. (Color online). a) Gated 8-10 keV, 10  $\mu\text{m}$ , 70 ps resolution x-ray images from pole and equator view of convergence ratio =15 CH capsules driven by 500 kJ 270 eV peak temperature NIF hohlraums. b) Extracted  $P_2/P_0$  (circles) and  $P_4/P_0$  (diamonds) versus time.

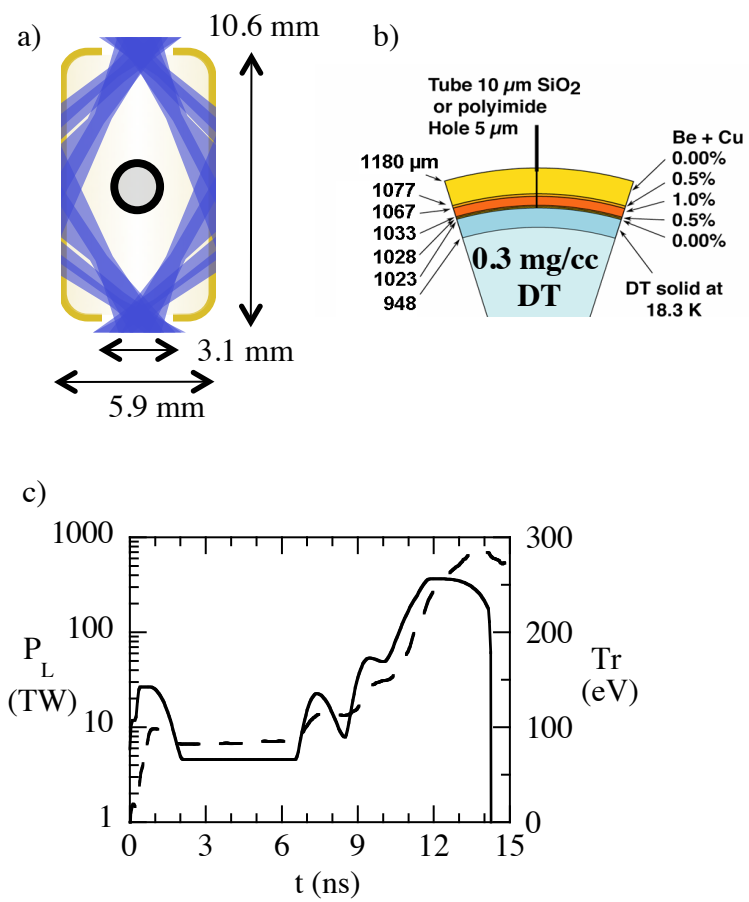
Figure 32. Illustrative example of how a number of shots measuring ablator mass remaining will be used to check variability and to set the optimum associated target parameter, the initial ablator thickness, and its  $1\sigma$  uncertainty.

Figure 33. Residual variances after tuning in random measurement error, systematic errors, target metrology errors, and laser diagnostic errors normalized to budget for each of the laser and target adjustable parameters.

Figure 34. Matrix of shot tuning type displayed in chronological order from top to bottom versus laser or target parameter. Green boxes on diagonal mean that shot observable is affected by and sets that parameter, and of-diagonal yellow and orange boxes mean that shot is affected by that parameter but does not set it. Value in each orange box above diagonal is expected cross-coupling sensitivity normalized to error budget.







**Figure 2 (Color)**

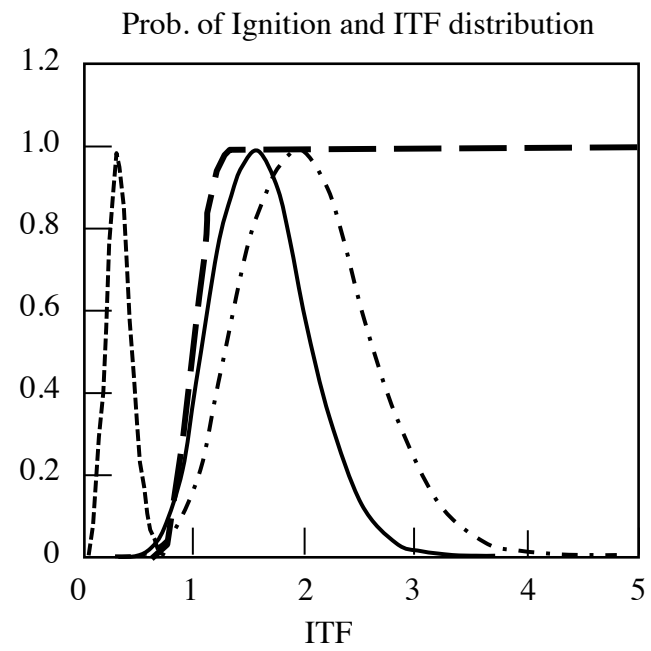


**Figure 3**

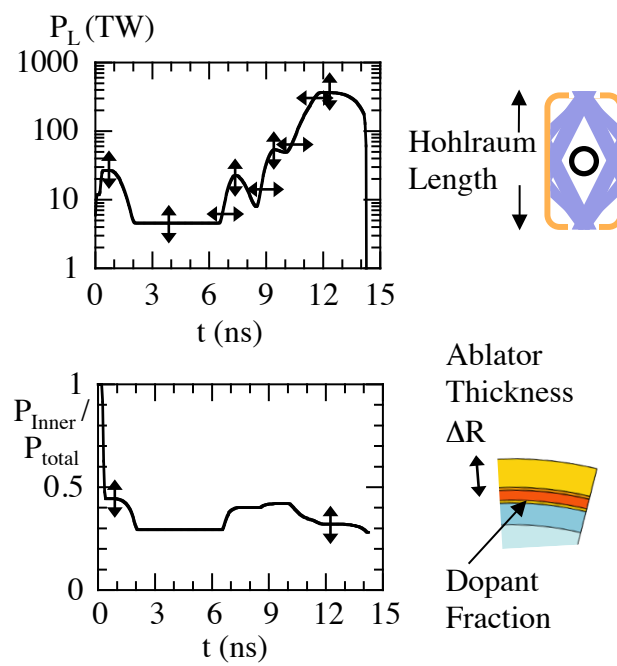


**Figure 4 (Color)**

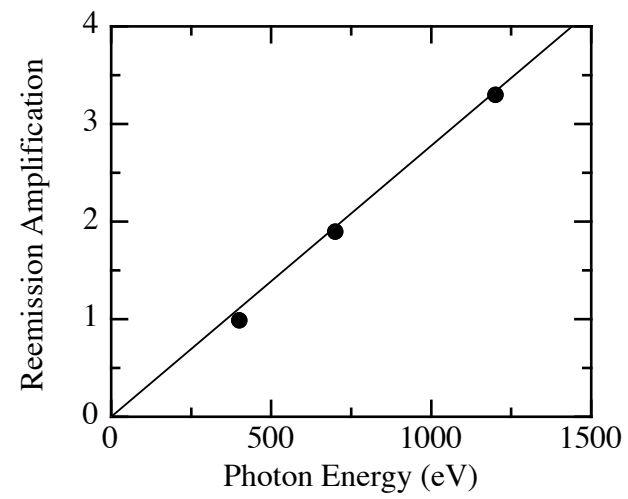


**Figure 5**

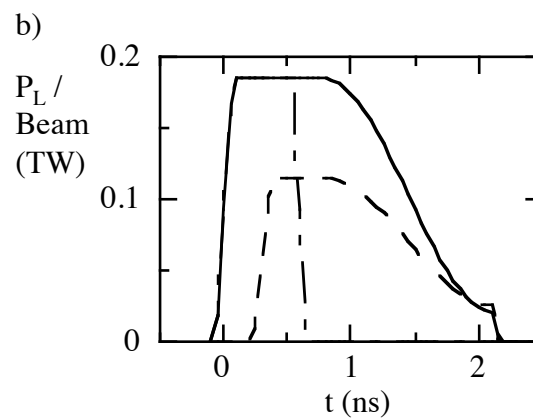
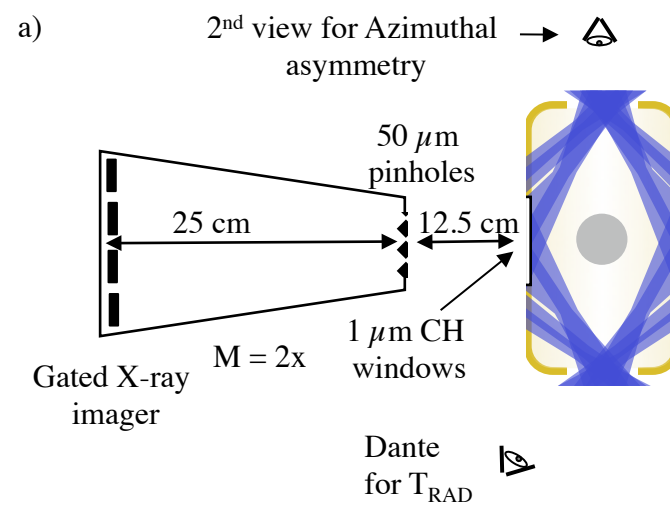


**Figure 6 (Color)**

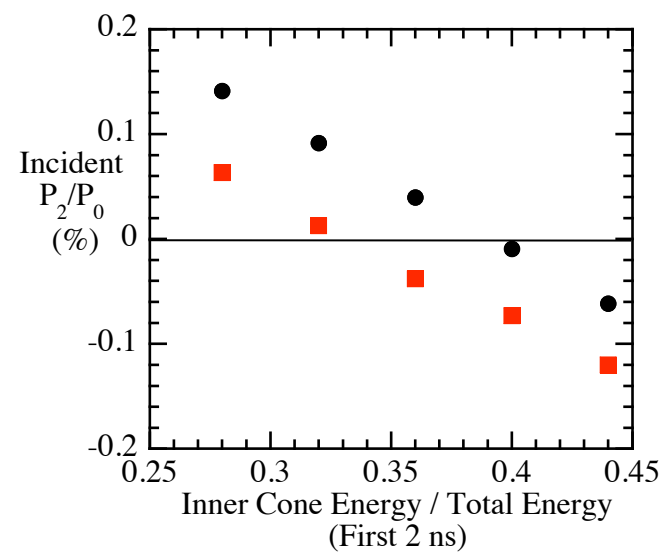


**Figure 7**

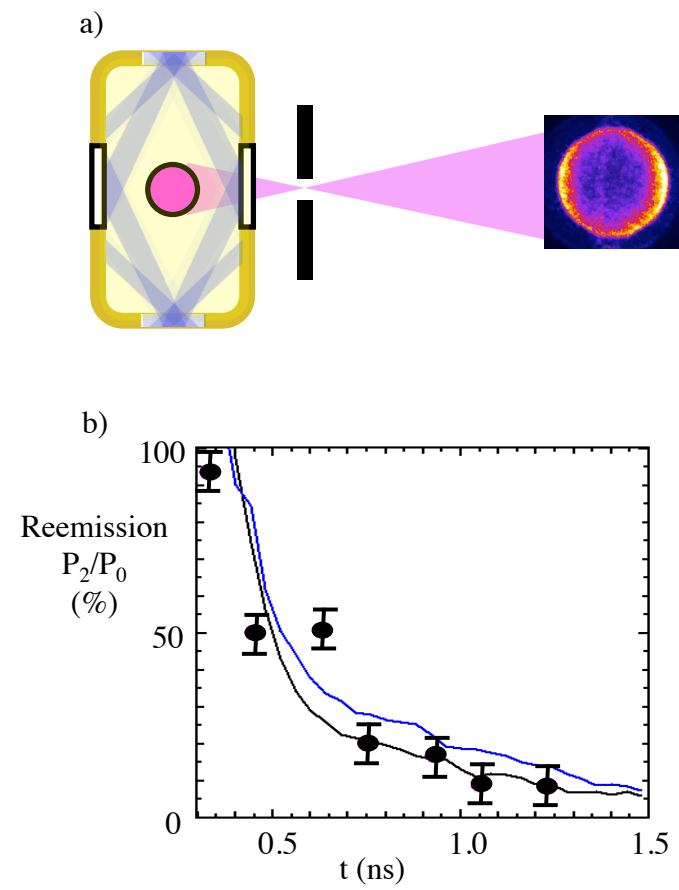
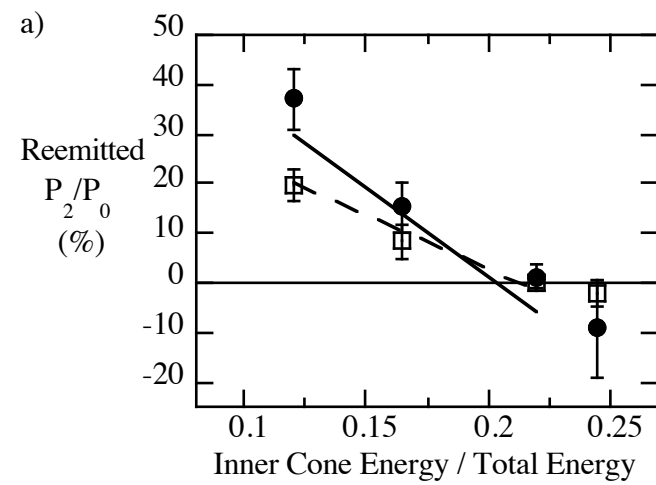


**Figure 8 (Color)**





b)

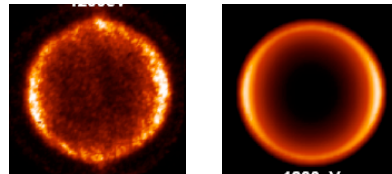


**Figure 9 (Color)**

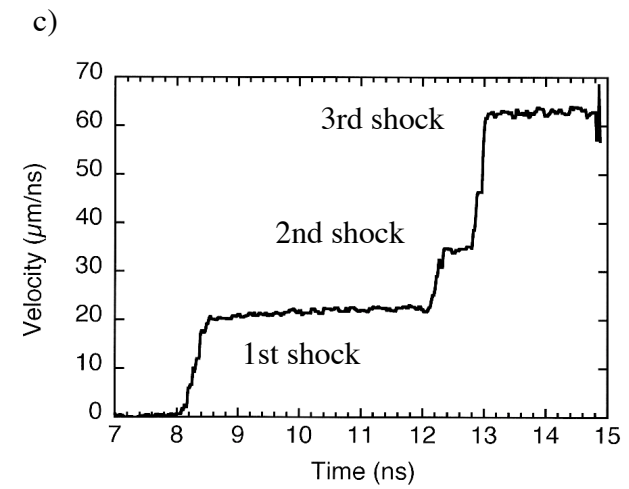
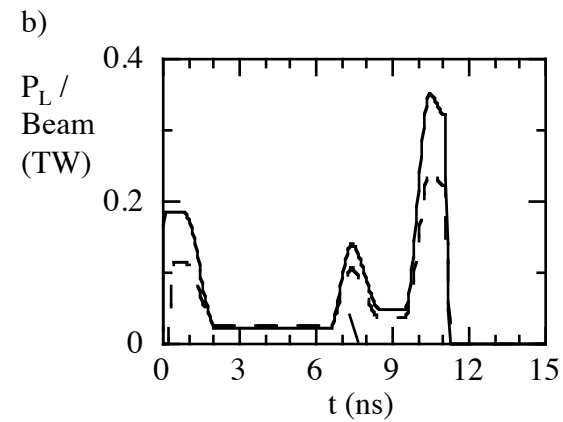
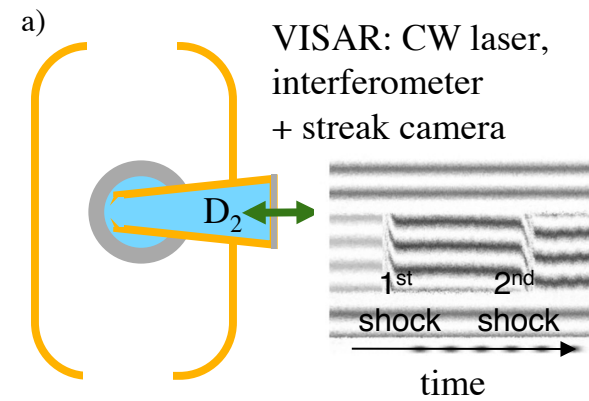


**Figure 10 (Color)**

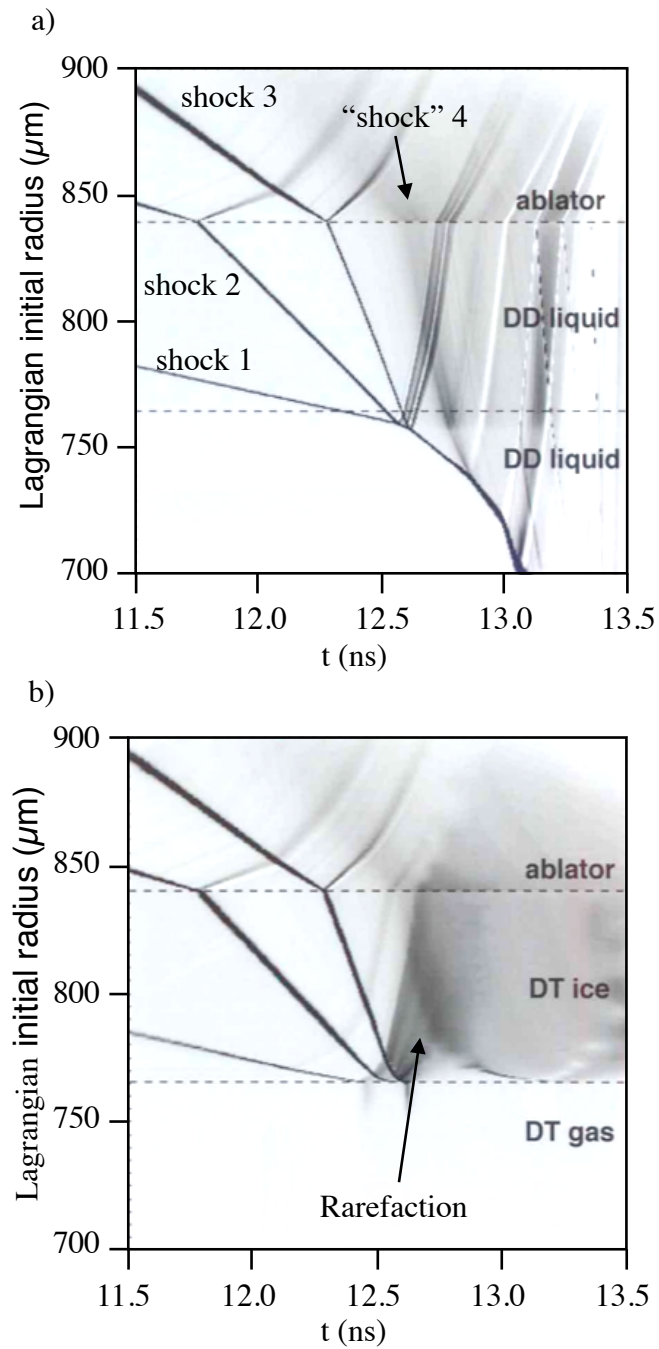
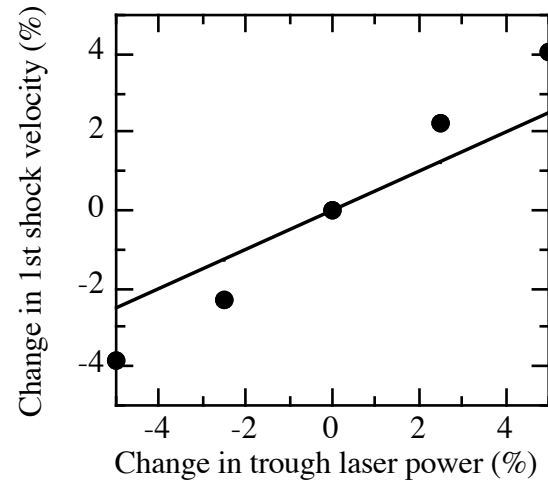
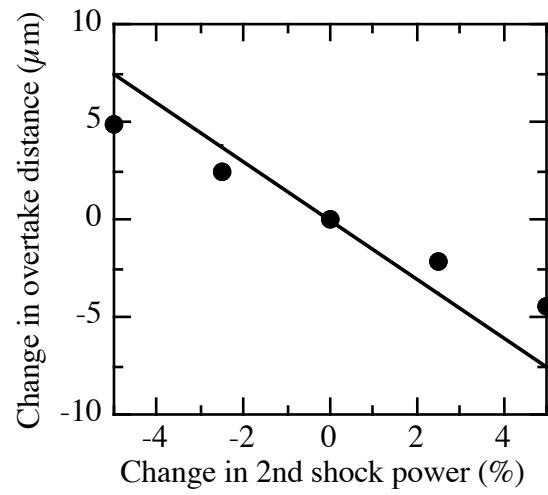


**Figure 11**

a)



b)



c)

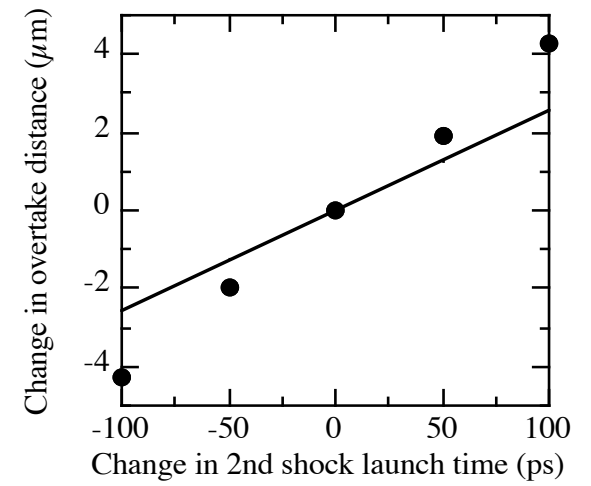
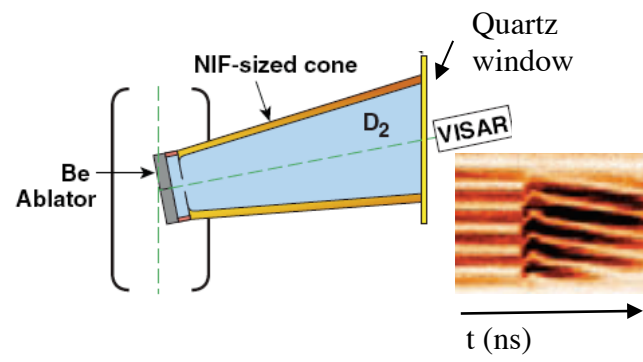
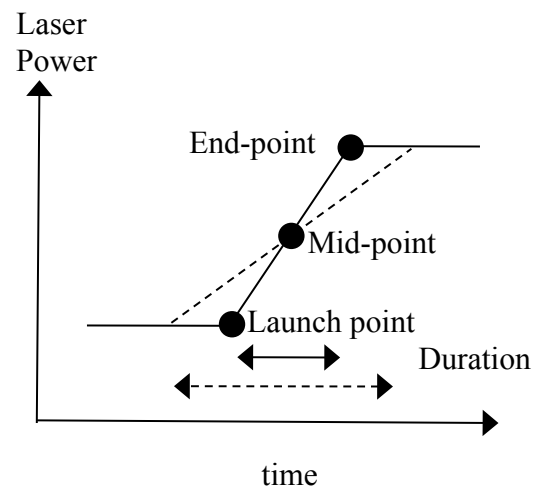


Figure 12



**Figure 13 (Color)**



**Figure 14**

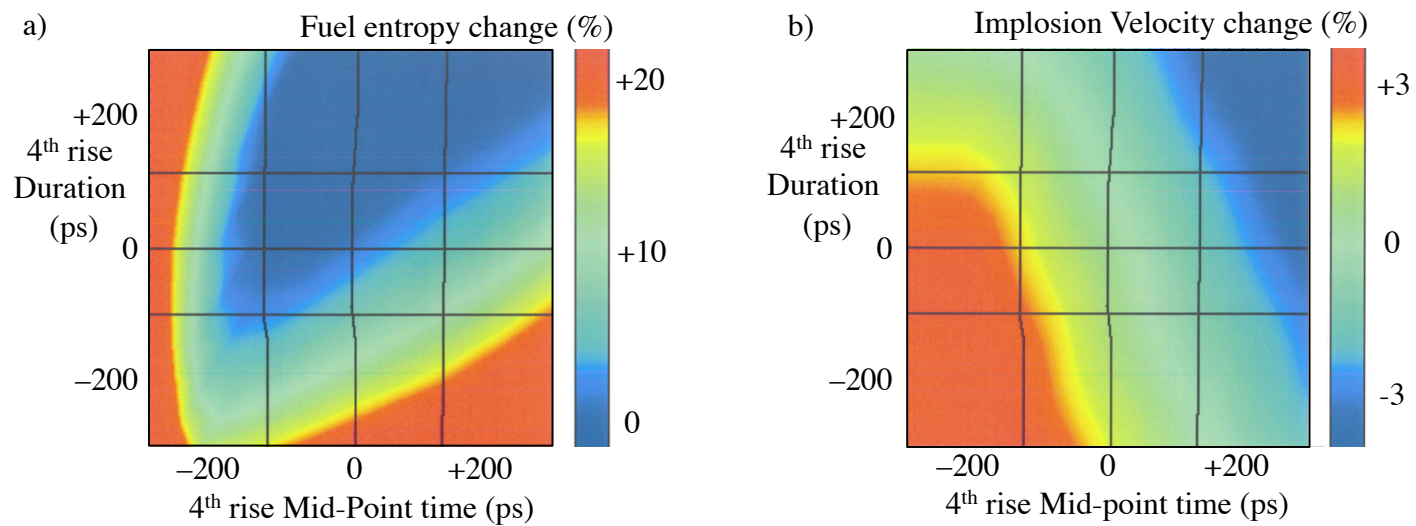


**Figure 15 (Color)**

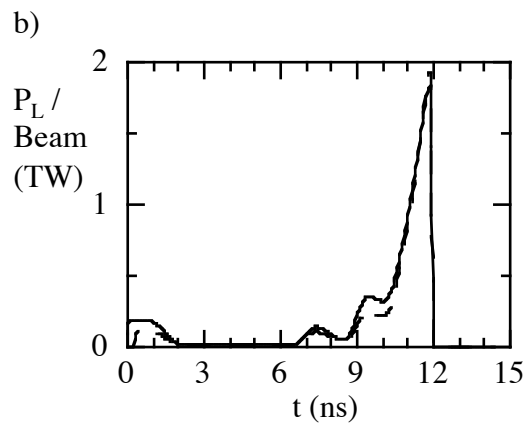
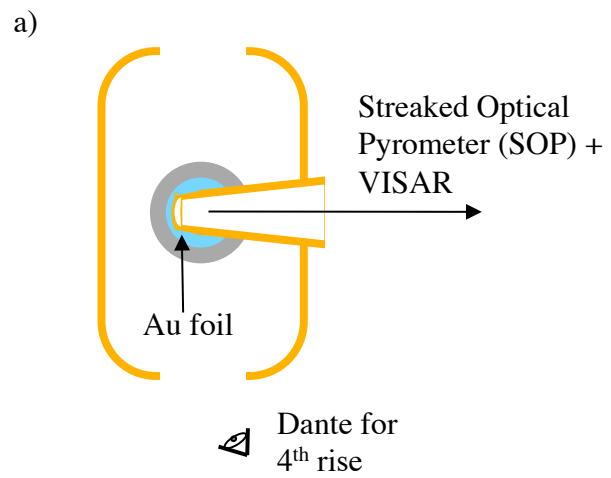


**Figure 16 (Color)**



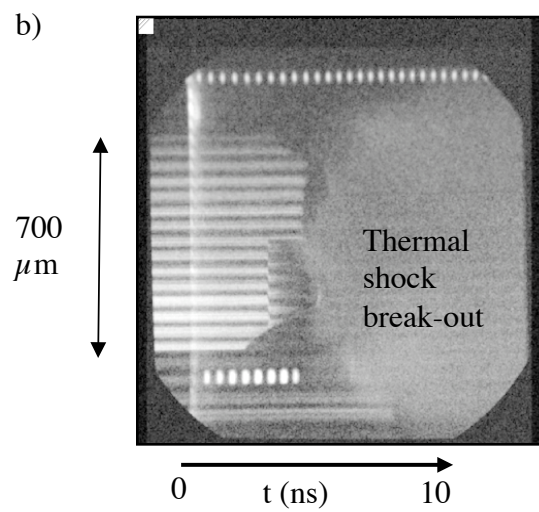
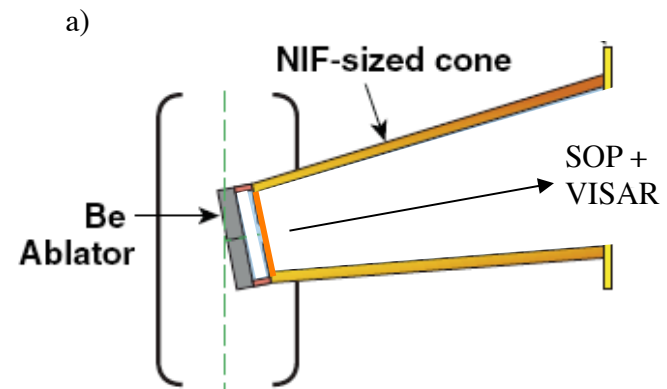


**Figure 17 (Color)**

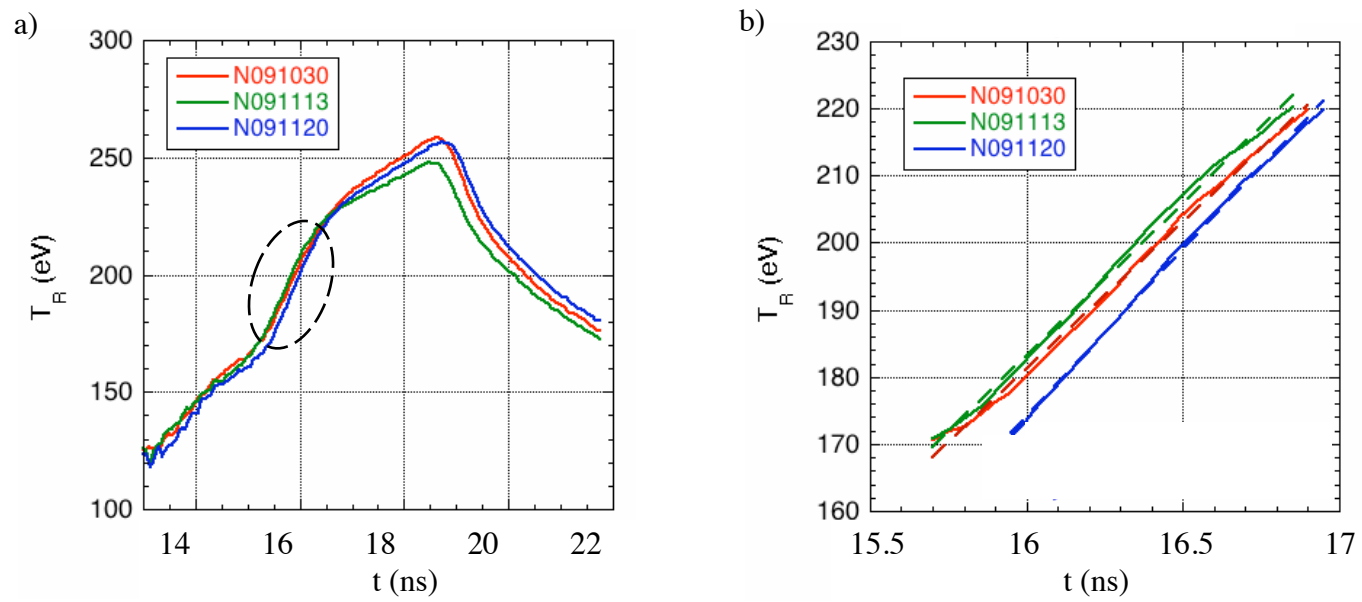


**Figure 18**

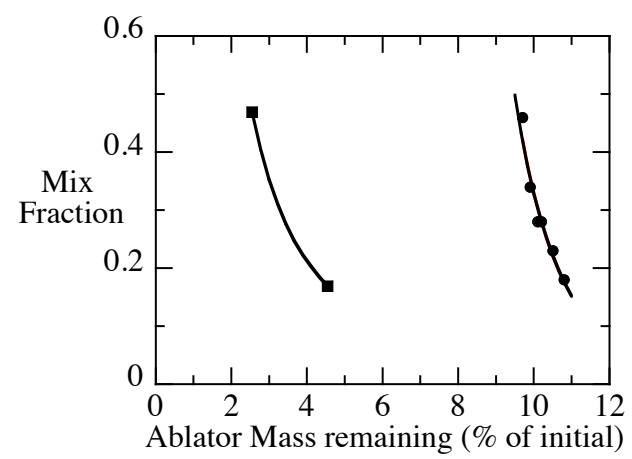


**Figure 19**

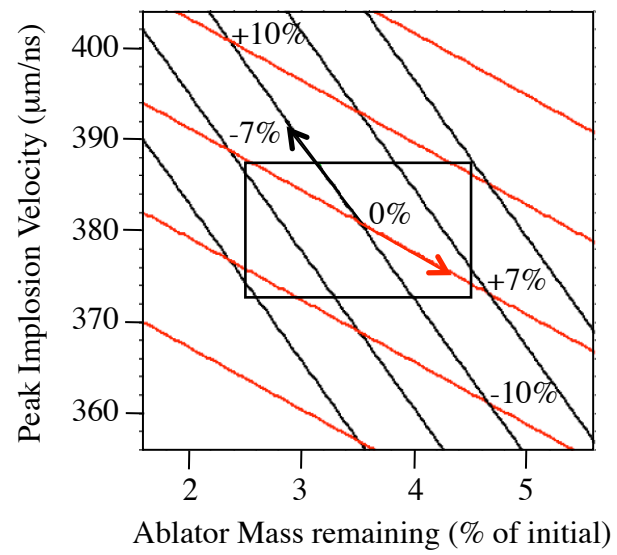


**Figure 20 (Color)**

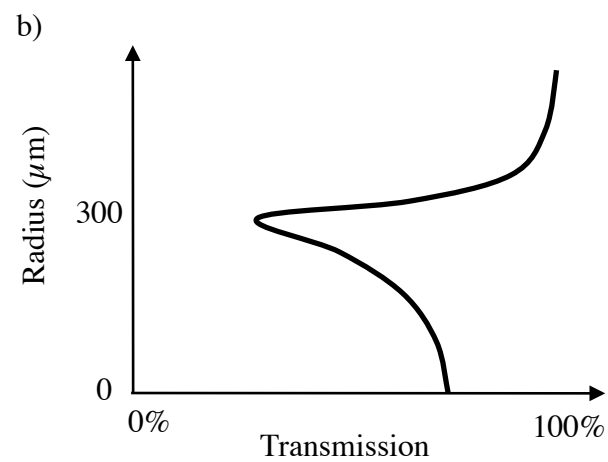
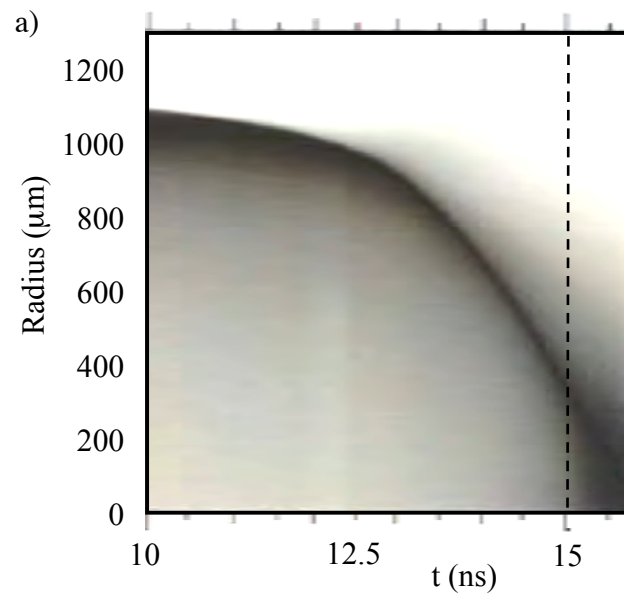


**Figure 21 (Color)**

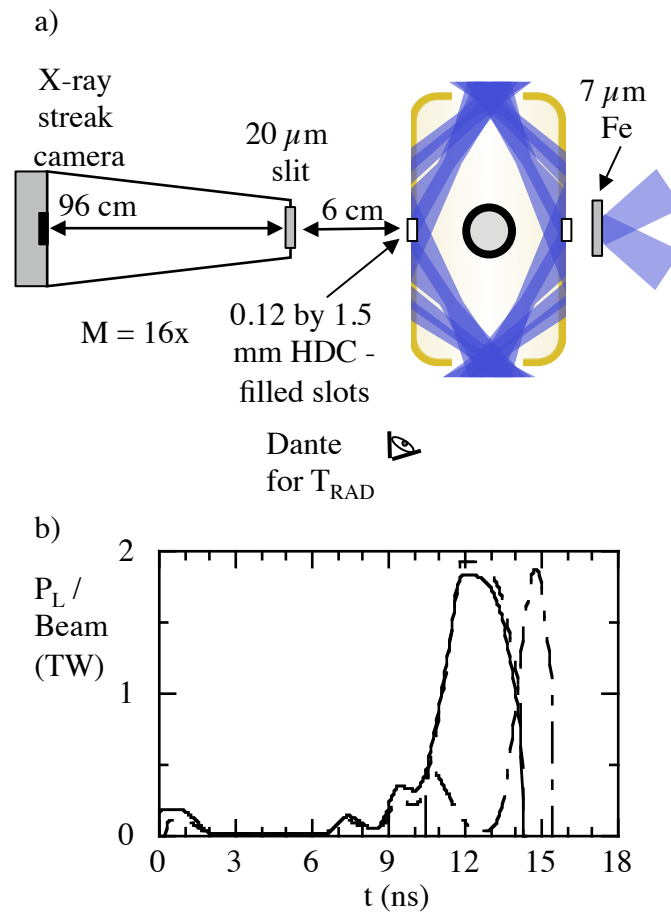


**Figure 22 (Color)**

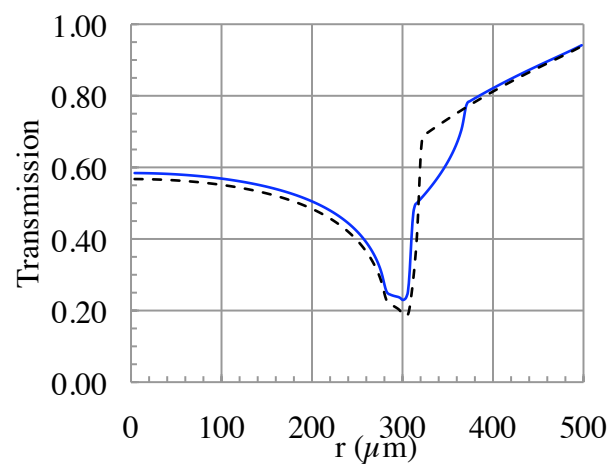


**Figure 23 (Color)**

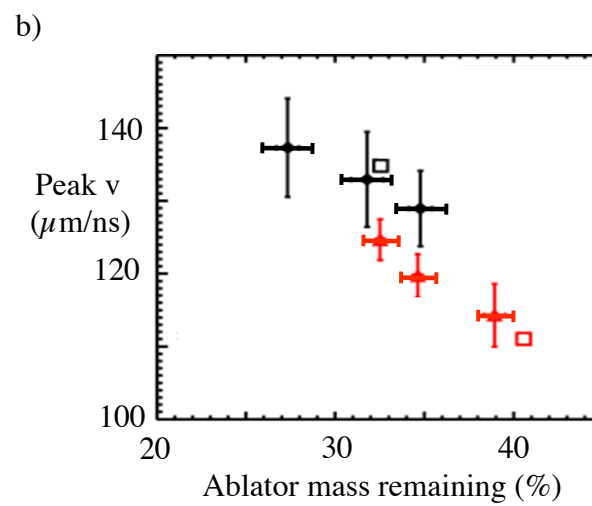
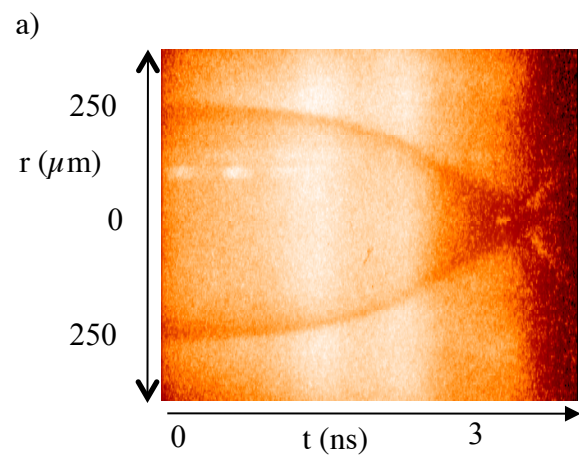


**Figure 24 (Color)**



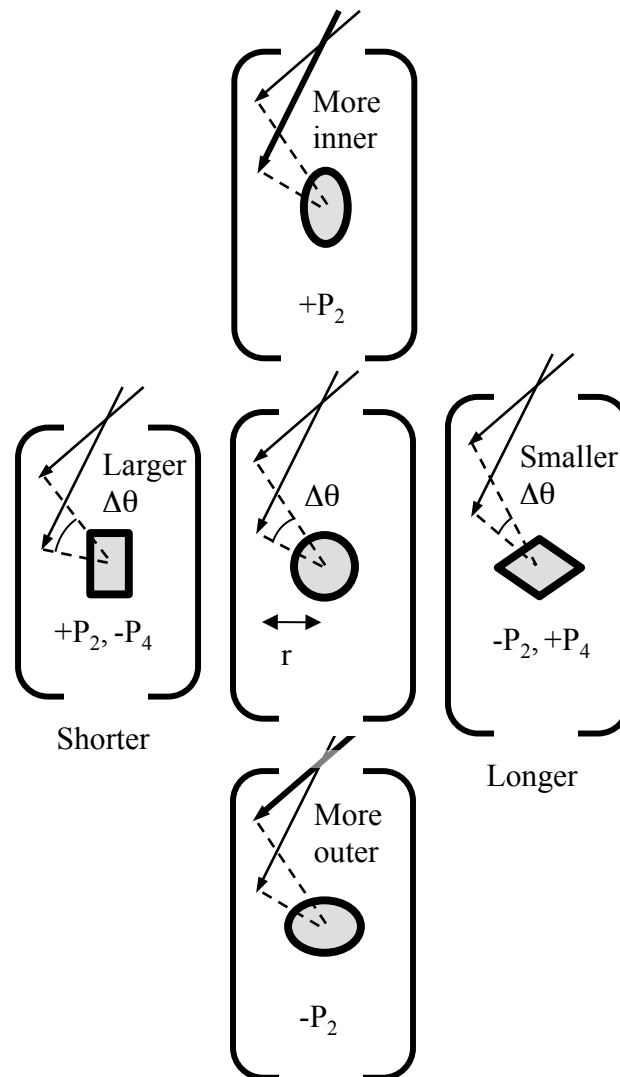


**Figure 25**

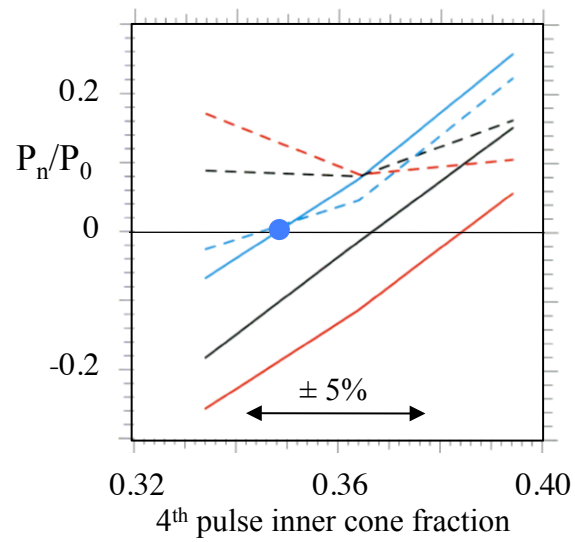


**Figure 26 (Color)**

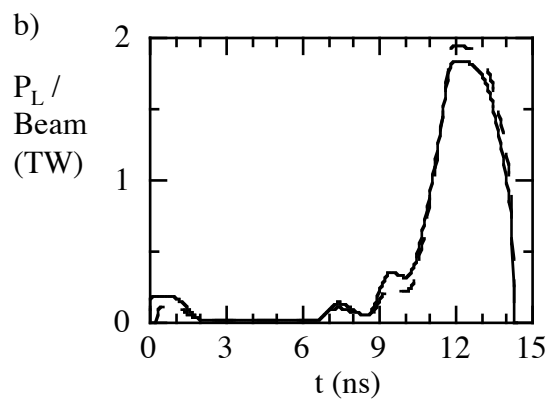
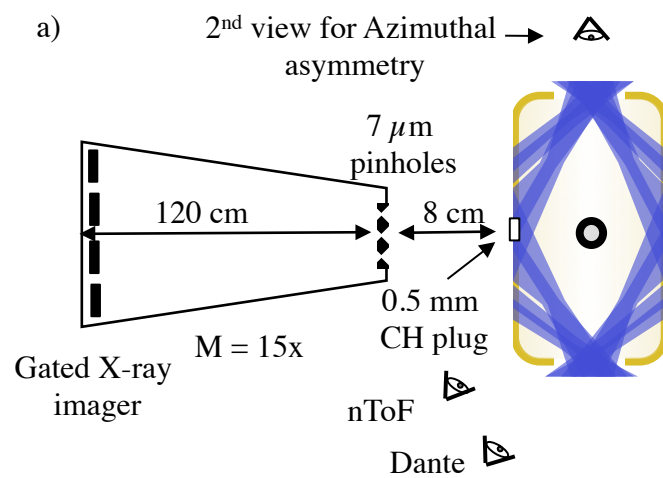


**Figure 27 (Color)**

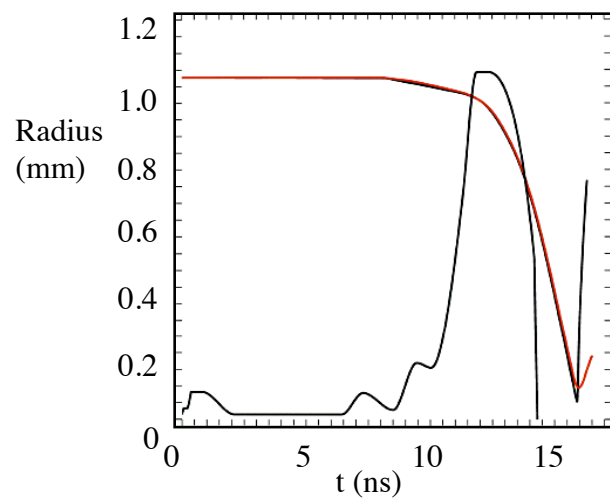


**Figure 28 (Color)**

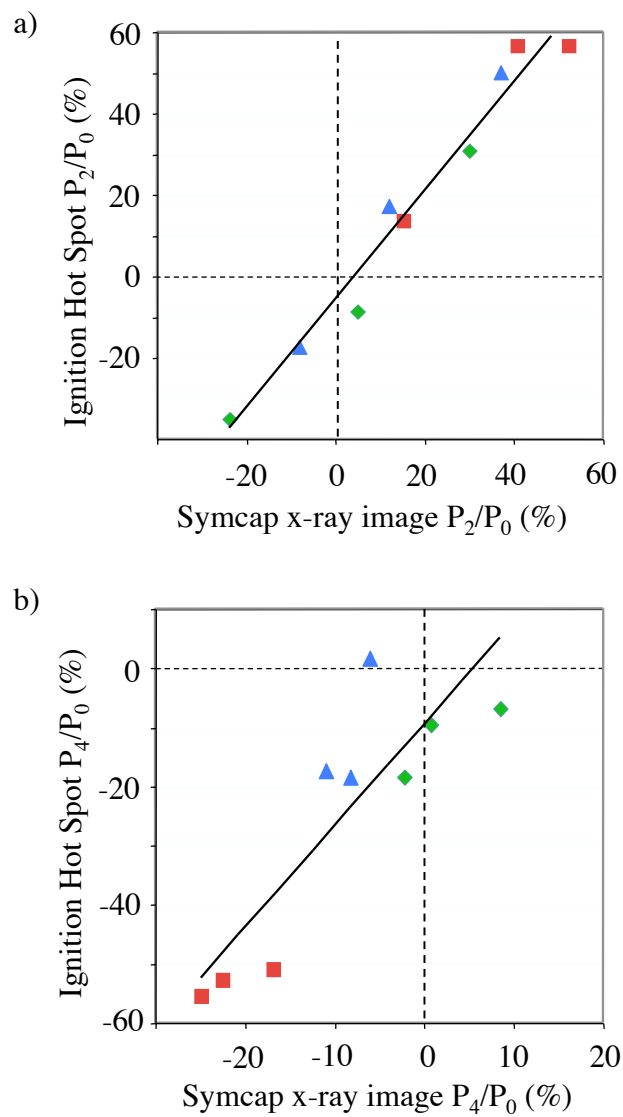


**Figure 29**

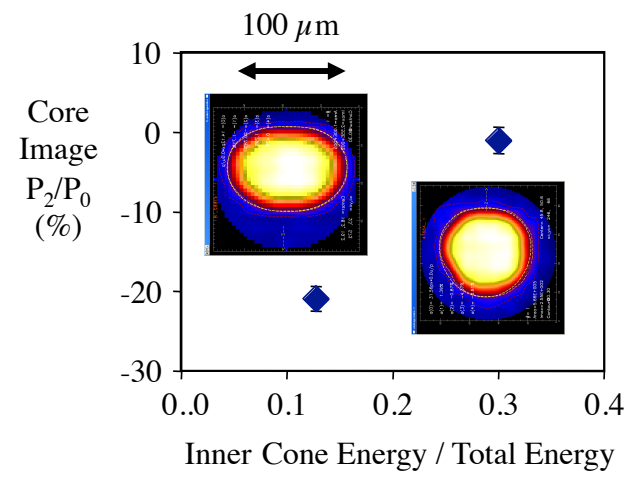


**Figure 30 (Color)**

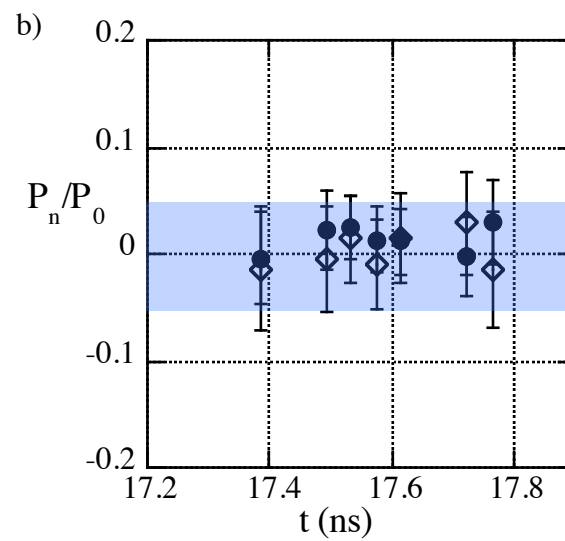
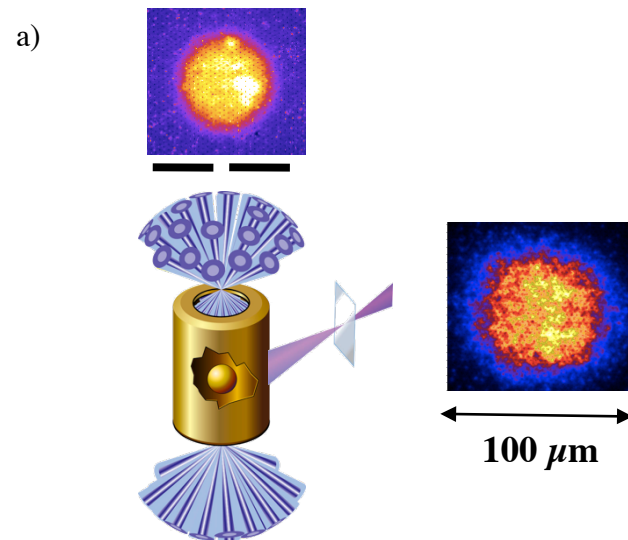


**Figure 31 (Color)**

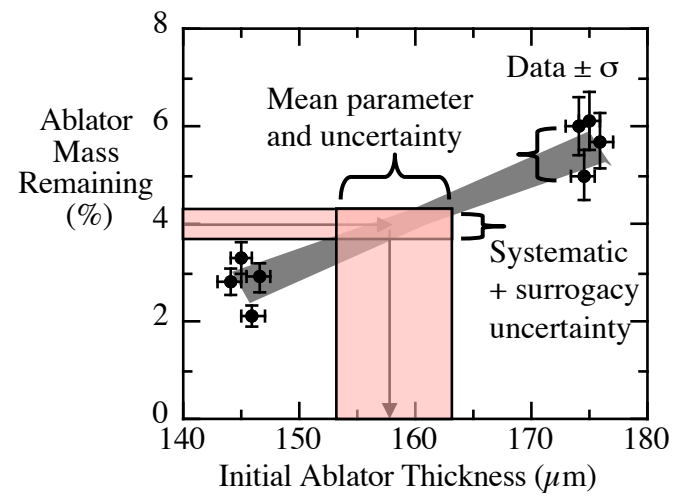


**Figure 32 (Color)**



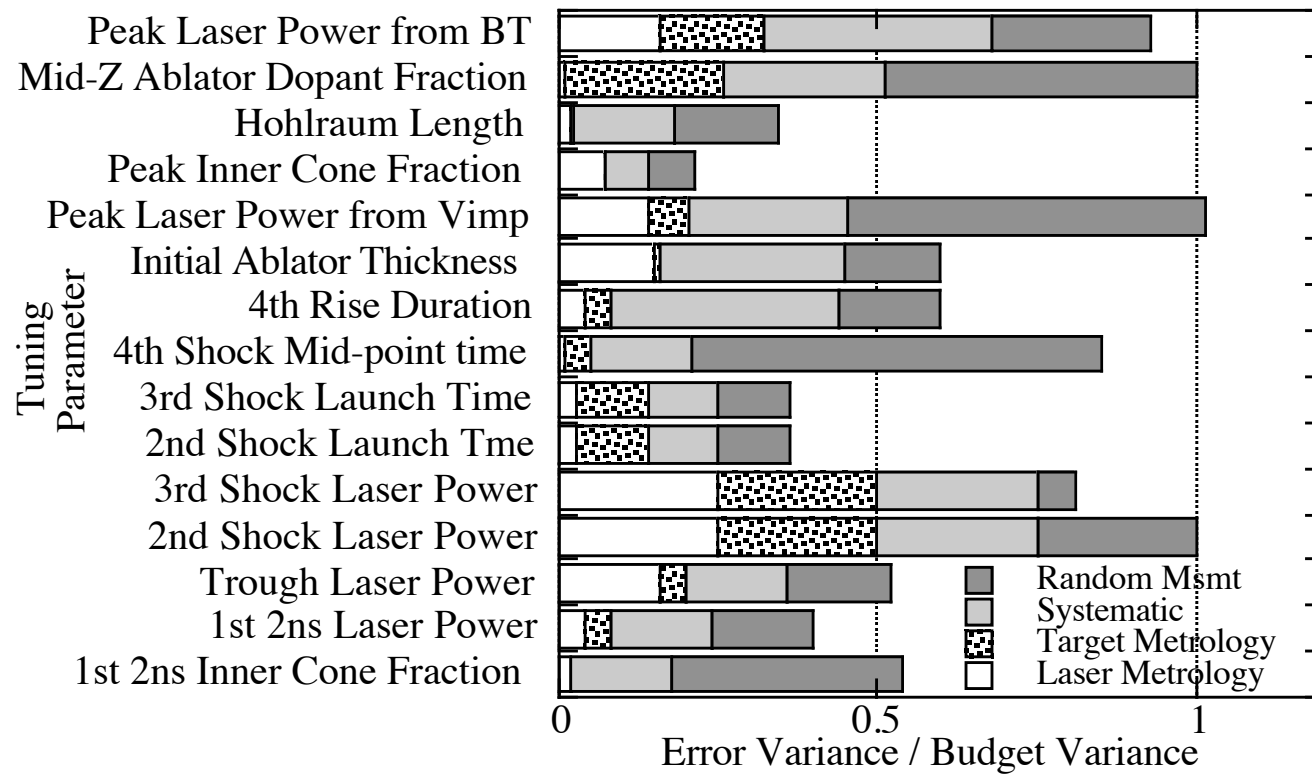


**Figure 33**

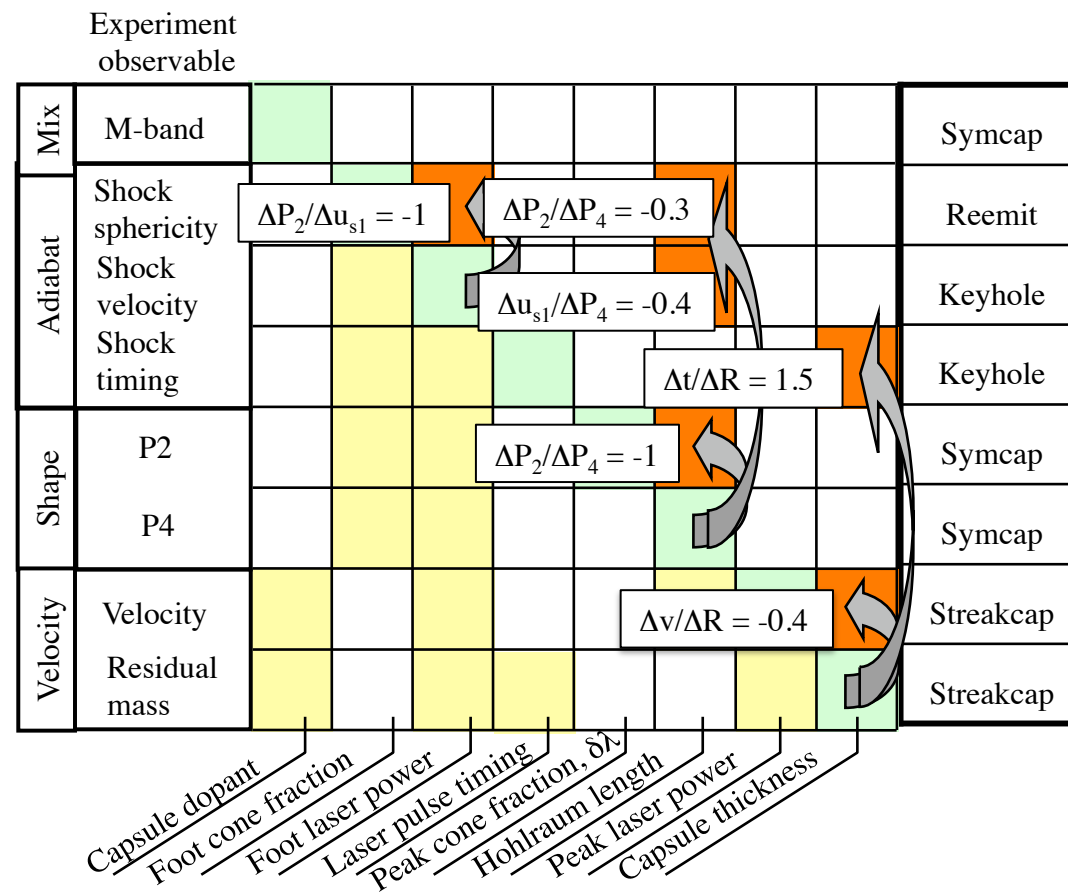


Figure 34